Research Updates

Enhancement of thermoelectric performance in two-dimensional materials: A review of recent progress

Gözde Özbal Sargin,[1] Engin Durgun,[2] Cem Sevik,[3] and Hâldun Sevinçli[4,*]

[1]*Department of Fundamental Sciences, Air NCO Vocational HE School, Turkish National Defence University, İzmir 35415, Türkiye*

[2]*UNAM-National Nanotechnology Research Center and Institute of Materials Science and Nanotechnology, Bilkent University, Ankara 06800, Türkiye*

[3]*COMMIT, Department of Physics and NANOlight Center of Excellence, University of Antwerp, Groenenborgerlaan 171, B-2020 Antwerp, Belgium*

[4]*Department of Physics, Bilkent University, Ankara 06800, Türkiye*

(Received 27 October 2023; revised 28 October 2025; accepted 14 January 2026; published 12 February 2026)

A thermal gradient not only generates a heat current but could also result in a usable voltage difference if applied to a suitable material. Conversely, it is possible to use voltage differences to drive heat currents. The effects related to the mutual conversion of temperature and voltage differences are known as the thermoelectric (TE) effects. TE materials have been used for energy harvesting and solid-state cooling applications for decades. Nevertheless, their performances need significant enhancements to overcome the growing demands for applications. The challenge is that a good TE material needs to have a high electrical conductivity like in a metal, a high Seebeck coefficient like in an insulator, and a low thermal conductivity like in a glass. A number of strategies have been proposed to meet these diverse demands. Dimension reduction is a promising route to enhance the efficiencies of conventional TE materials, and it was proposed long before the innovation of 2D materials. The emergence of 2D materials has stimulated intensive research into their TE properties, with numerous approaches proposed to enhance their performance. Here, we review the recent literature on the TE properties of 2D materials by focusing on the employed enhancement strategies. In addition to the effects of quantum confinement, strategies such as nanostructuring, strain engineering, edge/surface functionalization, creating defects/vacancies, and doping are discussed thoroughly. Approaches to incorporate the intrinsic electronic properties, to utilize the materials with intrinsically low lattice thermal conductivity, and proposed techniques to further lower thermal conductivity are also reviewed. Lastly, the properties of emerging 2D materials with potentially high TE efficiencies are summarized.

DOI: 10.1103/9wld-rh32

I. INTRODUCTION

The TE effect enables the direct conversion between thermal gradients and electrical power, offering a promising route for waste heat recovery. Among various applications, which includes energy harvesting, direct power generation, and cogeneration, waste heat recovery currently holds the largest share in the global TE generator market and is projected to maintain its leading position with continued growth [1].

Despite decades of research, improving TE energy conversion efficiency remains a persistent challenge, primarily because of the inherently conflicting requirements for high TE performance. The efficiency of a TE material is governed by the dimensionless figure of merit zT. Achieving a high zT demands a rare combination of properties: high electrical conductivity akin to metals, a large Seebeck coefficient (S) typical of insulators, and low thermal conductivity (TC) comparable to that of glasses. This intricate interplay of mutually opposing properties makes optimization difficult, and numerous strategies have been proposed to address the problem. One of the most promising strategies is reducing system dimensionality.

Over the past few decades, research on low-dimensional thermoelectricity has accelerated, particularly following the seminal theoretical work of Dresselhaus and Hicks, who demonstrated that reduced-dimensional systems could achieve superior TE performance [2,3]. Quantum confinement effects in low-dimensional materials enhance the density of states (DOS) near the Fermi level while simultaneously reducing lattice thermal conductivity (κ_l) via increased boundary scattering. As a result, efforts to predict novel low-dimensional TE materials and develop enhancement strategies have gained significant momentum. When combined with other optimization mechanisms, dimensionality reduction has led to remarkable improvements in the TE performance of two-dimensional (2D) materials [4–11]. A number of recent reviews survey thermoelectric research on selected 2D material classes such as transition-metal dichalcogenides and other vdW layered compounds [12–14]. Other comprehensive reviews address broad strategies for improving thermoelectric performance in specific bulk and low-dimensional systems

*Contact author: sevincli@fen.bilkent.edu.tr

Published by the American Physical Society under the terms of the Creative Commons Attribution 4.0 International license. Further distribution of this work must maintain attribution to the author(s) and the published article's title, journal citation, and DOI.

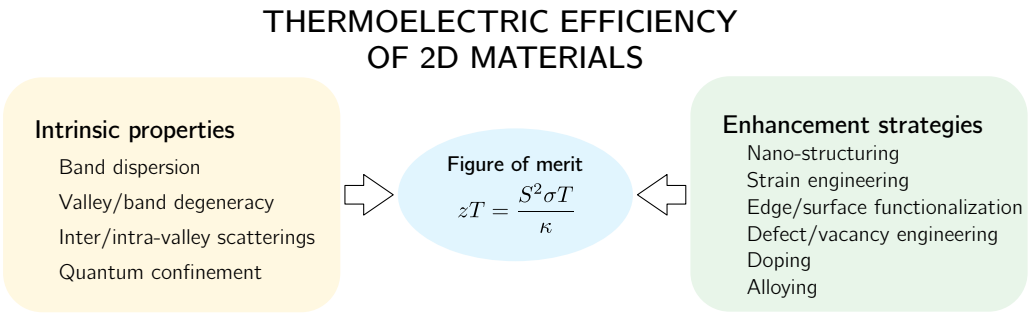


FIG. 1. Thermoelectric efficiency in 2D is reviewed in terms of the intrinsic properties of the materials and the proposed enhancement strategies.

[15,16]. However, to the best of our knowledge there is no single review that systematically organizes and assesses the enhancement mechanisms and spans the whole landscape of 2D material families in a unified, strategy-centric framework.

In this review, we first examine the interdependence between electronic band structures and TE efficiency, highlighting how band structure engineering plays a pivotal role in optimizing TE properties. We systematically discuss key concepts, including Rashba splitting, Janus materials, Mexican hat-shaped (MHS) and pudding-mold-type band structures, and topological band features. We further explore the influence of valley degeneracy and intervalley scattering on TE transport. We then provide an in-depth analysis of various enhancement strategies, including nanostructuring, strain engineering, edge and surface functionalization, and the effects of defects, vacancies, and doping, each addressed in dedicated subsections. A separate section is devoted to 2D materials characterized by inherently low κ_l, where we survey diverse approaches aimed at further reducing thermal transport in these systems. By comprehensively covering these intertwined aspects, our review offers a holistic perspective on the interplay between electronic structure, material properties, and optimization strategies, effectively summarizing recent progress toward achieving high-performance TE materials (Fig. 1). Finally, we review a selection of emerging TE materials, including twisted 2D materials, 2D perovskites, metal-organic frameworks (MOFs), covalent organic frameworks (COFs), and flexible 2D materials.

II. TRANSPORT COEFFICIENTS AND THE THERMOELECTRIC EFFECT

Two primary formulations for describing transport coefficients are extensively employed in the literature. The first is the semiclassical Boltzmann transport equation (BTE) approach, a versatile method applicable to a broad range of systems that allows for the inclusion of various scattering mechanisms affecting carrier transport. The second is the Landauer formalism, a quantum mechanical framework that does not assume a specific transport regime but instead relies on the quantum mechanical transmission probabilities of carriers. Consequently, the Landauer formalism provides a unified description of transport regimes ranging from ballistic to diffusive and localized, as well as more complex scenarios such as nonperiodic systems and constrictions, treating them on an equal footing [17–19].

In this section, we first present the general expressions for transport coefficients within the Landauer formalism. We also provide the corresponding expressions derived from the BTE. While the BTE and Landauer approaches are equivalent in the diffusive regime, the Landauer approach—by explicitly incorporating quantum mechanical transmission probabilities—offers particular advantages in analyzing systems where quantum effects play a critical role. We do not include the detailed derivations of these expressions here, as they are comprehensively covered in the literature [19,20].

In the Landauer formalism, charge transport is described by considering the transmission of carriers from one reservoir to another through a central region that represents the material of interest and incorporates the relevant scattering mechanisms. Considering that the reservoirs are maintained at different chemical potentials and temperatures, the charge current can be expressed as [21]

$$I = \frac{2e}{h}\int dE\, \mathcal{T}(E)(f_L(E) - f_R(E)), \tag{1}$$

where spin degeneracy is assumed, $\mathcal{T}(E)=M(E)t(E)$ is the transmission amplitude with $M(E)$ being the number of modes, $t(E)$ is the average transmission probability, and $f_{L/R}$ is the Fermi-Dirac distribution function at the left/right reservoir. Under near-equilibrium conditions, the Fermi-Dirac function can be expanded in terms of the differences in chemical potential μ, and temperature T. Consequently, the difference in occupation factors can be expressed as

$$f_L - f_R = \left(-\frac{\partial f}{\partial E}\right)e\Delta V - \left(-\frac{\partial f}{\partial E}\right)\frac{E-\mu}{T}\Delta T. \tag{2}$$

In the diffusive regime, transmission probability decreases with length, $t(E)\simeq\Lambda(E)/L$, where Λ is the mean free path for back scattering, and L is the system length. One defines the following integral functions for shorthand notation:

$$\mathcal{L}_n(\mu, T) = \frac{2}{h}\int dE\left(-\frac{\partial f}{\partial E}\right)(E-\mu)^n\mathcal{M}(E)\Lambda(E), \tag{3}$$

with $\mathcal{M} = M/A$ denoting the number of modes per cross-section area A. At thermal equilibrium ($\Delta T = 0$), referring to Eq. (2), one can write

$$I = \frac{A\,\Delta V}{L}e^2\mathcal{L}_o, \tag{4}$$

therefore, electrical conductivity σ is

$$\sigma = e^2\mathcal{L}_o. \tag{5}$$

The mean free path for back scattering can be expressed in terms of the carrier velocity and relaxation time as

$$\Lambda(E) = \frac{2\langle v_x^2 \tau \rangle}{\langle |v_x| \rangle}, \tag{6}$$

where v_x is the velocity component in the transport direction [20]. The above expression yields

$$\Lambda_{1D} = 2v(E)\tau(E), \tag{7}$$

$$\Lambda_{2D} = \frac{\pi}{2} v(E)\tau(E), \tag{8}$$

$$\Lambda_{3D} = \frac{4}{3} v(E)\tau(E), \tag{9}$$

for systems of different dimensionalities. Considering the fact that only carriers near the Fermi level (E_F) contribute to transport, it is common to assume either a constant scattering time or a constant mean free path.

When $\Delta T \neq 0$, charge current consists of two terms, one originating from ΔV and the other from ΔT,

$$I = \frac{A\,\Delta V}{L} e^2 \mathcal{L}_o - \frac{A\,\Delta T}{L} \frac{e}{T} \mathcal{L}_1. \tag{10}$$

The Seebeck coefficient can be extracted from the above expression. The current induced by a temperature difference can be canceled by an applied voltage difference, and S (Seebeck coefficient) is defined as the ratio of this voltage difference to the temperature difference,

$$\mathcal{L}_o \Delta V = \frac{1}{eT} \mathcal{L}_1 \Delta T, \tag{11}$$

and hence

$$S = -\frac{\Delta V}{\Delta T} = -\frac{1}{eT} \frac{\mathcal{L}_1}{\mathcal{L}_o}. \tag{12}$$

Similar to Eq. (1), electronic heat current can be expressed as

$$J_e = \frac{2}{h} \int dE\, \mathcal{T}(E)(E - \mu)(f_L(E) - f_R(E)). \tag{13}$$

Using the expansion of the occupation factor around equilibrium values of μ and T, and imposing the zero charge current condition, i.e., $\Delta V = (1/eT)(\mathcal{L}_1/\mathcal{L}_o)\Delta T$, we can write

$$J_e = \frac{1}{T} \left(\frac{\mathcal{L}_1^2}{\mathcal{L}_o} - \mathcal{L}_2 \right) \frac{A\,\Delta T}{L}. \tag{14}$$

Referring to Fourier's Law, electrical contribution to thermal conductivity is written as

$$\kappa_e = \frac{1}{T} \left(\mathcal{L}_2 - \frac{\mathcal{L}_1^2}{\mathcal{L}_o} \right). \tag{15}$$

The power factor (PF) is given by

$$P = S^2 \sigma, \tag{16}$$

and the figure of merit reads

$$zT = \frac{S^2 \sigma T}{\kappa_e + \kappa_l}. \tag{17}$$

It is possible to collect material-specific parameters into a single term, known as the TE quality factor. Assuming a parabolic band dispersion, zT of a 2D structure can be expressed as [3,22,23]

$$z_{2D}T = \frac{\left(\frac{2F_1}{F_0} - \eta\right)^2 F_0}{\frac{1}{B} + 3F_2 - \frac{4F_1^2}{F_0}}, \tag{18}$$

where the Fermi-Dirac functions are defined as $F_i = \int_0^\infty (e^{x-\eta} + 1)^{-1} x^i\, dx$, and B denotes the TE quality factor. The factor B is primarily determined by the intrinsic properties of the material, such as the effective mass, carrier mobility, and lattice thermal conductivity. Once B is established for a material, the optimal doping level required to maximize zT can be determined by adjusting the reduced chemical potential η.

In the BTE approach, transport coefficients are in terms of the carrier velocities and the scattering rates instead of the transmission probabilities [24,25]. Using BTE, the electrical conductivity of a D-dimensional material is defined as

$$\sigma_{\mathrm{BTE}} = \frac{e^2}{L^D} \sum_{n\mathbf{k}} v_n^2(\mathbf{k})\, \tau_n(\mathbf{k}) \left(-\frac{\partial f}{\partial E} \right), \tag{19}$$

where n denotes the band index. S is given by

$$S_{\mathrm{BTE}} = \frac{1}{\sigma} \frac{1}{eTL^D} \sum_{n\mathbf{k}} v_n^2(\mathbf{k})\, \tau_n(\mathbf{k})(\mu - E_{n\mathbf{k}}) \left(-\frac{\partial f}{\partial E} \right). \tag{20}$$

For a given energy, the transport distribution function (TDF) is defined as

$$\Sigma(E) = v_x(E)^2 \tau(E) D(E), \tag{21}$$

where v_x, τ, and D are the average velocity along the transport direction, the relaxation time, and DOS, respectively [26]. TDF and its spectral width are central quantities for TE efficiency. For materials with sizes much larger than the mean free path and operating in the diffusion regime, BTE results are equivalent to those obtained from the Landauer formalism [20].

The lattice thermal conductivity can be defined using quantum mechanical transmission probabilities within the Landauer approach as

$$\kappa_l = \int \frac{d\omega}{2\pi} \hbar\omega\, \mathcal{M}_p(\omega)\, \Lambda_p(\omega) \frac{\partial f_{BE}}{\partial T}, \tag{22}$$

where $\mathcal{M}_p$ and Λ_p denote the number of phonon modes per cross section area and the phonon mean free path for back scattering, respectively [27–29]. The BTE approach is widely employed also to calculate the lattice TC of crystalline solids [24,30]. Within BTE, the lattice thermal conductivity tensor is expressed as

$$\kappa_{\alpha\beta} = \sum_{j\mathbf{q}} C_{j\mathbf{q}} v_{j\mathbf{q}\alpha} v_{j\mathbf{q}\beta} \tau_{j\mathbf{q}\beta}, \tag{23}$$

where $C_{j\mathbf{q}} = k_{\mathrm{B}}(\hbar\omega/k_{\mathrm{B}}T)^2 f_{BE}(j\mathbf{q})[f_{BE}(j\mathbf{q}) + 1]$ represents the mode contribution to specific heat, and $\tau_{j\mathbf{q}\beta}$ is the phonon scattering rate. By employing density functional theory to compute harmonic and higher-order force constants, the scattering rates can be directly obtained. This approach has proven reliable when benchmarked against experimental data [31,32].

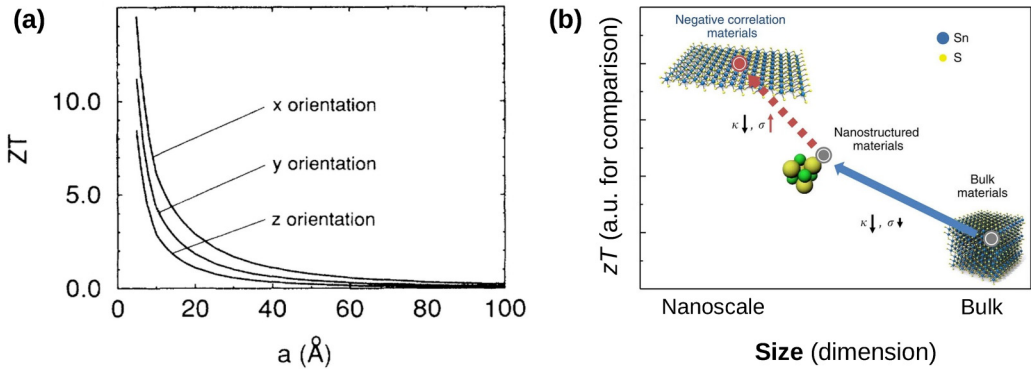


FIG. 2. Efficiency in TE conversion is closely related to the energy bandwidths and dimensionality of the system. (a) Quantum confinement was shown to boost the TE figure of merit in reduced dimensions by Hicks and Dresselhaus. Reproduced with permission from Refs. [2,3]. Generating a negative correlation between electrical and thermal conductivities by reducing the system's thickness is one of the approaches proposed to meet the conflicting demands of TE efficiency, as demonstrated for SnS_2 (b). (Reproduced with permission from Ref. [34].)

III. QUANTUM CONFINEMENT EFFECT

The strategy of employing dimension reduction to enhance the TE figure of merit dates back to the early 1990s. At that time, achieving $zT \simeq 1$ represented the industrial benchmark, and new strategies were sought to surpass this value. Two primary motivations underpinned the low-dimensional materials approach. The first was to exploit the enhancement of the PF in reduced dimensions. The second aimed to leverage the different scattering lengths of carriers and phonons to achieve a greater reduction in TC relative to electrical conductivity.

The effects of quantum confinement were first analyzed by Hicks and Dresselhaus [2,3]. They have demonstrated that confining the carriers introduces a new variable, the confinement length, into the transport coefficients. This variable can then be utilized to optimize S, σ, and κ, which are inherently interrelated and challenging to control independently. The potential advantages of this approach include: (i) enhancement of DOS near E_F, leading to an increased S; (ii) the opportunity to exploit anisotropic Fermi surfaces; (iii) possibilities to increase carrier mobility; and (iv) enhanced phonon boundary scattering at interfaces, particularly relevant when dimensionality is reduced through the introduction of superlattices [33].

The energy dispersion for carriers in reduced dimensions can be expressed within the effective mass approximation as

$$E_{2D}(k_x, k_y) = \frac{\hbar^2 k_x^2}{2m_x} + \frac{\hbar^2 k_y^2}{2m_y} + \frac{\hbar^2 \pi^2}{2m_z d_z^2} \tag{24}$$

for 2D confinement, and

$$E_{1D}(k_x) = \frac{\hbar^2 k_x^2}{2m_x} + \frac{\hbar^2 \pi^2}{2m_y d_y^2} + \frac{\hbar^2 \pi^2}{2m_z d_z^2} \tag{25}$$

for 1D confinement. Here, m_x, m_y, and m_z denote the components of the effective mass tensor. In this description, the 2D system lies in the xy plane, whereas the 1D system extends along the x direction, and d_y and d_z represent thickness. In the diffusive regime, assuming an energy-independent mobility, the TE quality factor B is found to increase with $1/d_z$ in 2D systems and with $1/(d_y d_z)$ in 1D systems [2,3]. In their study on Bi_2Te_3, Hicks and Dresselhaus predicted that the bulk zT value of Bi_2Te_3, calculated as 0.52 at 300 K, could experience a remarkable 14-fold enhancement when structured as a superlattice with a layer thickness $d_z = 1$ nm, reaching $zT = 6.9$ [2]. Similarly, in the 1D case, a value of $zT = 14$ was calculated for a Bi_2Te_3 nanowire with a width of 5 Å, as illustrated in Fig. 2(a) [3]. In these calculations, the phonon mean free path was assumed to be equal to the confinement lengths d_y and d_z.

Sofo and Mahan revisited the analysis [35], where they additionally considered the tunneling probability between the quantum wells and the finite TC of the material forming the barriers. They derived expressions similar to those in Ref. [2], with the key distinction that, instead of the quantum well width appearing in the denominator, their expressions incorporate the superlattice period. By accounting for the finite TC of the barrier region, they concluded that an enhancement of zT does indeed arise because of the increased DOS; however, this enhancement was estimated to be approximately twofold for a barrier width of 15 Å [35].

Motivated by these early studies on quantum size effects, high values for thermopower and PF have been predicted for several low-dimensional materials in both theoretical and experimental works [4–6,36–40]. Hung *et al.* reported that the confinement length L must be smaller than the de Broglie wavelength λ_{dB} in order to achieve an improved PF [7,41]. Subsequently, the validity of the proposed analytical formula for the optimum PF has been experimentally confirmed [8,9,42,43]. Very recently, first-principles studies on 2D β-bismuth have shown that reducing the number of layers improves the TE properties, particularly when L/Λ is less than 0.1 [44]. In addition, a negative correlation has been observed between σ and κ in nanostructured materials, opening a new pathway for enhancing zT, as depicted in Fig. 2(b) [34]. The quantum size effect can enhance not only the PF but also reduce the lattice thermal conductivity. For instance, the calculated κ_l of 2H-polytype $SnSe_2$ ranges from 1.29 to 2.87 $Wm^{-1}K^{-1}$ from monolayer to bulk form, in good agreement with experimental results [45]. In addition to the effects of quantum confinement through the density of states, there are theoretical works that approach the effects of confinement within a broader nanoscale thermodynamics

framework. In particular, Whitney and coworkers analyzed the fundamental aspects of steady-state heat-to-work conversion at the nanoscale, demonstrating that mechanisms such as energy filtering and confinement-induced discrete spectra are not only beneficial but also set intrinsic bounds on the efficiency and power of TE devices [46]. Several dedicated reviews have been published on the effects of quantum confinement on TE efficiency [10,47–49], and it is worth noting that dimensionality is an intrinsic factor influencing thermoelectric performance in all 2D materials, and it underpins the strategies discussed throughout this review.

IV. EFFECTS OF INTRINSIC ELECTRONIC PROPERTIES ON THERMOELECTRIC PERFORMANCE

Several studies adopting diverse theoretical approaches have investigated the ideal electronic band structure for optimizing TE efficiency [26,50–57]. In a seminal work, Mahan and Sofo have analyzed the TDF, as defined in Eq. (21), to identify optimal conditions for TE performance [26]. They have shown that an ideal TDF resembles a delta function, leading to maximum efficiency in the limit of vanishing lattice thermal conductivity κ_l [58]. This idea forms the basis of the energy-filtering concept, which favors narrow transport windows. More recently, Zhou *et al.* have revisited this problem using tight-binding band structures and various scattering models [50]. Their findings have shown that the best performance is not achieved with extremely narrow bands, but rather with a finite bandwidth whose optimum value depends on both scattering mechanisms and dimensionality. It should be noted that the TDF width cannot be equated directly with the electronic bandwidth. Instead, it is influenced by band dispersion, system dimensionality, and the energy dependence of scattering. As such, comparing the two widths is nontrivial. Additionally, Whitney has studied TE efficiency at finite power output using a nonlinear quantum scattering framework [57]. He has demonstrated that maximum efficiency is achieved when electron transport is restricted to a narrow energy window, thereby reinforcing the energy-filtering concept even under non-equilibrium conditions. While these theoretical studies have offered valuable insights, they typically rely on simplifying assumptions such as parabolic band edges or deformation potential (DP) approximations. Although such assumptions facilitate analytical treatment, they may limit the applicability of the results to real materials with complex electronic and phonon landscapes.

It should be noted that in the aforementioned analyses of optimal bandwidth, the parabolic band approximation is generally assumed to be valid near the band edges. The applicability of the single parabolic band model to materials with nonparabolic or complex band structures has been discussed in several studies [51–53]. These works have suggested the use of multiband models when intricate band features are present. Additionally, some approaches have retained the simple parabolic band (SPB) model while incorporating more sophisticated scattering mechanisms, yielding results that show better agreement with experimental data. The applicability of the new form of SPB was examined on 490 sets of experimental data. The restructured model provides a good fit to the classical SPB model over a wide range of carrier concentrations (Fig. 3), and the relative errors in key transport parameters were found to be less than 2%.

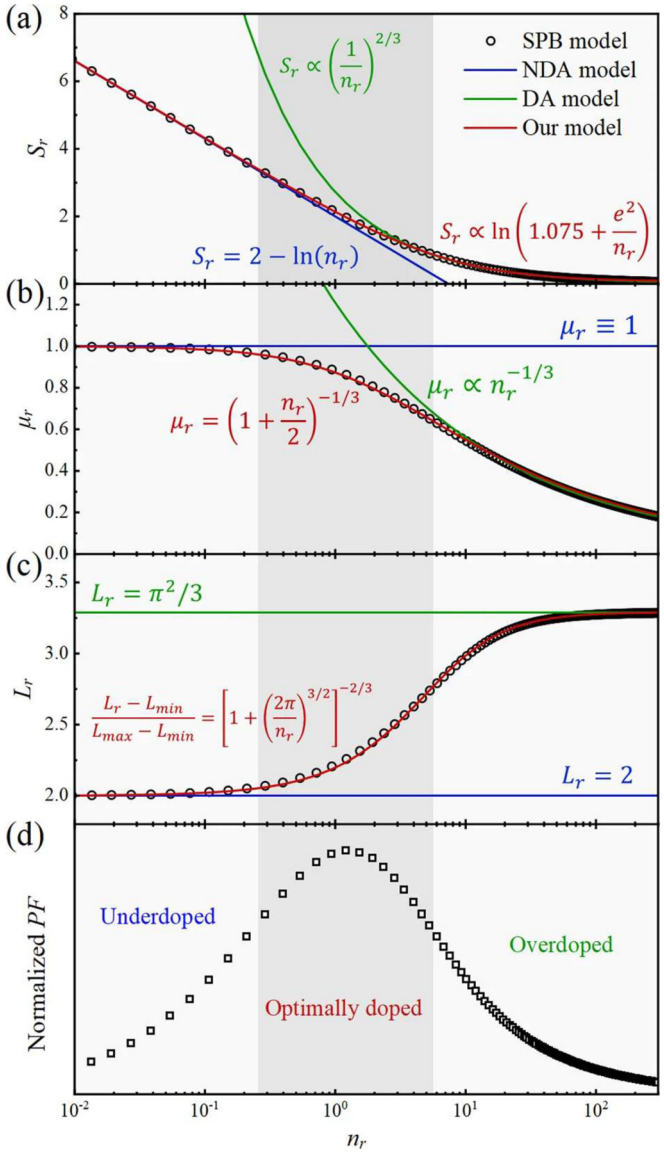


FIG. 3. The feasibility and accuracy of the reformed SPB model are tested by gathering 490 groups of experimental data, including the Seebeck coefficient, carrier concentration, and mobility. (a) Reduced Seebeck coefficient, (b) reduced mobility, (c) reduced Lorenz number, and (d) normalized PF generated by solving the classical single parabolic band (SPB) model, nondegenerate approximation model, degenerate approximation model, and restructured model, respectively. (Reproduced with permission from Ref. [53].)

Band isotropy, symmetry in the DOS, the dominant scattering mechanism, and its characteristics are among the intrinsic properties that influence TE performance. Detailed simulations have predicted that extremely anisotropic bands can yield high performance, particularly when bidirectional anisotropy mimicking a 1D-like band structure is achieved [59,60]. Moreover, it has been reported that the benefits of pocket multiplicity and band convergence depend on the relative shapes of the bands and the nature of the scattering mechanism; in particular, the coexistence of heavy

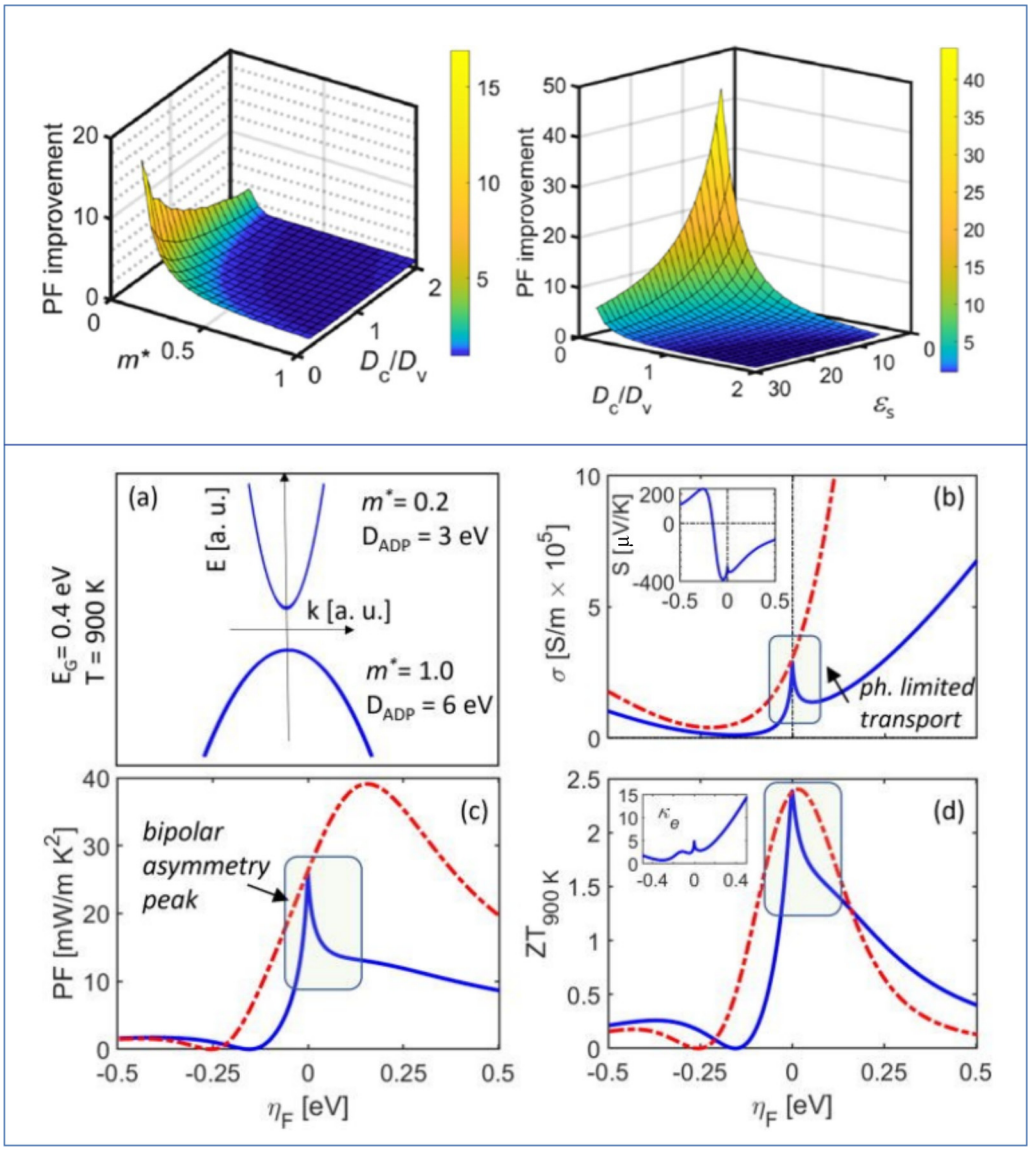


FIG. 4. Transport asymmetries, including effective masses, DOS, or phonon scattering rates, are crucial for obtaining high PF through finite Seebeck coefficient and high electrical conductivity in bipolar transport regime. (Top) Narrow band gap materials can reach a high PF value of 50 $\mathrm{mW/mK^2}$. (Reproduced with permission from Ref. [61].) (Bottom) (a) Illustration of highly anisotropic parabolic bands. (b) Electrical conductivity. (Inset) Seebeck coefficient). (c) Power factor, and (d) the figure of merit with $\kappa_l = 5\ \mathrm{W\,m^{-1}K^{-1}}$ [(Inset) κ_e in units of $\mathrm{W\,m^{-1}K^{-1}}$] are obtained under ionized impurity scattering and phonon limited case. (Reproduced with permission from Ref. [56].)

and light pockets can also be detrimental [59]. In the bipolar transport regime, asymmetric conduction and valence bands have been shown to provide significant improvements in narrow band gap semiconductors, representing a promising strategy for enhancement. Figure 4 illustrates the underlying mechanisms mentioned above for achieving a high PF.

In addition, there have been attempts to develop selection criteria or descriptors to maximize the PF of semiconductors as well as metals [62,63]. The suggested descriptors can assist machine learning studies in identifying material classes with exceptional PF. The conditions to obtain a high PF in narrow bandgap alloys were determined by analyzing analytical band structures, and it was concluded that structures possessing asymmetry in their density-of-states effective mass (m^*_{DOS}) or conductivity effective mass (m^*_c), along with asymmetry in electron-phonon (e–ph) scattering strength, yield high TE performance [56].

The improvement of PF for 2D materials can also be achieved by combining low effective mass, a step-like DOS, a dominant inelastic scattering mechanism, and high valley degeneracy [64]. It is also necessary to tune the bandwidth such that electrons contribute to transport without undergoing intervalley scattering. For example, in a prototype system (based initially on MoS_2) that incorporates all of the aforementioned attributes, the PF was shown to increase significantly from $0.044\ \mathrm{Wm^{-1}\,K^{-2}}$ to $22\ \mathrm{Wm^{-1}\,K^{-2}}$ [64].

A. High thermoelectric figure of merit inherent to band dispersions

Based on the above discussions, we review the TE performances of several distinctive electronic band structures in 2D materials. These band structures can help overcome the inherent trade-off between S and σ, thereby enhancing PF and zT.

Mexican-hat-shaped (quartic dispersion) bands. 2D materials that display MHS bands are prominent candidates for future electronic, spintronic, and TE devices [65–69]. The strong van Hove singularity at the quartic band edge leads to magnetic instability, doping-induced ferromagnetism, and ferroelasticity [70–75]. Bilayer graphene under external electric field [76], α-SnO [73], buckled-hexagonal phase of Bi-monolayer [77], transition metal dichalcogenide (TMD) heterostructure under strain [67], indium triphosphide [78], group VA-binary compounds [65,79], group III-VI monolayers [80–82], and their Janus counterparts [75,83] present these peculiar properties under p-type doping. From the TE perspective, there have been notable efforts to investigate the effect of MHS band character on TE efficiency utilizing first-principles calculations and analytical derivations to date [54,65,84,85].

The strong singularity at the band edge is associated with a step-like increase in the density of modes, and this gives rise to enhanced S and PF values, which also ensure high zT values [54]. However, the enlarged carrier pocket caused by degenerate critical points enhances scatterings and degrades σ. Therefore, zT depends on how scatterings affect S and σ. Monolayer group III-chalcogenides present inherently high TE efficiency, which is attributed to the step-like transmission spectra originating from the MHS valence band (VB). This distinctive transmission spectrum, combined with ultralow lattice thermal conductivity, boosts the zT value at various temperatures as seen in heavy compounds like InS, InSe, GaTe, and TlSe [66,86,87]. The novel stable phase of tin chalcogenides offers high n/p-type zT values from 300 K to 900 K [37]. While having a quartic VB improves its PF, the low elastic constants and strong lattice anharmonicity are reported to result in high zT values above 1 at room temperature. Group IV-V binaries are another leading class among the 2D material families with high TE efficiency, which is also because of the MHS VB. Among group IV-V binaries, CN, SiN, GeN, SnN, SiP, GeP, SnP, PbP, SnAs, and PbAs exhibit quartic dispersion at their VB edges [88]. Complementary findings have been reported by Ozbey *et al.* showing that GeP monolayer has a high p-type zT value of 1.72 at 800 K owing to the quartic topmost VB [89]. The peak values of electronic zT at 300 K of p-type SiN, SiP, and SiBi are reported as 0.99, 0.98, and 0.94, respectively [90]. Janus counterparts of group IV-V binaries such as Sn_2PAs and strained-Ge_2PAs have improved zT values because of the convergence of their parabolic and MHS valence bands [89,91].

Ring-shaped (octic dispersion) bands. M_2X_3 (M = Bi, Sb; X = S, Se, Te) layered compounds attract intense interest not only because of their topological properties but also because they are good candidates for TE applications [92,93]. They fulfill the requirements in terms of structural and electronic properties. For instance, heavy elements give rise to suppressed κ_l and provide a strong spin-orbit coupling (SOC) effect. Although their narrow band gap causes bipolar conduction and decreases S, alloying with heavy compounds has been suggested to help manage this problem [94,95].

By reducing the thickness of these topological insulator (TI) materials to a few quintiple layers (QLs), they undergo a transition from trivial to nontrivial surface states, and the valence band exhibits an unusual dispersion called the *octic* dispersion. Both analytical and numerical results have shown that the 1-QL case displays better TE properties compared to the 2-QL, thanks to the octic dispersion in which the energy-momentum relation is an eighth-order polynomial in k, as shown in Fig. 5(b) [55,96]. For 1-QL Bi_2Te_3, the optimized zT has been reported to be 1.1 with hole carrier concentration. The synergistic effect of quantum confinement and two-ring maxima of the valence band increases the TE efficiency. In addition, tight-binding analysis on the TE properties of bismuthene has shown that TIs can display extraordinary efficiency under high doping and in the case of introducing trivial edge states [97]. This, in combination with a higher σ/κ_e ratio and a large S, has led to zT values as high as 2.1 for Bi_2Se_3 thin films (10-QL $\geqslant t \geqslant$ 6-QL) [98]. Detailed information on the properties of 2D- and 3D-TE TIs can be found in recent reviews [99–102].

Pudding-mold-shaped bands. The pudding-mold-type band structure [Fig. 5(c)] is another distinctive electronic dispersion that has been shown to enhance TE efficiency [103,104,110]. This anisotropic band structure comprises flat (high m^*) and highly dispersive (low m^*) regions along different directions in the reciprocal space. It has been argued that such a configuration can simultaneously maximize the PF by combining the high S derived from the flat portion with the high σ enabled by the dispersive part. Furthermore, both theoretical and computational studies have suggested that 3D and 2D materials with pudding-mold-type bands exhibit superior PF and zT values compared to those with conventional parabolic bands [105]. 2D crystals of GeP_3 and SnP_3 have been identified as promising TE candidates because of their intrinsic pudding-mold-type band structures. Their maximum p-type zT values have been reported as 3.33 at 300 K and 4.46 at 700 K, respectively [106,107]. Similarly, the 1T-phase of the Tl_2O monolayer has exhibited exceptional zT values ranging from 1.79 to 4.20 between 300 K and 900 K under hole doping, attributed to its valence band with pudding-mold characteristics [108]. We should note that the maximum values of S and σ in these structures are often realized along different crystallographic directions, which can undermine the simultaneous optimization of zT.

Rashba spin splitting. Rashba spin splitting offers a novel enhancement mechanism for the electronic TE properties of materials [109]. The Hamiltonian that expresses the Rashba SOC is given as $H_{SOC} = \alpha_R(\boldsymbol{\sigma} \times \mathbf{k}) \cdot \mathbf{z}$, where α_R is the Rashba parameter, $\boldsymbol{\sigma}$ represents the Pauli spin matrices, and $\mathbf{k}$ is the crystal momentum. The strength of the Rashba effect is determined by $\alpha_R = 2E_0/|\mathbf{k}_0|$, where E_0 is the Rashba splitting energy, and $\mathbf{k}_0$ is the momentum shift. The mechanism underlying the improvement in TE efficiency because of Rashba spin-splitting is that each spin-degenerate parabolic band splits into two branches with identical energy values at distant k points, separated by $2k_0$, as illustrated in Fig. 5(e).

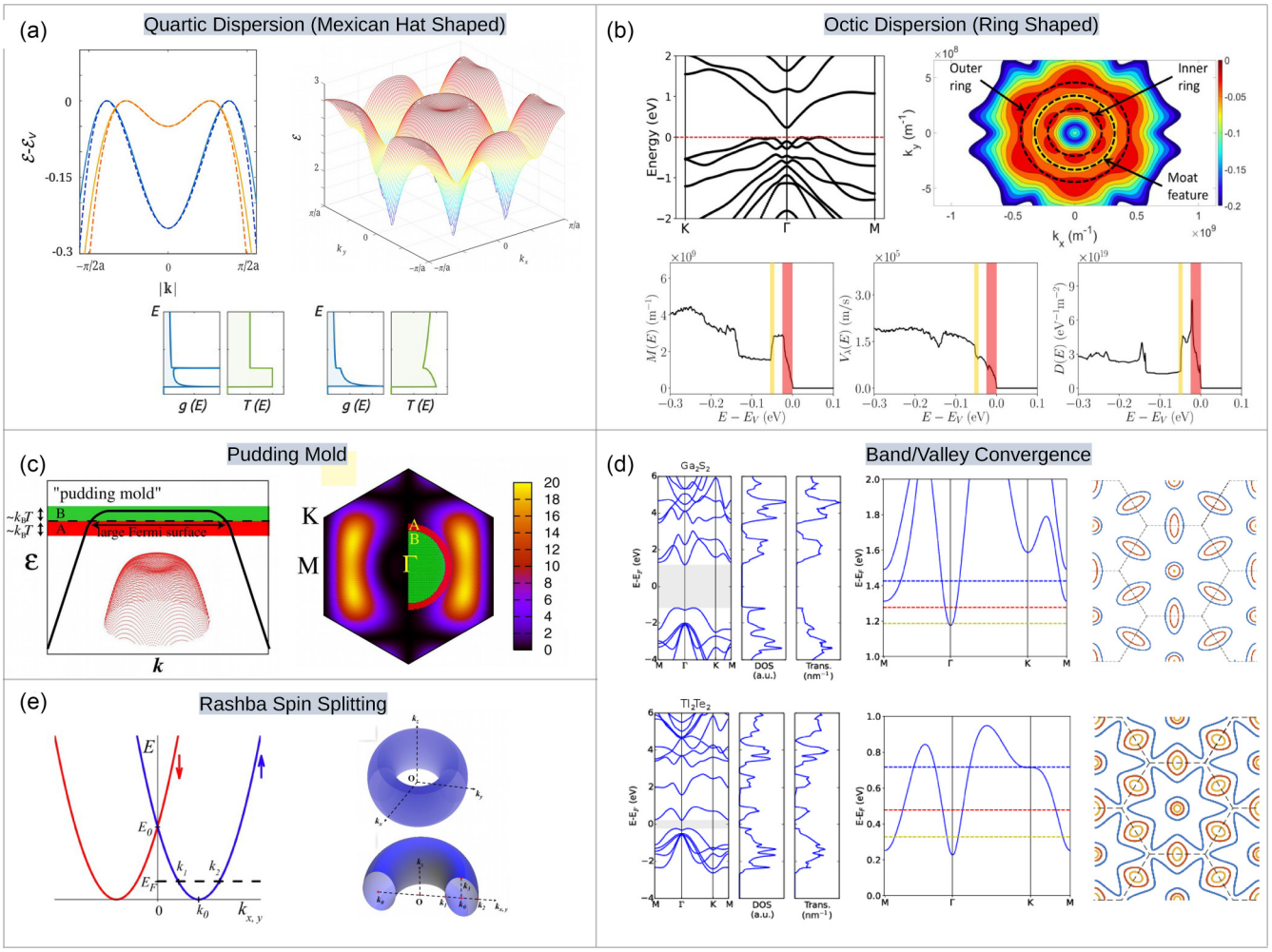


FIG. 5. Schematic representations and properties of band structures that enhance TE efficiency in 2D. (a) MHS band structure, DOS, and electronic transmission spectra of quartic dispersion in 1D and 2D systems. (Reproduced with permission from Ref. [65].) (b) Ring-shaped (octic) electronic band structure, energy contour plot of the valence band, distribution of modes (M), average velocity (V_λ), and DOS (D) versus energy for the valence states. (Reproduced with permission from Ref. [55].) (c) Schematic representation of pudding mold band and contour plot of $[v_x(\boldsymbol{k})]^2$. (Reproduced with permission from Ref. [110].) (d) Electronic band structure, transmission spectra, isoenergy curves, and related isoenergy surfaces near the valence band edge are shown in the first Brillouin zones of GaS and TlTe. (Reproduced with permission from Ref. [66].) (e) Band structure of the Rashba system in the k_z=0 plane for different spins. The Fermi surface with an elliptic-torus shape ($E_F < E_0$) and the ellipse-shaped cross-section of the carrier pocket are shown. (Reproduced with permission from Ref. [111].)

Since the sharp increase in the DOS enhances S, materials with Rashba-type band structures have been considered promising TE candidates.

Previous studies have shown that bulk BiTeI with Rashba spin-splitting bands has exhibited 2D-like TE properties [111]. Similarly, Rashba-type band structures can lead to induce a 1D-like DOS, resulting in significant improvements in S and zT for 2D systems [112–114]. However, only a minor increase has been reported in the n-type S of 2D Janus SbTeI and BiTeI upon inclusion of SOC [115]. Theoretical predictions of Rashba-type band structures in 2D Janus materials have provided a basis for improving their transport properties for TE applications [75,83,116–118].

B. Degeneracies and inter/intravalley scatterings

Orbital, valley, and band degeneracy. Valley and orbital engineering have been widely employed as effective strategies to enhance TE performance. Orbital degeneracy arises when the energy difference between the tops of the VBs or the bottoms of the conduction bands (CBs) of multiple bands lies within a few k_BT. Similarly, valley degeneracy occurs when multiple valleys in the VB (or CB) converge to nearly the same energy, resulting in degenerate hole (or electron) pockets [119]. The number of valleys N_v is directly proportional to the quality factor B, which in turn influences the TE performance. Therefore, both orbital and valley degeneracies contribute to an enhancement in B, thereby improving zT. However, degeneracies have contrasting roles in electronic transport. On the one hand, they increase the number of available conducting channels, which can lead to higher σ. On the other hand, they also introduce additional scattering pathways, which may adversely affect carrier mobility.

In the ballistic limit, where scatterings are negligible, valley convergence enhances DOS and S, as all additional carrier pockets fully contribute to conduction under these conditions.

Among 2D-TMDs, for instance, the H phases of TiS_2, $TiSe_2$, HfS_2, $HfSe_2$, and the 1T phases of ZrO_2 and HfO_2 have been reported to yield high p-type PF owing to nearly degenerate hole valleys located at high-symmetry points [120]. Similarly, GaS exhibits nearly degenerate conduction bands, while TlTe displays almost complete valley degeneracy. Both features primarily lead to enhanced n-type PF, as illustrated in Fig. 5(d) [66]. 2D layered AB_2Te_4 (A = Sn, Pb; B = Sb, Bi) ternary compounds have shown exceptional p-type TE performance, with zT values reaching up to 5.9 at elevated temperatures, owing to the presence of multiple valley degeneracies in their valence bands [121]. Furthermore, the valence band of FeOCl-type ferroelastic SnNX (X = Cl, Br) monolayers exhibits valley degeneracy, resulting in higher p-type S compared to n-type S [122]. It should be noted that in these studies, the carrier relaxation time was estimated without considering inter- or intravalley scattering processes [121,122]. The exploitation of valley or band convergence to improve TE performance via strain engineering has been widely investigated, and relevant studies will be summarized in Sec. V B.

Inter/intravalley scatterings. Valley scatterings play a critical role in determining TE properties of materials. The energy-dependent relaxation time $\tau(E)$ is typically estimated using either the DP approximation or by fully accounting for e–ph interactions. Since the DP approach only includes scattering from longitudinal acoustic phonons, its reliability is limited in materials where other phonon modes contribute significantly. Nevertheless, DP theory can yield accurate predictions of $\tau(E)$ for 2D materials exhibiting horizontal mirror symmetry, such as graphene and semiconducting TMDs in the hexagonal phase. In these materials, the e–ph coupling matrix $g_{mnv}(\mathbf{k}, \mathbf{q})$ is odd because of the symmetry of the Kohn–Sham potential with respect to flexural vibrational modes. Consequently, $g_{mnv}(\mathbf{k}, \mathbf{q})$ vanishes for these modes, suppressing the corresponding scattering events. As a result, DP theory performs better for 2D materials exhibiting trigonal prismatic phase (H-phase). In contrast, for buckled phases or octahedral (T-phase) materials, the DP method often overestimates $\tau(E)$. In a recent study, Wu *et al.* [123] calculated the TE coefficients and efficiency of α- and β-antimonene by explicitly considering e–ph interactions. Because of the buckled geometry and nearly degenerate CB valleys of antimonene, accurate modeling required going beyond the standard DP approximation. Despite these complexities, the Seebeck coefficients obtained from both approaches were comparable, as $\tau(E)$ showed limited energy dependence. However, for β-antimonene, the inclusion of full e–ph coupling led to a significant reduction in zT, from 2.15 to 0.37, primarily because of decreased σ. Although strain engineering is commonly employed to induce valley degeneracy, it can also be used to suppress valley convergence in specific cases. For example, in arsenene, the application of 2% uniaxial strain reduces six-fold multivalley degeneracy to a twofold configuration, leading to a decrease in intervalley scattering and enhanced charge carrier mobility [124]. Such improvements in mobility and σ are expected for buckled group-V monolayers. Concordantly, strong intervalley e–ph coupling has been shown to reduce the TE performance of group-IV and group-V elemental monolayers [125]. For instance, in stanene, electron mobility calculated using the BTE with full e–ph interaction is three orders of magnitude lower than that predicted by DP theory [126].

Sb_2Te_2Se monolayer emerges as an outperforming candidate for efficient TE applications, showcasing remarkably high zT values for both p-type and n-type behavior. Specifically, it exhibits exceptional p-type and n-type zT values of 1.28 and 1.86/2.99/3.75 at 300 K [126]. Regarding SnS_2, incorporating comprehensive mode-resolved e–ph couplings into calculations, the predicted electron mobility turns out to be approximately 15 times lower compared to estimations derived solely from the DP theory. This revised approach aligns more closely with experimental findings [127–129]. Notably, the highest zT of 0.43 is attained at 700 K, where the full e–ph coupling matrix elements have been used. Chen *et al.* have recently reported that monolayer InP_3 exhibits maximum zT values of 0.37 for n-type doping and 0.18 for p-type doping at room temperature, which are an order of magnitude lower than those predicted using DP theory [130]. In summary, valley/band degeneracy is beneficial for TE efficiency only under certain conditions. The enhancement of TE efficiency depends strongly on the interplay between the S and the σ.

V. STRATEGIES FOR ENHANCING ELECTRONIC PROPERTIES

A. Nanostructuring

Nanopores. Nanostructuring presents an effective pathway to optimize the electronic transport properties of 2D materials for TE applications. A promising approach to nanostructuring in two dimensions involves introducing periodic holes into the structure to form an antidot lattice. It has been demonstrated that graphene can be engineered into a semiconducting material, with a band gap tunable through modifications to its geometrical features of the antidot lattice [131–134]. The incorporation of an antidot lattice not only induces a finite band gap—an essential factor for enhancing thermopower—but also suppresses TC, thereby further improving TE efficiency [60,135]. Detailed calculations have indicated that hexagonal antidot lattices with clean armchair edges exhibit higher zT values, whereas structures with zigzag edges result in significantly lower performance [136]. Additionally, triangular antidot lattices have been found to yield the lowest TC, while isotriangular lattices exhibit the highest PF and zT [137]. Moreover, broken symmetry has been reported to induce a dimensional crossover, where quasi-1D electron states emerge within 2D antidot lattices. These states lead to a stepwise electron transmission spectrum, thereby enhancing both S and zT [60].

The influence of nanopore arrays on the TE properties of quasi-1D graphene nanoribbons (GNRs) has also been extensively investigated [135,138–140]. It has been found that ribbon width plays a crucial role in these structures, as electronic conduction is dominated by edge states [135]. The optimization of TE performance in graphene antidot lattices (GALs) is further complicated by the multitude of geometrical parameters that influence their properties. To address this complexity, Yamawaki *et al.* employed a Bayesian optimization approach and demonstrated that their method could enhance zT by a factor of up to 11 [139]. Experimental studies

have also confirmed the opening of a band gap in graphene antidot lattices. Oh *et al.* fabricated large-area single- and bilayer-graphene nanomeshes with sub-10-nm neck widths using block copolymer self-assembly. Their findings revealed a significant reduction in TC to 78 $W\,m^{-1}K^{-1}$ and an increase in thermopower, reaching values as high as 520 $\mu V/K$ [141]. These results highlight the potential of GALs for fine-tuning both electronic and phononic properties, thereby enhancing the TE performance of graphene sheets.

Heterostructures and superlattices. The construction of heterostructures and superlattices presents a compelling strategy for tailoring the electronic and phononic transport properties of 2D materials, thereby enhancing their TE performance. Among the most studied systems are in-plane graphene/hexagonal boron nitride (hBN) heterostructures, owing to their structural commensurability and nearly identical lattice constants, which makes them ideal candidates for constructing 2D in-plane heterostructures, such as superlattices and hBN islands embedded within a graphene host, or vice versa [142–145]. Beyond their potential for band gap engineering, lateral graphene/hBN heterostructures have been extensively studied for their ability to tune electronic and thermal properties to optimize TE performance [146–154]. Computational studies on the TC of hBN/graphene heterostructures have explored configurations featuring embedded dopant dots or superlattice stripes. In all cases, TC was found to decrease substantially. Specifically, when the diameter of embedded hBN inclusions ranged from 2 to 8 nm, TC was reduced by up to 65% [147]. The maximum reduction in TC was reported for 50% hBN content [147,153]. Furthermore, in stripe-based superlattices, the zigzag interface geometry exhibited a higher TC than the armchair interface [153]. The optimal supercell size for minimizing thermal conductance was found to be smaller than the phonon mean free path, a phenomenon attributed to phonon localization effects [151]. In addition to suppressing lattice thermal conductivity (κ_l), the superlattice geometry has been shown to enhance S [149]. A 20-fold enhancement in S was reported for zigzag nanoribbons, attributed to the formation of a pudding-mold-type band structure in the superlattice [149]. Similarly, in armchair-edged structures, zT was found to increase by 10–20 times compared to pristine structures, an effect linked to the emergence of partially flat electronic bands [148]. Beyond lateral configurations, graphene/hBN van der Waals (vdW) heterostructures also exhibit promising TE properties. Experimental studies have demonstrated that graphene's thermopower doubles when placed on hBN instead of SiO_2 [154], underscoring the potential of hBN as a substrate for enhancing graphene's TE performance.

Other heteorstructuring routes, beyond graphene/hBN systems, were also investigated. Numerous studies have explored various hybridization techniques to enhance TE efficiency, primarily focusing on optimizing σ while preserving or improving S [155–160]. One widely studied approach involves integrating graphene or reduced graphene oxide (rGO) with TMDs [156,157], Bi_2Te_3 [158], or InSb [159]. Additionally, alternative materials and configurations have been explored, including the construction of MXene-organic superlattices [160], bilayer germanium-based monochalcogenides [161], and the incorporation of multilayers and thin films of $PtSe_2$ [155]. These strategies highlight the versatility of heterostructure-based engineering in tailoring 2D materials for high-performance TE applications.

Nanoribbons. Reducing the dimensionality of a material inherently enhances its TE properties by inducing quantum confinement effects. Beyond this intrinsic advantage, various engineering techniques have been employed to further optimize the transport and TE performance of nanoribbons (NRs), including contemporary enhancement strategies.

Graphene nanoribbons (GNRs) are the most extensively studied quasi-1D structures for TE applications. Their reduced dimensionality grants significant advantages over graphene, including band gap opening and enhanced quantum confinement effect [162]. Recent studies have explored geometry-based modifications to further enhance TE performance of GNRs. For example, inline and staggered armchair-GNR heterostructures have been simulated, revealing that all-metallic armchair-GNR backbones transition into semiconductors with increased zT values [163]. Combinations of engineering schemes were also employed, like the hybridization of geometrical effect and clusters of isotopes to scatter long wavelength phonons, which was predicted to result in highly efficient TE conversion [164].

Various structural modifications have also been employed to optimize phonon transport while preserving electronic transport characteristics. Techniques such as hybridization with BN, edge disorder, antidot patterning, edge roughness, and strain engineering have been shown to significantly reduce κ_l while maintaining a high PF, thus enhancing zT [148,165–170].

Beyond single-layer GNRs, bilayer structures provide additional degrees of freedom for TE optimization. Deng *et al.* studied twisted bilayer GNRs at different twist angles and predicted zT values exceeding 2 at optimized chemical potentials [171]. Similarly, a comparative study on bilayer GNR junctions with and without nanopores showed that vdW interactions between layers reduce κ_l, while hole engineering enhances the PF [172]. While perfect GNRs exhibit low TE performance ($zT = 0.19$), introducing structural modifications led to significantly higher values, $zT = 9.65$ and 5.55 for n- and p-type doping, respectively. Incorporating vertical heterojunctions has also been explored as an alternative strategy. For instance, GNR arrays stacked on MoS_2 substrates and as-grown suspended GNRs exhibit enhanced TE coefficients [173,174].

Edge engineering has been extensively investigated as a means to increase TE efficiency. This approach has been applied to GNRs, BN-NRs, and silicene NRs. Notably, wide silicene NRs exhibit high zT values under heavy doping conditions [175]. Similarly, nitrogenated holey GNRs were predicted to achieve $zT \sim 1.5$ at room temperature [176]. BN-NRs, hydrogenated BN-NRs, and phosphorene NRs have also emerged as promising candidates, with phosphorene NRs reaching a maximum zT of 6.4 at room temperature under n-type doping [177–179]. Furthermore, tuning boundary potentials in zigzag phosphorene NRs has been shown to double the value of S [180].

TE properties of TMD NRs have garnered considerable interest, owing to the remarkable TE performance observed in their 2D counterparts. Studies on MoS_2 NRs have shown that

TABLE I. Enhanced TE coefficients of 2D materials through nanostructuring.

2D-material	S_{enh}(p/n) (μV/K)	PF_{enh}(p/n) (W m^{-1}K^{-2})	zT_{enh}(p/n)	κ_l (W m^{-1}K^{-1})	T (K)
Graphene antidot lattice [60]		$0.22/0.22 \times 10^{-3}$	0.94	0.058	300
Graphene nano-mesh [141]	$-/520 \pm 92$	8.2×10^{-3}			520
Graphene/h-BN/graphene [146]	$-/99.3$	$1.51(W/K^2) \times 10^{-15}$	1.0510^{-6}		300
GNR [165]	30	1.80×10^{-15}(W/K)	$\geqslant 0.1$		420
Twisted bilayer GNR [171]	750		2/2.7	0.0034(nW/K)	300
Bilayer GNR junction [172]	0.39/0.38		5.55/9.65	0.0032(nW/K)	300
Wide-silicene [175]	247/217		2.56/1.02	0.315(nW/K)	300
Phosphorene NR [177]	343.1/431.3	$1.01 \times 10^{-2}/2.49 \times 10^{-2}$	2.3/4.5	0.67	300
$PtSe_2/PtSe_2$ [155]	90.3	50×10^{-6}	5×10^{-5}	9.33	300
MoS2-NR [181]	223/204	0.071/0.032	3.4/2.5	1.02	300
HfSe2-NR [184]	2.25/2.45	0.83/1.47	0.94/1.55	0.21	300
WS2-WSe2-NR [186]	62.5×10^{-3}	580	4.13	0.61	300

both p- and n-type zT values can reach 3.4 and 2.5, respectively, because of their intrinsically low κ_l at 300 K [181,182]. Similarly, WSe_2 NRs exhibit a relatively high zT value of 1.4 [183]. The reduction in dimensionality plays a particularly significant role in enhancing TE properties, as demonstrated in 1T-$HfSe_2$ NRs, where the zT for p-type doping is enhanced by a factor of four at room temperature, attributed to reduced phonon scattering [184]. Moreover, engineering strategies, such as the introduction of pillars or branches, have been shown to improve the zT of MoS_2 NRs, with values increasing from 0.72 to 1.93 [185].

Janus and superlattice structures of WS_2-WSe_2 NRs have exhibited exceptional TE performance, with predicted zT values of 4.13 and 5.47, respectively [186]. This enhancement is attributed to a combination of high carrier mobility and low phonon lifetime, optimizing electrical transport while simultaneously suppressing TC. Similarly, hybrid TMD NRs, such as those composed of MoS_2 and WS_2, have demonstrated outstanding TE efficiency, with a reported zT of 5.5 at 600 K [187]. Furthermore, the $MoS_2/MoSe_2$ heterostructure exhibits even higher zT values, reaching 7.4 at 800 K [188], positioning it as one of the most promising TMD-based materials for TE applications.

The impact of edge roughness and sulfur vacancies on the TE properties of MoS_2 NRs has also been studied using the non-equilibrium Green's function method [189]. These studies indicate that introducing sulfur vacancies significantly enhances TE performance, increasing the maximum zT values to 3 for n-type and 4 for p-type doping at 500 K.

Table I summarizes the lattice thermal conductivities and the enhanced electronic TE coefficients reported for various 2D materials. These findings underscore the effectiveness of nanostructuring strategies in optimizing TE performance by tailoring both electronic and phononic properties.

B. Strain engineering

Strain engineering is a widely employed technique for modifying valley and band degeneracy by subtly adjusting lattice parameters. In addition to its impact on electronic properties, strain-induced reductions in κ_l contribute to enhanced TE performance. This section summarizes key studies investigating the role of strain in improving the TE efficiency of 2D materials.

The TE performance of well-known 2D TMDs, specifically MX_2 monolayers (M = Mo, W; X = S, Se, Te), can be significantly enhanced through the application of strain [190–192]. In addition to improving electronic TE coefficients and zT values, strain also reduces κ_l, further boosting TE efficiency [193,194]. Local lattice distortion induced by strain has been shown to increase carrier mobility in 2D MoS_2 [195]. In particular, rippled MoS_2 exhibits higher mobility compared to its flat counterpart, which weakens the interdependence between S and σ, resulting in an increased PF. Although vdW heterostructures, such as MoS_2/WS_2, generally possess lower zT values compared to their monolayer counterparts, studies have shown that their TE performance can be slightly enhanced by biaxial strain [196].

Electron and phonon transport analyses have been conducted to investigate the effect of strain on the TE properties of Hf, Zr, and Ti-based TMD monolayers [197–200]. Biaxial tensile strain applied to ZrX_2 monolayers has been shown to significantly enhance TE efficiency, yielding zT values around 2, primarily the result of a reduction in κ_l and an increase in PF [201,202]. Among these, $ZrSe_2$ exhibits exceptional performance under 7.5% tensile strain, achieving a zT of approximately 3.84, which is a twofold increase compared to its unstrained counterpart [203]. In addition to binary TMDs, the TE coefficients of anisotropic MX_3 monolayers, such as TiS_3 and ZrS_3, are also sensitive to applied stress [204,205]. In TiS_3, the enhancement of σ nearly doubles the PF, while in ZrS_3, the zT increases to 0.7, driven by suppressed κ_l.

The TE properties of Janus derivatives of TMDs can also be tuned via strain engineering. The introduction of strain induces valley degeneracy and flat electronic bands, significantly enhancing the zT of PtSSe and WSSe [206,207]. Among various MXY systems (M = Zr, Hf, Pt; X/Y = S, Se), the ZrSSe-HfSSe vdW heterostructure has been identified as the most promising TE candidate owing to its PF under strain [208].

Among the group III-nitrides, monolayers of BN, AlN, and GaN have been reported to exhibit relatively low zT values. However, h-InN stands out as a promising TE candidate owing to its relatively high electrical conductivity and low

TC. Notably, for *p*-type h-InN, the zT value can reach 1.3 at elevated temperatures under compressive strain [209]. This enhancement is attributed to a band convergence effect in the valence band, which significantly increases the PF, while simultaneously reducing κ_l at low compressive strain.

Introducing band degeneracy through compressive strain has been shown to maximize the TE efficiency of monolayer InSe, achieving a zT value of 0.46 [210]. Additionally, the effect of tensile strain on κ_l of InSe has been investigated, revealing a reduction from 25.9 W/mK to 13.1 W/mK at 300 K [211]. As a result of this suppressed κ_l, zT exceeds 0.40 under increasing tensile strain. For InSe/GaSe superlattices, *p*-type TE performance has been significantly enhanced under compressive strain, attributed to the synergistic effect of a high Seebeck coefficient (S) and low κ_l [212]. Furthermore, in the ballistic limit, the InTe monolayer achieves the maximum zT value of 2.7 when subjected to 8% tensile strain [213].

The effect of strain on the TE properties of anisotropic 2D group IV-chalcogenides has been extensively investigated using *ab initio* methods. Notably, the heterobilayer SnS/SnSe exhibits a high PF under in-plane compressive strain, driven by an increase in both σ and S [214]. Significant strain-induced improvements in zT have been reported for both monolayer and bilayer SnS [215,216]. In the monolayer case, the increase in zT is attributed to low κ_e and high PF, while for the bilayer counterpart, the enhancement is driven by low κ_l and high PF. Similarly, the electronic TE properties of GeSe and SnTe have been shown to improve under compressive strain [217,218]. Additionally, tensile biaxial strain has been reported to boost the TE performance of puckered Si_2SeS, yielding a zT of 2.55 at room temperature [219].

Tensile strain has been shown to significantly enhance the TE efficiency of Se_2Te and $SeTe_2$ monolayers [220]. For *p*-type doped Bi_2O_2Se monolayers, the zT increases to 1.14 under 2% tensile strain at 300 K and reaches as high as 4.22 at 800 K [221]. Similarly, in hydrogenated Sn_2Bi monolayers, the combination of high PF and low κ_l results in an *n*-type zT of 1.03 at 700 K under 2.5% strain [222]. Strain engineering has also been applied to mono-elemental hexagonal tellurium (α-Te, space group $P\bar{3}m1$) and its α' phase (P2 space group), both of which exhibit enhanced zT values of 0.94 and 1.18 under strain, respectively [223,224]. Notably, α'-Te reaches its maximum efficiency at 800 K with a zT of 6.07 [224]. Beyond chalcogenides, strain engineering has been utilized to optimize the TE performance of elemental analogues of graphene, including phosphorene, silicene, germanene, and stanene [225–228]. Another promising elemental 2D material, antimonene, exhibits a strain-engineered zT value of 1.2 at room temperature, highlighting its potential for TE applications [229]. Applying 2% tensile strain to a SnI_2 (tin iodide) monolayer leads to a considerable improvement in zT because of the combined effect of phonon softening and valley degeneracy [230]. A similar synergistic effect resulting from compressive strain enhances the *n*-type zT of penta-PdSeTe from 0.84 to 1.24 at 700 K along the y direction [231]. Ozbal *et al.* recently showed that band gap opening and reduction in lattice thermal conductance under biaxial tensile strain make the carbon biphenylene network a promising material for TE applications [232].

As summarized in Table II, strain engineering has emerged as a powerful strategy for improving zT of 2D materials, primarily by increasing the PF and suppressing κ_l. Despite these advantages, the practical realization of the required strains remains an open direction for future work.

C. Edge/surface functionalization

Surface functionalization plays a crucial role in modifying the properties of 2D materials because of their inherently high surface-to-volume ratio. By introducing functional groups, it is possible to tailor electronic properties such as band structure, DOS, and carrier mobility. Moreover, thermal transport characteristics are strongly influenced by the type and concentration of surface functional groups. As a result, surface functionalization offers a versatile strategy for optimizing TE transport coefficients, ultimately enhancing TE efficiency.

The effects of surface functionalization have been extensively investigated in graphene-based structures. In particular, the diverse electronic and thermal modifications induced by functional groups have motivated various strategies to enhance TE performance through chemical modification [235–242]. Graphene oxide (GO) contains epoxide groups (oxygen atoms bridging two neighboring carbons), as well as carbonyl and hydroxyl functionalities. Molecular dynamics (MD) simulations predict that room-temperature TC is reduced by a factor of 25 upon functionalization with epoxy, hydroxyl, and ether groups [237]. Although such suppression of TC is advantageous for improving zT, oxidation also severely degrades electronic conductivity. To mitigate this effect, reduced graphene oxide (rGO) is produced through thermal annealing, which partially restores electronic conduction. While rGO exhibits higher TC than GO, it remains approximately five times lower than that of pristine graphene [241]. Experimentally, oxygen plasma treatment has been shown to open a bandgap and significantly enhance thermopower while preserving high electrical conductivity [243].

The functionalization of graphene with larger side groups has also been studied in detail. Thermal transport can be effectively modulated by the selection of appropriate functional groups, where phonon confinement and molecular antiresonances play critical roles [238,239]. Furthermore, patterned functionalization has emerged as a promising method for substantial zT enhancement [235,236]. This approach enables the formation of sharp DOS features near the band edge, boosting thermopower while simultaneously reducing lattice thermal conductivity. Computational studies predict up to a two-order-of-magnitude increase in zT through patterned functionalization [236]. Additionally, molecular functionalization has been shown to enhance the PF in few-layer graphene by inducing bandgap opening and band flattening [244].

MXenes, a class of 2D transition metal carbides and nitrides, are derived from MAX phases—a family of layered metallic solids. While MAX phases generally exhibit poor TE performance because of their intrinsic metallic nature, their exfoliated counterparts, MXenes, can display either metallic or semiconducting behavior depending on surface termination or functionalization. This tunability suggests that MXenes may achieve significantly enhanced TE

TABLE II. Enhanced TE coefficients of 2D materials through strain engineering.

2D-material	S_{enh}(p/n) (μV/K)	PF_{enh}(p/n) ($W\,m^{-1}K^{-2}$)	zT_{enh}(p/n)	κ_l ($W\,m^{-1}K^{-1}$)	T (K)
WS_2 [190]	922/1029	$12\tau_p/59\tau_n \times 10^{10}$	0.43/0.72		900
$HfSe_2$ [197]			2.5/-	0.74	300
HfS_2 [198]		$29.5/22.9 \times 10^{-3}$	3.35/2.29	1.12	300
ZrS_2 [201]	370/370		5.1/5.1	0.24	800
$ZrSe_2$ [203]	725/725		3.84/4.58	0.94	300
WSSe [206]		$50.2/12.1 \times 10^{-6}$	1.08/1.06		1500
h-InN [209]	700/350	6.9×10^{-3}/-	0.50/-	6.77	300
InSe [210]	36/5		0.46/0.03	27.79	300
InTe [213]	1520/1330		2.7/-	$0.087 \times 10^9 (W/m^2K)$	300
SnS [215]		1.1/0.5	2.4/1.3	0.087∼3.60	300
SnS-SnS [216]	2270	172×10^{-3}	4.96	0.21–3.23	300
Si_2SSe [219]	2147		2.55[a]		300
Bi_2O_2Se [221]	560/240	$3.79/1.79 \times 10^{-3}$	1.14/0.53	0.48	300
Sn_2Bi [222]	127/176	$3.21/47.16 \times 10^{-3}$	0.51/0.88	0.59	300
SnI_2 [230]	373/279	$3.24/0.97 \times 10^{-3}$	3.05/1.22	0.14	300
αTe [223]			−/2.03	4.3	700
Silicene [225]	58/56	$8.3/8.4 \times 10^{-3}$	−/2.03	∼1.4	1200
H-Germanene [226]	1063/1021	$12.6/57.2 \times 10^{10}\,W/mK^2s$			800
aw-Antimonene [229]	−/500	$-/900 \times 10^{-3}$	−/0.9	0.18	800
La_2GeI_2 [233]	978/-		1.09	1.23	300
SiH [234]	−/144/-		2.83	0.28	700

[a] zT_e.

performance compared to their bulk MAX phase precursors. Indeed, several semiconducting MXene structures—Sc_2CF_2, $Sc_2C(OH)_2$, Sc_2CO_2, Ti_2CO_2, Zr_2CO_2, and Hf_2CO_2—have been reported to exhibit high thermopower values exceeding 1140 μV/K at temperatures around 100 K [245]. Furthermore, functionalized Mo_2C has demonstrated a superior PF when terminated with F, OH, or H groups. The underlying mechanism responsible for this enhancement is attributed to the coexistence of flat and dispersive electronic bands, where flat bands contribute to large thermopower and dispersive bands support high electrical conductivity [246].

The advantages of Mo-based MXenes have been experimentally demonstrated, showing high electrical conductivity and *n*-type thermopower following heat treatment [247]. In contrast, hydrothermal treatment of Ti-based MXenes has been found to significantly modify surface characteristics, leading to a threefold enhancement in thermopower. For $CrTiC_2$ and Cr_2TiC_2 functionalized with F and OH groups, surface termination has been shown to lower lattice thermal conductivity, resulting in predicted zT values as high as 3 at 600 K [248]. A comprehensive study on the structural effects in M_2CO_2 MXenes (M = Ti, Zr, Hf, Sc) revealed that the oxygen adsorption site plays a critical role, with the potential to enhance TE performance by up to 40% [249]. This improvement is strongly dependent on the symmetry of surface terminations on opposite faces. Moreover, the presence of flat valence bands was reported to induce a large bandgap, thereby enhancing thermopower and yielding a zT of up to 1.1 at room temperature [249]. Recently, Jing *et al.* conducted high-throughput simulations on the electronic and phononic transport properties of 225 double-transition-metal o-MXenes with various metal combinations. Caclulating the e-ph couplings, they systematically investigated the influence of surface terminations and structural configurations [250]. The study identified the majority of o-MXenes as promising TE materials, with zT values exceeding 0.5, as illustrated in Fig. 6. Collectively, these studies underscore the critical role of surface termination and functionalization in tuning both the electronic and thermal transport properties, thereby significantly influencing the overall TE performance of MXenes.

In a similar manner, hydrogenation induces significant modifications in both the electronic and vibrational properties of 2D materials. In mono- and multilayer silicene, the zT value improves primarily because of the bandgap opening induced by hydrogenation [251,252]. A notable zT of 2.2 has been reported for hydrogenated silicene under *n*-type doping at 800 K, attributed to reduced thermal conductivity and enhanced S [252]. Likewise, the zT value of hydrogenated graphenylene increases to 1.66, surpassing the value of pristine graphenylene, which stands at 0.49 [253]. Moreover, the combined effects of layer number and hydrogenation ratio on the electronic contribution to zT have been explored, taking into account the inherent geometric anisotropy [251]. Li *et al.* reported that single-layer silicene with 66.7% and 100% hydrogenation ratios yields the highest *p*- and *n*-type electronic zT values. Following the confirmation of bandgap opening in hydrogenated germanene and the structural stability of hydrogenated Sn_2Bi monolayers, their TE performance has been further enhanced through strain engineering [222,226]. Another example is Si_2BiN, which initially exhibits metallic behavior but undergoes a semiconductor transition upon hydrogenation and oxidation. While pristine Si_2BiN shows poor TE performance, its oxidized form achieves a high zT of 0.99 at 300 K [254].

Recent studies have also highlighted the critical role of functional group mass in reducing phonon thermal

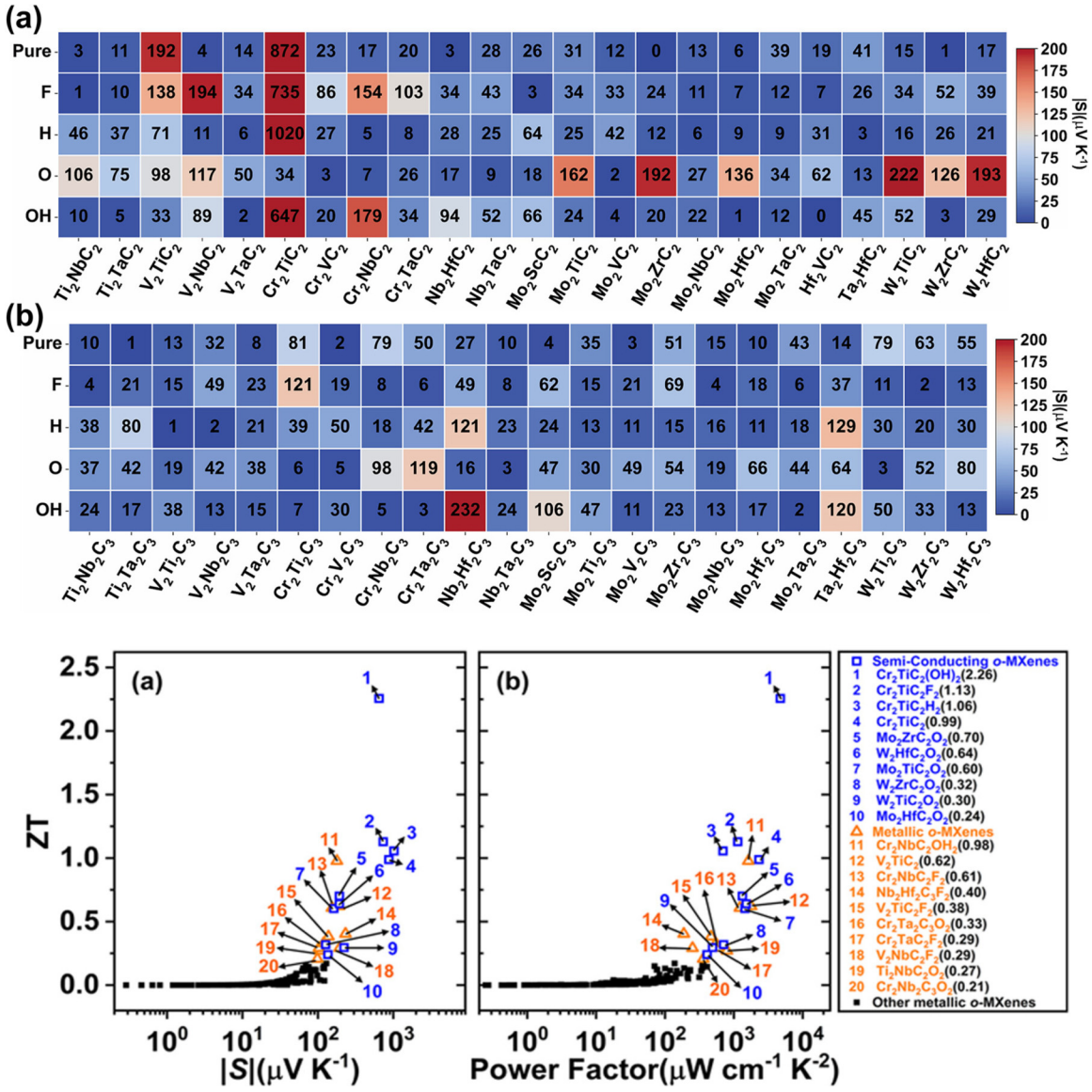


FIG. 6. Surface terminations give rise to high S and zT of double-transition-metal o-MXenes. Absolute Seebeck coefficients of double-transition-metal o-MXenes at 300 K are shown for "212" and "223" type structures are shown in (a) and (b). In the lower panel, predicted Seebeck coefficients (a), and power factors (b) are plotted as functions of TE figure of merit (zT) for 225 double-transition-metal o-MXenes at 300 K. The blue and orange colors represent semiconducting and metallic o-MXenes with zT values larger than 0.2, respectively. The black marks represent other metallic o-MXenes with zT values lower than 0.2. Reproduced with permission from Ref. [250].

conductivity and optimizing zT. In carbon-based diamane, functionalization with chlorine, hydrogen, and fluorine has been investigated, revealing that chlorine-functionalized diamane exhibits the lowest κ_l among the three, owing to the heavier atomic mass of chlorine [254]. It was also shown that surface functionalization with a selected variety of molecular adsorbates that have different vibrational spectra result in a more effective suppression of phonon transport and could enhance TE efficiency [239].

Among hydrogenated group IV–V X_2Y compounds, Si_2BiH_2, Si_2SbH_2, and Si_2AsH_2, display zT values exceeding 2 at room temperature. This enhancement is primarily attributed to their intrinsically low κ_l [255]. In line with these findings, hydrogenation and fluorination of black phosphorus monolayers have been shown to effectively suppress phonon thermal transport. However, the concurrent reduction in carrier mobility limits the overall gain in TE performance [256]. Furthermore, a recent study demonstrated that Ni-doped $HfSe_2$ monolayers can reach a zT value of 3.09 at 300 K, emphasizing the importance of selective chemical adsorption as a strategy for improving TE efficiency [257].

A list of representative materials whose zT values have been enhanced through edge and surface functionalization is provided in Table III.

D. Defects and vacancies

Naturally occurring defects in crystals play a critical role in determining both electronic and phononic transport properties of materials. For phonons, defects act as scattering centers,

TABLE III. Enhanced TE coefficients of 2D materials through edge and surface functionalization.

2D-material	S_{enh}(p/n) (μV/K)	PF_{enh}(p/n) (W m^{-1}K^{-2})	zT_{enh}(p/n)	κ_l (W m^{-1}K^{-1})	T (K)
GONRDs[a] [235]	127.1–287.3	3.9–18.9 × 10^5 W/m^2 K^2	0.05/0.75	0.6–1.0	800
Graphene [243]	69.55	3.41 × 10^{-3}	6.24 × 10^{-3}		295
o-MXenes [250]	< 100		< 0.5		300
$Cr_2TiC_2(OH)_2$ [250]	~640	~487.5 × 10^{-3}	2.26	12.4	300
$Mo_2TiC_2T_x$ [247]	−/47.3	3.09 × 10^{-4}			803
$Cr_2TiC_2(OH)_2$ [250]	>600/ ⩽ 400	749.1 × 10^{-3}	~3	6.5	600
Ti_2CO_2 [249]	750/750		~1	18.42	300
H-silicene [251]	>200		~1		200-400
Si_2BiH_2 [255]	−/320	-/15.66 × 10^{-3}	−/2.85	0.09	300
F-BP [256]			0.321/-	10.8	300
Ni-$HfSe_2$ [257]		1.68/85.06 × 10^{-3}	3.09	1.17	300

[a]Graphene oxide nanorods.

effectively reducing κ_l. In terms of charge carriers, defects not only serve as scattering sites but also alter the electronic structure, potentially enhancing S. As a result, evaluating the net influence of defects on TE performance is a complex task that depends strongly on the type, concentration, and spatial distribution of the defects. Defect engineering aims to optimize this overall impact by introducing specific defect types at controlled concentrations and, in some cases, arranging them in deliberate geometrical configurations. The primary objective in such approaches is to achieve substantial suppression of κ_l while maintaining or enhancing PF. By carefully tailoring defect characteristics, it is possible to shift the balance between electronic and phononic contributions in favor of improved TE efficiency.

MoS_2 is a widely studied material for TE applications because of its large effective mass and low κ_l. Interest in defect incorporation has grown as means to enhance its TE efficiency [258–265]. Sulfur vacancies are naturally present in MoS_2, and their presence induces phonon localization, leading to a drastic reduction in TC [261,262,265]. However, p-type zT remains unaffected, while n-type zT is reduced in the presence of these vacancies [265]. Similarly, Se vacancies in $MoSe_2$ have been shown to reduce the PF, which is attributed to the dangling bonds around the defect sites [264]. Enhancement of zT has been reported for MoS_2/a-MoO_3 nanosheets [258], where MoO_3 optimizes the electronic properties. High-resolution TEM images confirm a 97% increase in electrical conductivity compared to pristine MoS_2. A similar mechanism has been observed in MoS_2/hBN heterostructures, where n-type MoS_2 supported by h-BN exhibits S-vacancy-induced Kondo hybridization, leading to a two order of magnitude enhancement in PF [260].

The impact of defects on the TE performance of graphene has been extensively investigated [243,266–272]. Exposure to oxygen plasma introduces structural defects in graphene, which has been shown to reduce the thermopower because of the increased defect density [269]. However, at sufficiently high defect concentrations, the reduction in κ_l outweighs the degradation in electronic transport, resulting in a threefold enhancement in zT relative to pristine graphene [270]. An alternative strategy involves healing the defected structure via atomic layer deposition following oxygen plasma treatment. This process not only restores κ_l but also significantly enhances the σ and PF. As a result, the zT value was reported to be 4.8 times higher than those previously measured in similar systems [243]. In graphene synthesized by chemical vapor deposition, the presence of high-angle tilt boundary domains has been found to enhance S and suppress κ_l [266]. The increase in S is attributed to energy filtering, whereby low-energy carriers are selectively scattered, allowing higher-energy carriers to dominate transport. Furthermore, the spatial distribution of defects plays a critical role in quasi-one-dimensional systems. In γ-graphyne NRs, for instance, a Bayesian optimization algorithm was employed to determine the defect configuration that yields the highest TE efficiency. The optimized configuration led to a fivefold increase in zT relative to the pristine structure [272].

Sn vacancies in SnS and SnSe have been found to enhance PF and suppress κ_l, leading to zT values as high as 0.8 at 873 K for SnSe [273,274]. Similarly, oxygen vacancies in MoO_3 have been shown to introduce a sharp peak in the DOS near the Fermi level, which contributes to an enhanced zT [275]. Substitutional defects in BAs and point defects in WTe_2 have also been reported to improve TE performance [276,277]. Recently, the TE PF of 2D PdPS with a thickness of 9.1 nm has been improved to 0.648 mWm^{-1} K^{-2} at 300 K through precise control of multifunctional native defect formation via annealing treatment [278]. Similarly, in 2D MXene $Ti_3C_2T_x$, the creation of oxygen vacancies through electrochemical regulation has been shown to significantly enhance electrical conductivity without degrading S [279].

It is also important to note that defect engineering strategies are not limited to 2D sheets; they are equally applicable to NRs, where they have been effectively used to improve TE properties [135,280–289].

Table IV summarizes the reported enhancements in S, PF, and zT for a variety of 2D materials, achieved through the controlled introduction of defects and vacancies.

E. Gating and doping

Field-effect carrier doping is an effective tool for precisely tuning carrier density under the control of a gate voltage. This approach offers several key advantages. Firstly, it preserves the intrinsic dependence of TE properties on carrier concentration, which may arise from disorder, structural

TABLE IV. Enhanced TE coefficients of 2D materials through introducing defects vacancy.

2D-material	S_{enh}(p/n) (μV/K)	PF_{enh}(p/n) ($W\,m^{-1}K^{-2}$)	zT_{enh}(p/n)	κ_l ($W\,m^{-1}K^{-1}$)	T (K)
$MoS_2\alpha MoO_3$ [258]	474	448.4×10^{-6}	1.18	0.16	600
Graphene [266]	50.1	4.12×10^{-3}	3.78×10^{-3}	369	350
HG [267]	645.67/1662.59	$5.69/6.44\,W/mK^2s \times 10^{11}$	0.89/0.89	369	800
SnSe [273]	430	0.9×10^{-3}	2.4	0.22	800
SnS [274]	284	0.46×10^{-3}	0.8	0.43	873
3A-TGNR-3 [280]	223	$1.15 \times 10^{-12}\,W/K^2$	1.11	0.54 nW/K	600

deformations, and environmental influences. Secondly, it allows for continuous and precise modulation of carrier density by controlling the Fermi level. Finally, it enables the adjustment of S through gate voltage variation. Experimental studies have demonstrated the effectiveness of electric-double-layer transistor configurations in evaluating TE properties of trilayer WSe_2 and black phosphorus, revealing high-S and PF values [290,291]. More recent measurements show that thin-film WSe_2 exhibits high S values for both n- and p-type doping, reaching 500 and 950 μV/K, respectively, at 300 K [38].

Extensive efforts have been devoted to optimizing TE coefficients in low-dimensional materials via chemical doping [292–295]. A recent study has demonstrated that Ni doping in MoS_2 simultaneously increases σ and reduces κ [295]. However, the accompanying reduction in S resulted in lower zT values compared to undoped MoS_2. In contrast, optimized Cu doping in MoS_2 at 420 K yielded the highest σ and PF [292]. Similarly, Nb doping has also emerged as an effective strategy for simultaneously enhancing both S and σ in MoS_2 [293,296–298]. Very recently, Nb-doped thin MoS_2 (8 nm) has demonstrated outstanding bulk conductivity of up to $360 \pm 30\,S\,cm^{-1}$ and a peak PF of $370 \pm 80\,\mu W\,m^{-1}\,K^{-2}$ at room temperature [297].

In ZnO thin films, Ga doping has been found to enhance the TE coefficients [294]. The increase in σ caused by Ga impurities is accompanied by a rise in the DOS, which mitigates the typical reduction in the S. Consequently, PF reaches $256\,\mu W\,m^{-1}\,K^{-2}$, establishing Ga doping as an effective strategy for improving TE performance in ZnO-based materials.

Based on BTE calculations, the TE properties of SnTe monolayers have been explored under pnictogen and halogen doping [217]. Among the dopants considered, iodine (I) and arsenic (As) were identified as optimal for achieving high PF. Similarly, Mn-doped blue phosphorene has been reported to exhibit high zT along the zigzag direction at room temperature [299].

Youn *et al.* systematically studied the TE performance of n- and p-type doped $PtSe_2$ nanosheets through both experimental and theoretical approaches. Utilizing a molecular charge transfer doping method, they achieved PF values of 160 and 250 $\mu W\,m^{-1}\,K^{-2}$ for n- and p-type doping, respectively [300].

Experimental studies have demonstrated that Si substitution in graphene leads to reduced κ_l and a significant enhancement in TE conversion efficiency compared to both suspended and supported graphene [301]. The TE properties of porous graphene sheets have attracted considerable attention owing to their superior performance over pristine graphene, benefiting from bandgap opening and tunability through doping [302,303]. For instance, hydrogenated nitrogen-doped porous graphene exhibits a zT of 0.37 along the zigzag direction, while the armchair direction yields only $zT = 0.03$, owing to pronounced anisotropic transport behavior [302]. Similarly, boron doping in nitrogenated holey graphene increases zT from 0.4 to 0.62 at low boron concentrations [303]. Among γ-graphyne-like configurations, the S of the γ-graphyne-like BN sheet increases to 3.10×10^{-3} V/K, approximately five times higher than that of pristine γ-graphyne, leading to an extraordinary $zT \sim 6$ [304]. Furthermore, large-scale graphene doped with polyethylenimine and polyamic acid has been found to exhibit considerably high S and PF values, reaching 350 μV/K and 14 000 $\mu W m^{-1}\,K^{-2}$, respectively, when $\Delta T \simeq 18$ K [305].

The same doping strategies that enhance the TE efficiency of 2D materials can also be applied to NRs, leading to significant improvements in their TE performance [304,306–309]. For instance, nitrogen-doped zigzag GNRs exhibit higher zT than pristine counterparts because of enhanced S and reduced κ_l [308]. Additionally, magnetic Fe and Co impurities in GNRs have been shown to enable their use as spin-filter materials for heat-to-electricity conversion [309]. B- and N-doped graphyne benefit from a sizable bandgap, improving TE efficiency. A simultaneous increase in S and σ leads to a significant enhancement in zT, reaching values as high as ∼6 [304].

Table V presents a summary of electronic TE coefficient enhancements and reduced κ_l values achieved through gating and doping strategies.

VI. THE ROLE OF LATTICE THERMAL CONDUCTIVITY

One of the most viable routes for improving TE performance lies in engineering κ_l, preferably without degrading the electronic qualities [310–322]. Significant progress has been made in this direction, contributing to major advancements in the development of high-performance TE materials [323]. The study of phonon dynamics falls within the domain of non-equilibrium statistical physics. The macroscopic thermal transport properties of solids are typically described via microscopic interactions, using kinetic frameworks such as the Kadanoff–Baym [324,325] or Bloch–Boltzmann formalisms [326], or through linear response theory based on the Kubo formalism [327]. These methods are generally applied to near-equilibrium conditions and rely on the fluctuation-dissipation theorem [328]. Recent efforts have focused on

TABLE V. Enhanced TE coefficients of 2D materials through gating and doping.

2D-material	S_{enh}(p/n) (μV/K)	PF_{enh}(p/n) ($W\,m^{-1}K^{-2}$)	zT_{enh}(p/n)	κ_l ($W\,m^{-1}K^{-1}$)	T (K)
WS_2 [290]	300	$3.7 \times 10^{-3}\,W/K^2m$			300
Cu-doped MoS_2 [292]	202.8	31.3×10^{-6}			420
Nb-doped MoS_2 [293]	162	2.09×10^{-6}			300
GZO [294]	−/72	256.3×10^{-6}			623
$PtSe_2$ [300]	>150	$250/160 \times 10^{-6}$			
Zig-NH-G [302]	500	$0.78/\text{-} \times 10^{-15}\,W/K^2$	∼0.5	0.39 nW/K	300
Nitrogenated holey graphene [303]		$\sim 5 \times 10^{11}\,W/mK^2s$	0.62	53.4	300
Graphyne-like BN [304]	3100/3100		∼6	$30 \times 10^{-12}\,W/K$	300
Graphene [305]	∼350	14000×10^{-6}			$\Delta T = 18$

implementing the Kadanoff–Baym equations within first-principles frameworks, offering a potential path beyond the limitations of semiclassical approaches [329–331]. Nevertheless, current state-of-the-art first-principles calculations still predominantly employ the semiclassical Bloch–Boltzmann formalism via the BTE. An alternative and widely adopted approach for describing nanoscale thermal transport is the Landauer formalism, which is capable of modeling both ballistic and diffusive regimes. While the Landauer framework is often associated with non-interacting phonon transport, it can also incorporate scattering effects through an accurate determination of the phonon mean free path (see Sec. II).

Recent advances in first-principles solutions of the phonon BTE have significantly enhanced our understanding of thermal transport phenomena in materials. Moving beyond the relaxation time approximation, it is now feasible to iteratively solve the BTE using third- and fourth-order force constants for a wide range of material classes [332–334]. Notably, the integration of machine learning-based techniques has enabled the achievement of convergence in calculations involving higher-order anharmonic interactions, particularly for fourth-order terms [335,336]. Furthermore, modern computational frameworks facilitate the inclusion of additional scattering mechanisms, such as isotope and boundary scattering, alongside various phonon-phonon interaction processes [332–334].

As mentioned, thermal transport in semiconductors is primarily governed by phonon transport, with phonon-phonon scattering—arising from the anharmonicity of the interatomic potential—playing the dominant role. While the coupling of phonons with electrons or quasiparticles such as magnons can influence thermal transport, these effects are typically negligible compared to the phonon contribution. However, recent studies have shown that e–ph coupling may significantly reduce κ_l in highly doped semiconductors, including several high-performance the TE materials [337–343]. In particular, the occupation of sharply localized electronic states—such as van Hove singularities in doped single-layer crystals—has been reported to reduce κ_l by up to 80% while concurrently enhancing the κ_e [344–350]. Therefore, depending on the doping level and the presence of sharply localized states near the Fermi level, the impact of *e*–ph coupling on κ_l should be carefully considered in simulations to obtain reliable estimates of the material's TE performance.

In addition to carrier-based approaches, MD-based techniques for calculating lattice thermal conductivity, such as the Green-Kubo method and non-equilibrium MD are also widely employed [351,352]. These methods enable direct atomistic simulations of heat transport, offering valuable insights into phonon dynamics and TC in a variety of material systems. While MD approaches provide a complementary perspective to the semiclassical and quantum mechanical formalisms discussed earlier, they are subject to certain limitations, including high computational cost and challenges in accurately capturing phonon-phonon scattering processes, particularly at low temperatures. Nonetheless, MD simulations remain powerful tools for exploring thermal transport phenomena, especially in complex or disordered materials where first-principles approaches may be less useful.

Moreover, recent advancements in machine learning-based interatomic potentials have opened new avenues for accurately describing phonon-phonon interactions [353,354]. These potentials employ data-driven techniques to capture complex interatomic forces, thereby enhancing the predictive capabilities of thermal transport models. When integrated with MD simulations, machine learning approaches enable more accurate and computationally efficient investigations of phonon dynamics and κ_l across a wide range of material systems. Furthermore, the recent implementation of *ab initio* Green-Kubo theory has allowed for the direct computation of TC in insulating materials from first principles [355,356], offering a more comprehensive understanding of thermal transport phenomena at the atomic scale.

Indeed, recent advancements in computational tools, extensively documented in the literature, offer a diverse array of methodologies for accurately determining lattice thermal transport properties across a broad spectrum of materials [332–335,357,358]. These approaches are applicable to strained, defected, heterostructured, and doped systems, illustrating their versatility in addressing complex material configurations. As a result, computational characterization of strategies for tailoring TC has emerged as a powerful and reliable avenue for advancing TE research. This approach has already shown significant potential in achieving targeted TE performance across various candidate materials. Furthermore, it has been demonstrated that nanostructuring and alloying strategies—guided by computational predictions—can effectively suppress κ while maintaining high σ, thereby leading to notable improvements in the zT. These findings underscore the transformative role of computational

methodologies in accelerating the discovery and design of high-performance TE materials.

A. Materials with intrinsically low lattice thermal conductivity

The dominant mechanism in the heat transfer process of TE materials is κ_l, as discussed above. In this context, the primary heat carriers are phonons, and the main resistive mechanism is phonon-phonon scattering, whose rate is directly determined by the degree of anharmonicity in the interatomic potential of the crystal. Consequently, the intrinsic anharmonic nature of TE materials plays a pivotal role in governing their efficiency [359]. Phonon-phonon interactions in solids can be categorized into three-phonon, four-phonon, and even higher-order scattering processes. The rates of these scattering events are governed by the third-, fourth-, and higher-order force constants, which are, in turn, dictated by the crystal symmetry and the nature of chemical bonding in the material—assuming an ideal crystalline structure. Recent studies have demonstrated that explicitly accounting for four-phonon interactions in the thermal transport calculations of 2D materials leads to a significant reduction in κ_l [360–363]. TE materials with intrinsically high anharmonicity have garnered substantial attention, as understanding the interplay between chemical bonding and lattice vibrations is critical for modulating phonon transport. Materials that exhibit phonon-glass electron-crystal behavior, achieving TC values close to the amorphous limit, have demonstrated high-zT values. This has spurred extensive research into identifying and designing materials that intrinsically possess ultralow κ_l, comparable to that of amorphous solids [318,364–373].

On the other hand, weak and anisotropic bonding characteristics have been identified as effective mechanisms for suppressing TC in layered crystals that intrinsically exhibit favorable TE properties. Notable successes have been reported for materials such as BiCuSeO [374], SnSe [367], Bi_2Te_3 [375], and $Cr_2Ge_2Te_6$ [376], all of which demonstrate low κ_l owing to their intrinsically weak interlayer bonding. The theoretical foundation for this concept was laid by Hicks and Dresselhaus in 1992, who predicted that reduced dimensionality and bonding asymmetry would lead to significant suppression of κ_l [2]. This hypothesis was experimentally validated years later with the successful fabrication of Si nanowires, which exhibited remarkably low κ_l values in agreement with theoretical predictions [377].

The successful synthesis of single- to few-layer 2D materials has opened new avenues for TE research. In addition to their unique electronic properties, the thermal transport characteristics of these materials have been extensively investigated. Notably, the effect of dimensional reduction has been shown to enable effective control over lattice thermal properties. This phenomenon has been particularly well demonstrated in graphene, boron nitride, phosphorene, and TMDs, where reduced dimensionality leads to enhanced phonon scattering and significantly lower κ_l values.

Initially, graphene and its 1D ribbon forms have been intensively investigated as potential TE materials, despite their remarkably high κ_l [378]. The exceptional electronic transport properties of graphene have inspired significant interest in its TE applications. However, the theoretically predicted superior TE performance of graphene has not been experimentally validated. Consequently, research efforts have shifted toward TMD layers, which have been predicted to exhibit high carrier mobility and relatively low κ_l [379]. First-principles calculations have reported room-temperature κ_l values of 142, 103, and 54 $Wm^{-1}K^{-1}$ for WS_2, MoS_2, and $MoSe_2$, respectively [380]. Supporting these findings, other theoretical studies have predicted κ_l values in the range of 30–115 $Wm^{-1}K^{-1}$ for MX_2 compounds (M = Mo, W; X = S, Se, Te) [381]. Although these predictions have not been precisely confirmed by experiments, they remain consistent with available measurements [382,383].

The advances in the synthesis of 2D materials have paved the way for the theoretical exploration of numerous possible layered systems [384]. Consequently, many of these have been identified as promising TE candidates. In particular, materials exhibiting low room-temperature κ_l on the order of a few $Wm^{-1}K^{-1}$, such as phosphorene oxide [385], GeX (X = S, Se, Te) [386], XSe (X = Cu, Ag, Au) [387], AB_2Te_4 (A = Sn, Pb; B = Sb, Bi) [121], ISbTe [388], Sb_2C [389], $GeAs_2$ [390], GeSe [391], MNI (M = Zr, Hf) [392], Bi_2X_2Y (X = Se, Te; Y = S, Se, Te) [393], Al_2Te_5 monolayers [394], and BiP_3 [395], have been demonstrated as efficient thermoelectrics under various temperature and carrier concentration regimes relevant to potential technological applications. On the other hand, single-layer materials with intrinsically ultra-low κ_l values ($< 1\,Wm^{-1}K^{-1}$), such as holey phosphorene [396], $CdTe_2$ [397], AuS [398], α-$InSe_3$ [399], $Sc_2I_2Se_2$ [400], $Al_2I_2Se_2$ [401], $MoP_2Ga_2S_2$ [402], SnI_2 [403], $MnBi_2Te_4$ [404], Ge_2Sb_2 [405], Pb_2XY (X = S, Se; Y = Se, Te; $X \neq Y$) [406], Janus β-PdXY (X/Y = S, Se, Te) [407], and other 2D Bi-based compounds [408,409], have been predicted through theoretical materials discovery efforts. Additionally, W-Janus bilayers have been reported to exhibit exceptionally low κ_l because of hybridization between acoustic and low-frequency optical phonon modes [410]. Similarly, a substantial suppression of κ_l has been observed in 2D CrSX (X = Cl, Br, I) [411], SiS [412], WB_4 [413], and the $Ca_3Sn_2S_7$ chalcogenide perovskite monolayer [414], which is attributed to the presence of rattling phonon modes.

B. Strategies for reducing lattice thermal conductivity

In addition to intrinsic phonon-phonon scattering, the phonon mean free paths in crystalline solids can be effectively tuned through various extrinsic scattering mechanisms. Traditionally, these mechanisms are categorized into three main approaches: (i) structural disorder or distortion of unit cells, such as point defects and isotope substitutions; (ii) resonant scattering induced by localized rattling atoms, as observed in compounds like $CsBi_4Te_6$; and (iii) the introduction of a high density of interfaces through nanostructuring or grain-boundary engineering. These strategies have proven to be effective in suppressing lattice thermal transport and are widely employed to enhance the TE efficiency of materials.

1. Strain engineering

It has been demonstrated that strain can serve as an effective tuning parameter for manipulating the lattice thermal transport properties of 2D materials, in addition to their

optical and electronic characteristics [415]. Beyond theoretical predictions, the applicability of strain engineering—particularly tensile strain—has been experimentally validated through two-point and four-point bending techniques [416]. However, enhancing TE efficiency requires a controllable suppression of κ_l. Studies on graphene have revealed that whether tensile strain increases or decreases κ_l depends sensitively on the sample geometry and length [417–420].

Recent works have highlighted the effectiveness of this strategy across various 2D systems. For instance, the κ_l of γ-Ge_2SSe has been reduced from 4.41 to 3.13 $Wm^{-1}K^{-1}$ under biaxial tensile strain [421], while La_2GeI_2 monolayer exhibited a significant decrease in κ_l from 3.22 to 0.57 $Wm^{-1}K^{-1}$ upon strain engineering [233]. Vani *et al.* have shown that hydrogenated silicene exhibits ultralow κ_l under 14% tensile strain [234]. Moreover, experimental findings demonstrate that the TC of monolayer MoS_2 decreases by approximately 62% under 6.3% tensile strain [422]. For other planar and few-layered materials—such as BN, MoS_2, SiC, arsenene, stanene, silicene, GaN, and BAs—a similar nonmonotonic strain dependence has been predicted [221,417–419,423–430]. On the other hand, a weak dependence of κ_l on in-plane compressive strain has been observed in several 2D materials, indicating a directional sensitivity in the thermal response to strain.

As with in-plane strain, out-of-plane strain also has a notable influence on the lattice thermal transport properties of few-layer 2D materials, as demonstrated in bilayer graphene [431,432]. However, similar to the in-plane case, the variation in κ_l under out-of-plane strain exhibits nonmonotonic behavior, strongly dependent on the size and geometry of the system. Hence, the current literature suggests that strain engineering, while promising in specific cases, may not serve as a universally reliable strategy for consistently enhancing TE performance. Instead, it appears to function more as a stochastic tuning parameter, with outcomes highly sensitive to material-specific and structural conditions.

2. Intentional defects and disorder

Another strategy to reduce κ_l in 2D materials is through the intentional introduction of defects and disorder. These structural imperfections are particularly effective at scattering long-wavelength phonons, which are the primary heat carriers in crystalline solids. Various defect types—such as point defects, line defects, and surface defects—commonly observed in bulk crystals are also present in 2D materials [415]. Even at minor concentrations, such defects can significantly suppress κ_l [433–436]. Atomistic defects, including vacancies, substitutions, and interstitials, primarily influence phonon-specific heat capacity and group velocity. Nonetheless, the dominant mechanism contributing to TC suppression is the reduction in the phonon mean free path [436,437]. This phenomenon has been observed in graphene [438], BN [439], and TMD layers [434–436], where the presence of defects—particularly those randomly distributed—has been shown to strongly suppress κ_l.

The large-scale formation of atomistic defects can give rise to nanomesh structures. Both disordered and ordered meshes in 2D materials have been demonstrated to effectively suppress κ_l [440–442]. First-principles and atomistic simulations on graphene nanomeshes have shown that phonon backscattering and localization around nanopores significantly hinder heat transport. Moreover, a weak temperature dependence of TC has been predicted, which suggests the possibility of achieving a stable TE response over a broad temperature range. Experimentally, the utility of nanoporous structures for tailoring lattice thermal transport has been validated in 2D phononic crystals [443].

Because of the 2D orientation of in-plane atoms, grain boundary-type imperfections are commonly observed in these materials [444–446]. These imperfections suppress κ_l by increasing phonon scattering rates and introducing boundary scattering as an additional resistive mechanism. Numerous studies have demonstrated that TC in 2D materials decreases with grain formation, with smaller grain sizes yielding more pronounced suppression [447–452]. Conversely, it has been reported that oriented grain boundaries can lead to considerable anisotropy in κ_l [453].

Similar to intentional atomic defect creation, grain boundary engineering can be considered an effective strategy for reducing κ_l in potential TE materials, including 2D systems [454]. However, the experimental realization of controllable grain boundaries remains considerably more challenging. Notably, graphene structures with controlled grain formations have been experimentally synthesized by Ma *et al.* [449].

3. Heterostructuring

As another strategy for thermal transport engineering in TE materials, the concept of heterojunctions has been proposed [455]. The influence of heterostructures on TC has been extensively investigated using both first-principles and classical approaches, considering both in-plane and out-of-plane 2D heterostructures, such as graphene/h-BN, graphene/silicene, and $MoSe_2/WSe_2$ [151,153,456–459]. In most cases, the resulting κ_l lies within the range defined by the individual components of the heterostructure. Moreover, for asymmetric heterostructures, direction-dependent TC—referred to as thermal rectification—has been predicted, particularly in graphene/h-BN and $MoSe_2/WSe_2$ lateral heterojunctions [458–460], offering an additional route for thermal transport manipulation. These findings, along with the successful synthesis of various 2D heterostructures [461,462], highlight the potential of heterostructuring as a powerful method to regulate κ_l in TE materials.

4. Doping and alloying

Similar to its effect in charge transport and in bulk materials, doping has been shown to be an effective strategy for engineering κ_l in 2D systems [415]. In principle, doping introduces mass mismatch and bond strength disorder, which enhances phonon scattering [463,464]. Moreover, enhanced e–ph coupling has been demonstrated to significantly suppress lattice thermal transport in doped 2D materials, such as hexagonal boron phosphorus [345]. A similar mechanism is also present in alloyed 2D monolayers, where compositional disorder effectively reduces phonon transport. The strong influence of such structural and mass disorders on thermal transport has been reported in several studies, including N-doped graphene

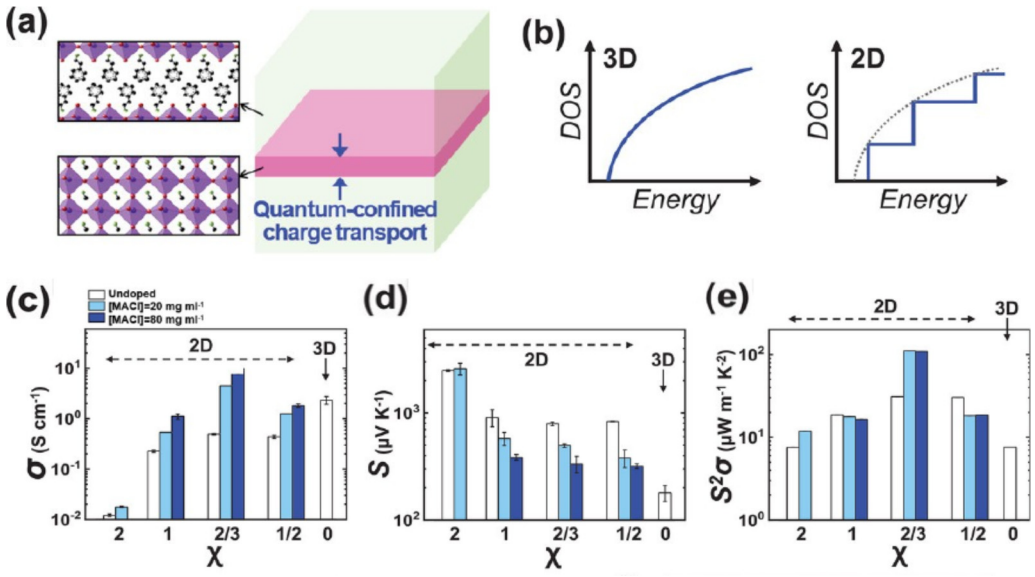


FIG. 7. 2D OHPs. Quantum-confined charge transport by the organic spacer layer (a), and electronic DOS (b) of 3D and 2D semiconductors are illustrated. Electrical conductivity (c), Seebeck coefficient (d), and power factor (e), with respect to the ratio of phenethylammonium iodide to tin(II) iodide, $\chi = [\text{PEAI}]/[\text{SnI}_2]$ are also shown. (Reproduced with permission from Ref. [490].)

[465], fullerene-doped graphene [466], CH_3-doped BN sheets [467], W-doped $MoSe_2$ [468], Si_xGe_y monolayers [469], and GaSb-InSb alloys [470].

In addition to chemical doping, isotope engineering also serves as an effective technique to reduce κ_l through mass disorder without altering the structural or chemical integrity of the host material. The dramatic impact of low-concentration isotope disorder on κ_l has been demonstrated both theoretically and experimentally in graphene [471–475]. These findings underscore the potential of isotope doping as a clean and tunable method for modulating thermal transport in 2D materials.

VII. EMERGING MATERIALS FOR EFFICIENT TE APPLICATIONS

In this section, we review emerging materials with outstanding TE properties and summarize the key mechanisms that contribute to their enhanced performance.

Twisted 2D materials. Twisted bilayers of 2D materials can exhibit ultraflat bands in their low-energy spectra, resulting in strong electron correlations [476–481]. These flat bands have been explored not only to exploit resonances near the Fermi level but also to investigate the applicability of the Mott approach in such correlated systems. In magic-angle twisted bilayer graphene, simultaneous measurements of resistivity and thermopower have revealed an excess S of $2\,\mu\text{V/K}$ at 10 K, which has been interpreted as evidence of non-Fermi liquid behavior [482]. Similarly, in bilayer graphene systems exhibiting trigonal warping and a Lifshitz transition, it has been shown that S cannot be inferred solely from conductance measurements [483]. Twist-angle-dependent enhancements in S have also been reported in cross-plane measurements of bilayer and trilayer graphene [484–488]. In particular, graphene/boron nitride twisted heterostructures exhibit pronounced variations in PF and zT as a function of rotation angle. The κ_l of 0.095 W/mK at 300 K has been reported at a rotation angle of 21.79° [489].

Perovskites. Perovskites have garnered significant attention because of their potential in photovoltaic applications. Many perovskite materials are low-cost and flexible, rendering them attractive for various energy conversion technologies. Additionally, their intrinsically soft lattice structures contribute to low κ_l [491]. Organometallic halide perovskites (OHPs), in particular, exhibit excellent charge transport properties, positioning them as promising candidates for TE applications. Notably, their 2D counterparts have demonstrated PF that are an order of magnitude higher than those of their 3D analogs, as illustrated in Fig. 7 [490]. Furthermore, it has been shown that Sn-based halide perovskites can be stabilized in 2D form through the incorporation of conjugated ligands, resulting in significantly enhanced PF [492].

MOFs and COFs. COFs are porous crystalline materials composed entirely of light elements linked by covalent bonds, whereas MOFs are hybrid porous materials formed by the coordination of metal ions with organic ligands. The unique structural and electronic characteristics of MOFs and COFs have attracted considerable interest for TE applications.

He *et al.* have reported that zT of crystalline 2D MOFs, $[M_3(\text{HITP})_2]$ (M = Ni, Pd, or Pt), can attain high values under optimized mean free paths and with p-type doping [493]. The combination of a large S and low κ contributes significantly to their enhanced TE performance. Furthermore, Cu-HHTP-rGO has been shown to exhibit a PF of $0.17\ \mu\text{W/mK}^2$, which is notably high relative to previously reported MOF-based systems. The intrinsically low κ of Cu-HHTP-rGO is expected to further boost its zT when coupled with its high PF [494].

Several other 2D MOFs, including $Ni_3(\text{HITP})_2$, $Cu_3(\text{HHTP})_2$, Cu-BHT, SWCNT@Ni-THT, and $\text{TCNQ@Cu}_3(\text{BTC})_2$ composite films, as well as nanorods of MOFs based on perthiolated coronene (PTC), have been identified as promising TE materials because of

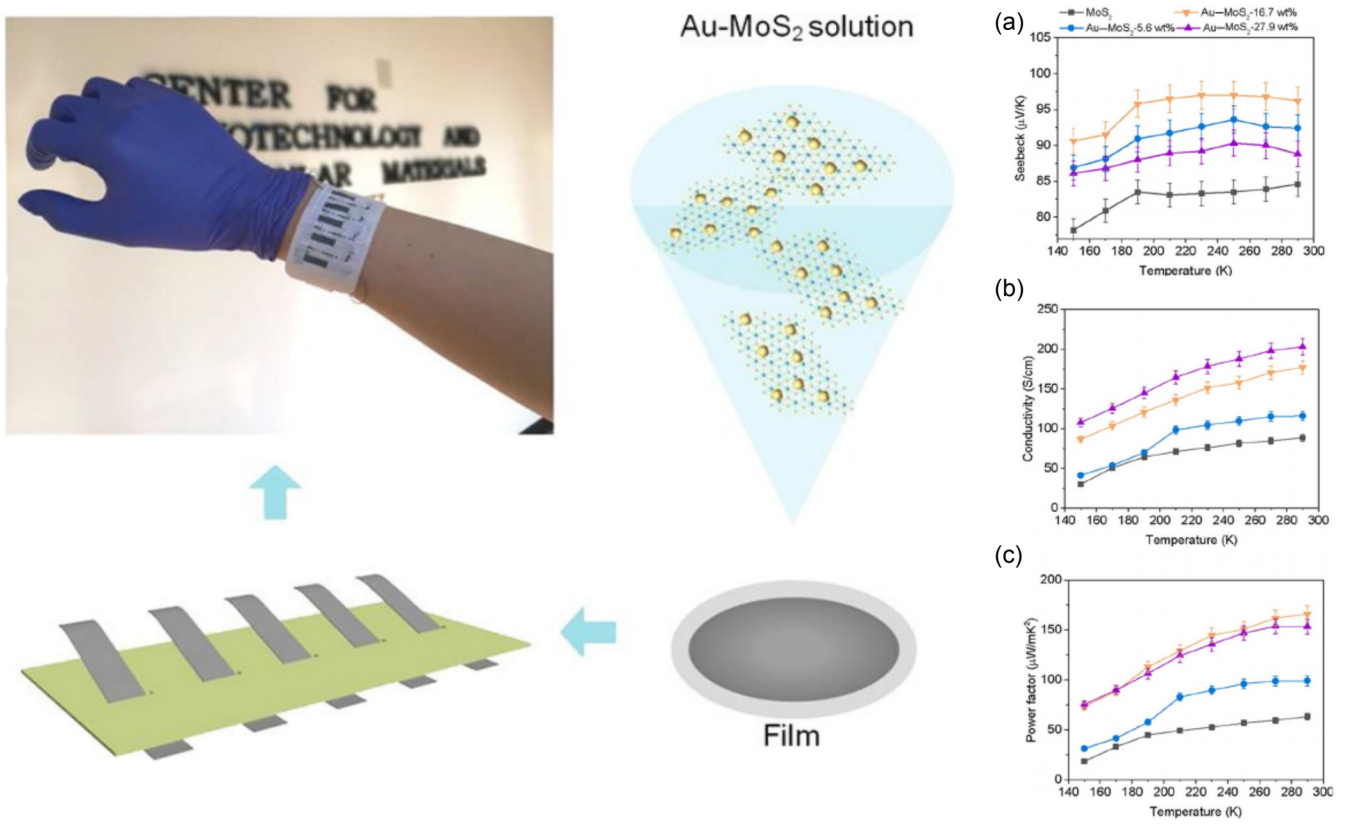


FIG. 8. An illustration of experimental route for obtaining Au-decorated MoS2-assembled heterojunction systems, which is promising for harvesting human body heat (left). TE coefficients of flexible thin films based on 2D MoS_2 and Au–MoS_2 hybrid nanocomposites are plotted on the right. Seebeck coefficient (a), electrical conductivity (b), and the power factor (c) are plotted as functions of temperature. (Reproduced with permission from Ref. [508].

their intrinsically low κ_l and PF [495–500]. A recent high-throughput computational study, which employed classical MD simulations, has identified more than 30 MOFs with ultralow κ, marking them as excellent candidates for TE applications [501]. Furthermore, fluorene-based COFs have been reported to exhibit high S and PF at 300 K, positioning them as strong contenders for energy conversion technologies [502]. Very recently, Zhou *et al.* have shown that even a small contribution from the linker and knot components in 2D COFs can significantly enhance hole mobility, thereby increasing the PF [503].

Flexible 2D TE devices. The integration of lightweight and flexible 2D materials into wearable electronic devices presents a promising strategy for harvesting temperature gradients between the human body and the ambient environment to generate TE power. Wearable electronics are increasingly employed for physiological monitoring, health tracking, and smart textiles, thereby requiring materials that combine high PF, low κ_l, and mechanical flexibility [11,504–506].

Among emerging 2D materials, $NbSe_2/WSe_2$ heterostructures have been developed for wearable gas sensing applications [507], while Au-decorated 2D MoS_2 nanostructures, as illustrated in Fig. 8, have demonstrated significant potential for flexible TE applications [508]. Bi_2Te_3 thin films remain among the most efficient TE materials for wearable technologies [509,510], and α-phase Cu_2Se thin films have also exhibited promising flexibility and TE performance [509]. Nonoxidized graphene flakes (NOGF) preserve high electrical conductivity and mechanical stability, making them suitable for integration into flexible TE devices [511,512]. Similarly, MXene nanosheet/organic superlattice (SL) composites offer a synergistic enhancement in TE performance, benefiting from high carrier mobility and low κ_l [513]. Furthermore, 2D tellurene has emerged as a promising candidate owing to its exceptional flexibility and high TE efficiency [514]. The combination of low κ, high PF, and mechanical durability in these materials underscores their potential for next-generation wearable TE devices.

VIII. SUMMARY AND CONCLUDING REMARKS

2D materials offer a broad platform for engineering approaches aimed at enhancing TE efficiency. Because of their versatility and tunability, 2D TE materials can be envisioned as integrated components in next-generation devices based on vdW heterostructures. In this review, we have examined key physical phenomena and engineering strategies that govern TE performance in 2D systems, emphasizing approaches proposed for achieving high efficiency. Among these, the quantum confinement effect has been a foundational strategy, extensively studied even prior to the emergence of atomically thin materials. As discussed in Sec. III, quantum confinement not only enhances the PF but also contributes to the suppression of κ_l, thereby boosting the overall performance.

Beyond quantum confinement, 2D materials exhibit a range of unique features that can be leveraged to further enhance TE performance. Notably, certain classes of 2D materials derive a significant advantage from their unconventional band structures, making them particularly promising for TE applications. Materials with quartic MHS, octic (ring-shaped), and pudding-mold-type band dispersions stand out in this regard (see Sec. IV A). These band structures are characterized by singularities near the band edges, which contribute to enhanced DOS and result in high PFs. As in 3D TE materials, valley and band degeneracies play a pivotal role in determining TE efficiency. In 2D systems, however, these degeneracies can be more readily manipulated, particularly via strain engineering, enabling simultaneous enhancements in S and the PF. The underlying mechanisms and examples of such strategies are discussed in Secs. IV B and V B. Moreover, the high surface-to-volume ratio inherent to 2D materials facilitates efficient chemical functionalization and nanostructuring, both of which can drastically modulate their electronic and phononic properties (see Secs. V A and V C). Gating is another powerful approach in 2D systems, allowing precise control over carrier concentration and Fermi level positioning (Sec. V E). Additionally, doping and the intentional introduction of defects have been extensively employed to enhance TE performance, as detailed in Secs. V E and V D. Crucially, strategies such as strain engineering, defect creation, heterostructuring, doping, and alloying have proven effective in reducing TC, a key parameter for achieving high zT, as reviewed in Sec. VI. The discovery of new material systems (as reviewed in Sec. VII) and the development of innovative engineering strategies are anticipated to further advance the field.

Some critical remarks are in order here. Current literature on the TE properties of 2D materials is predominantly composed of theoretical and modeling studies, while experimental investigations remain comparatively limited. Even for fundamental quantities such as TC, experimental reports are relatively scarce. In bulk thermoelectric materials, theoretical approaches generally reproduce qualitative experimental trends, including the Seebeck coefficient, carrier polarity, and their temperature and doping dependence; however, quantitative agreement is often limited, and calculations tend to overestimate the thermoelectric figure of merit zT [515,516]. A central source of this discrepancy lies in the treatment of carrier scattering, as the commonly adopted constant relaxation time approximation neglects material-dependent and doping-dependent scattering processes; correspondingly, improved agreement is obtained when relaxation times extracted from experiment are employed [517,518]. Experimentally measured zT values are further reduced by extrinsic scattering mechanisms, including impurity, defect, and microstructural scattering, effects that are especially pronounced in heavily doped systems, materials near phase stability boundaries, and compounds with strong electronic correlations [519,520]. Consequently, while theory provides robust insight into transport mechanisms and serves as an effective screening tool, quantitative prediction of bulk thermoelectric performance generally requires close integration of computational modeling with experimental input [516,519]. These limitations carry over to two-dimensional thermoelectric systems, where enhanced boundary scattering, substrate coupling, and increased sensitivity to disorder are likely to further complicate quantitative comparison between theoretical predictions and experimental measurements.

The discrepancy between simulations and experiments is further amplified by experimental difficulties in obtaining precise thermoelectric measurements in atomically thin systems. Some strategies identified as promising in theoretical studies require further analysis. Nanostructuring, while capable of tailoring material properties, carries the risk of introducing disorder that may degrade transport and TE efficiency. Similar concerns apply to edge/surface functionalization, intentional defects, and vacancies. Although these strategies are predicted to be effective when implemented periodically, they may also act as sources of disorder, reducing the performance. Clarifying these competing effects remains an important open task. At present, the literature provides extensive insights into the intrinsic thermoelectric (TE) properties of 2D materials. Factors such as substrates, protective layers, and interfaces/contacts will play decisive roles in actual device performance. The influence of these external effects, whether beneficial or detrimental, needs to be systematically investigated. This is essential not only for advancing device-level applications but also for bringing theory and experiment into closer alignment.

In summary, the intense interest in 2D TE materials is expected to continue in the coming years, supported by ongoing advances in computational methods that promise increasingly accurate predictions of TE behavior. Experimental studies will further enrich this understanding, with progress in characterization techniques playing a key role in confirming theoretical insights and guiding practical applications. Overall, the study of TE transport in 2D materials is advancing rapidly, driven by both theory and experiment, and offers a fertile ground for innovative approaches and breakthroughs.

ACKNOWLEDGMENTS

H.S. acknowledges the support from TÜBİTAK (Grant No. 124F332). G.Ö.S. acknowledges support from TÜBİTAK BİDEB 2218 program (Grant No. 123C159). E.D. acknowledges the financial support of Turkish Academy of Sciences (TÜBA).

[1] L. Yang, Z.-G. Chen, M. S. Dargusch, and J. Zou, Adv. Energy Mater. **8**, 1701797 (2018).

[2] L. D. Hicks and M. S. Dresselhaus, Phys. Rev. B **47**, 12727 (1993).

[3] L. D. Hicks and M. S. Dresselhaus, Phys. Rev. B **47**, 16631 (1993).

[4] Y. Li, T. Ding, D. K. Sang, M. Wu, J. Li, C. Wang, F. Liu, H. Zhang, and H. Xie, J. Mater. Chem. C **8**, 4181 (2020).

[5] Anisha, M. Singh, R. Kumar, S. Srivastava, and K. Tankeshwar, J. Phys. Chem. Solids **172**, 111083 (2023).
[6] H. K. Ng, D. Chi, and K. Hippalgaonkar, J. Appl. Phys. **121**, 204303 (2017).
[7] N. T. Hung, E. H. Hasdeo, A. R. T. Nugraha, M. S. Dresselhaus, and R. Saito, Phys. Rev. Lett. **117**, 036602 (2016).
[8] J. Zeng, X. He, S.-J. Liang, E. Liu, Y. Sun, C. Pan, Y. Wang, T. Cao, X. Liu, C. Wang, *et al.*, Nano Lett. **18**, 7538 (2018).
[9] Y. Zhao, P. Yu, G. Zhang, M. Sun, D. Chi, K. Hippalgaonkar, J. T. L. Thong, and J. Wu, Adv. Funct. Mater. **30**, 2004896 (2020).
[10] N. T. Hung, A. R. T. Nugraha, T. Yang, and R. Saito, MRS Adv. **5**, 469 (2020).
[11] K. Kanahashi, J. Pu, and T. Takenobu, Adv. Energy Mater. **10**, 1902842 (2020).
[12] G. Zhang and Y.-W. Zhang, J. Mater. Chem. C **5**, 7684 (2017).
[13] M. Fronzi, P. Mele, A. V. Ellis, and C. Stampfl, RSC Appl. Interfaces **2**, 852 (2025).
[14] H. Ming, Z.-Z. Luo, Z. Zou, and M. G. Kanatzidis, Chem. Rev. **125**, 3932 (2025).
[15] D. Li, Y. Gong, Y. Chen, J. Lin, Q. Khan, Y. Zhang, Y. Li, H. Zhang, and H. Xie, Nano-Micro Lett. **12**, 36 (2020).
[16] M. Martin-Gonzalez, K. Lohani, and N. Neophytou, Energy Mater. **5**, 500121 (2025).
[17] R. Landauer, Philos. Mag. **21**, 863 (1970).
[18] M. S. Lundstrom and C. Jeong, *Near-Equilibrium Transport: Fundamentals And Applications* (World Scientific, Singapore, 2012).
[19] Y. Kruglyak, J. Nanosci. **2014**, 7254201 (2014).
[20] C. Jeong, R. Kim, M. Luisier, S. Datta, and M. Lundstrom, J. Appl. Phys. **107**, 023707 (2010).
[21] R. Landauer, IBM J. Res. Dev. **1**, 223 (1957).
[22] M. Dresselhaus, Y.-M. Lin, S. Cronin, O. Rabin, M. Black, G. Dresselhaus, and T. Koga, in *Recent Trends in Thermoelectric Materials Research III*, Semiconductors and Semimetals, edited by T. M. Tritt (Elsevier, Amsterdam, 2001), Vol. 71, pp. 1–121.
[23] G. Chen, M. S. Dresselhaus, G. Dresselhaus, J.-P. Fleurial, and T. Caillat, Int. Mater. Rev. **48**, 45 (2003).
[24] J. M. Ziman, *Electrons and Phonons: The Theory of Transport Phenomena in Solids* (Oxford University Press, New York, 1960).
[25] N. W. Ashcroft and N. D. Mermin, *Solid State Physics* (Saunders College Publishing, Fort Worth, 1976).
[26] G. D. Mahan and J. O. Sofo, Proc. Natl. Acad. Sci. USA **93**, 7436 (1996).
[27] L. G. C. Rego and G. Kirczenow, Phys. Rev. Lett. **81**, 232 (1998).
[28] A. Ozpineci and S. Ciraci, Phys. Rev. B **63**, 125415 (2001).
[29] T. Yamamoto, S. Watanabe, and K. Watanabe, Phys. Rev. Lett. **92**, 075502 (2004).
[30] R. E. Peierls, *Quantum Theory of Solids* (Clarendon Press, Oxford, 1955).
[31] A. Ward, D. A. Broido, D. A. Stewart, and G. Deinzer, Phys. Rev. B **80**, 125203 (2009).
[32] A. Kundu, N. Mingo, D. A. Broido, and D. A. Stewart, Phys. Rev. B **84**, 125426 (2011).
[33] M. S. Dresselhaus, G. Dresselhaus, X. Sun, Z. Zhang, S. B. Cronin, and T. Koga, Phys. Solid State, **41**, 679 (1999).
[34] M.-J. Lee, J.-H. Ahn, J. H. Sung, H. Heo, S. G. Jeon, W. Lee, J. Y. Song, K.-H. Hong, B. Choi, S.-H. Lee, and M.-H. Jo, Nat. Commun. **7**, 12011 (2016).
[35] J. O. Sofo and G. D. Mahan, Appl. Phys. Lett. **65**, 2690 (1994).
[36] N. T. Hung, A. R. T. Nugraha, E. H. Hasdeo, M. S. Dresselhaus, and R. Saito, Phys. Rev. B **92**, 165426 (2015).
[37] B. Dong, Z. Wang, N. T. Hung, A. R. Oganov, T. Yang, R. Saito, and Z. Zhang, Phys. Rev. Mater. **3**, 013405 (2019).
[38] V. Chen, H. R. Lee, C. Koroglu, C. J. McClellan, A. Daus, and E. Pop, Nano Lett. **23**, 4095 (2023).
[39] Z. Dong, S. Xiao, M. Zhang, W. Yan, Y. Li, X. Chen, and X. Wang, ACS Appl. Electron. Mater. **7**, 729 (2025).
[40] X. Jiang, C. Xu, and D. Wang, ACS Appl. Nano Mater. **7**, 16404 (2024).
[41] N. T. Hung, A. R. T. Nugraha, and R. Saito, Appl. Phys. Lett. **111**, 092107 (2017).
[42] Y. Zhang, B. Feng, H. Hayashi, C.-P. Chang, Y.-M. Sheu, I. Tanaka, Y. Ikuhara, and H. Ohta, Nat. Commun. **9**, 2224 (2018).
[43] H. Ohta, S. W. Kim, S. Kaneki, A. Yamamoto, and T. Hashizume, Adv. Sci. **5**, 1700696 (2018).
[44] C. Wu, L. Sun, and J. Han, Phys. Chem. Chem. Phys., **25** 28735 (2023).
[45] M. Mandal, N. Maity, P. K. Barman, R. Biswas, S. Mondal, V. Raghunathan, A. K. Singh, P. K. Nayak, and K. Sethupathi, Phys. Rev. B **110**, 195404 (2024).
[46] G. Benenti, G. Casati, K. Saito, and R. Whitney, Phys. Rep. **694**, 1 (2017).
[47] N. T. Hung and R. Saito, Adv. Quantum Technol. **4**, 2000115 (2021).
[48] J. Mao, Z. Liu, and Z. Ren, npj Quant. Mater. **1**, 16028 (2016).
[49] M. Samanta, T. Ghosh, S. Chandra, and K. Biswas, J. Mater. Chem. A **8**, 12226 (2020).
[50] J. Zhou, R. Yang, G. Chen, and M. S. Dresselhaus, Phys. Rev. Lett. **107**, 226601 (2011).
[51] J. de Boor, J. Materiomics **7**, 603 (2021).
[52] H. Naithani and T. Dasgupta, ACS Appl. Energy Mater. **3**, 2200 (2020).
[53] J. Zhu, X. Zhang, M. Guo, J. Li, J. Hu, S. Cai, W. Cai, Y. Zhang, and J. Sui, npj Comput. Mater. **7**, 116 (2021).
[54] J. Maassen, Phys. Rev. B **104**, 184301 (2021).
[55] C. Rudderham and J. Maassen, Phys. Rev. B **103**, 165406 (2021).
[56] P. Graziosi, Z. Li, and N. Neophytou, Appl. Phys. Lett. **120**, 072102 (2022).
[57] R. S. Whitney, Phys. Rev. Lett. **112**, 130601 (2014).
[58] C. Jeong, R. Kim, and M. S. Lundstrom, J. Appl. Phys. **111**, 113707 (2012).
[59] J. Park, Y. Xia, V. Ozoliņš, and A. Jain, npj Comput. Mater. **7**, 43 (2021).
[60] M. N. Çınar and H. Sevinçli, Phys. Rev. Appl. **14**, 024075 (2020).
[61] P. Graziosi and N. Neophytou, J. Phys. Chem. C **124**, 18462 (2020).
[62] S. E. A. Akhtar and N. Neophytou, ACS Appl. Energy Mater. **8**, 1609 (2025).
[63] P. Graziosi, K.-I. Mehnert, R. Dutt, J.-W. G. Bos, and N. Neophytou, PRX Energy **3**, 043009 (2024).
[64] A. Kommini and Z. Aksamija, J. Phys. Mater. **3**, 015005 (2019).

[65] H. Sevinçli, Nano Lett. **17**, 2589 (2017).
[66] M. N. Cinar, G. Ozbal Sargin, K. Sevim, B. Özdamar, G. Kurt, and H. Sevincli, Phys. Rev. B **103**, 165422 (2021).
[67] S. Zhang, C. Li, J. Shang, H. Li, Z. Wang, L. Li, and Y. Jia, Phys. Chem. Chem. Phys. **22**, 21961 (2020).
[68] W. Li, X. Zhang, J. Yang, S. Zhou, C. Song, P. Cheng, Y.-Q. Zhang, B. Feng, Z. Wang, Y. Lu, K. Wu, and L. Chen, Nat. Commun. **14**, 2757 (2023).
[69] N. Jia, Y. Shi, Z. Lv, J. Qin, J. Cai, X. Jiang, J. Zhao, and Z. Liu, New J. Phys. **25**, 033033 (2023).
[70] T. Cao, Z. Li, and S. G. Louie, Phys. Rev. Lett. **114**, 236602 (2015).
[71] B. Fu, W. Feng, X. Zhou, and Y. Yao, 2D Mater. **4**, 025107 (2017).
[72] S. Jiang and G.-p. Zheng, Phys. Status Solidi B **260**, 2200269 (2023).
[73] L. Seixas, A. S. Rodin, A. Carvalho, and A. H. Castro Neto, Phys. Rev. Lett. **116**, 206803 (2016).
[74] M.-W. Chen, H. Kim, D. Ovchinnikov, A. Kuc, T. Heine, O. Renault, and A. Kis, npj 2D Mater. Appl. **2**, 2 (2018).
[75] M.-Y. Liu, Y. He, Y. Mao, and K. Xiong, Phys. Rev. B **105**, 035418 (2022).
[76] D. Suszalski, G. Rut, and A. Rycerz, Phys. Rev. B **97**, 125403 (2018).
[77] S. Singh, Z. Zanolli, M. Amsler, B. Belhadji, J. O. Sofo, M. J. Verstraete, and A. H. Romero, J. Phys. Chem. Lett. **10**, 7324 (2019).
[78] N. Miao, B. Xu, N. C. Bristowe, J. Zhou, and Z. Sun, J. Am. Chem. Soc. **139**, 11125 (2017).
[79] Y. Nie, M. Rahman, P. Liu, A. Sidike, Q. Xia, and G.-h. Guo, Phys. Rev. B **96**, 075401 (2017).
[80] V. Zólyomi, N. D. Drummond, and V. I. Fal'ko, Phys. Rev. B **87**, 195403 (2013).
[81] R. Meng, M. Houssa, K. Iordanidou, G. Pourtois, V. Afanasiev, and A. Stesmans, Phys. Rev. Mater. **4**, 074001 (2020).
[82] N. Liu, S. Zhou, and J. Zhao, J. Phys. Chem. Lett. **13**, 590 (2022).
[83] M.-Y. Liu, L. Gong, Y. He, and C. Cao, Phys. Rev. B **104**, 035409 (2021).
[84] C. Rudderham and J. Maassen, J. Appl. Phys. **127**, 065105 (2020).
[85] M. Nurhuda, A. R. T. Nugraha, M. Y. Hanna, E. Suprayoga, and E. H. Hasdeo, Adv. Nat. Sci: Nanosci. Nanotechnol. **11**, 015012 (2020).
[86] D. Wickramaratne, F. Zahid, and R. K. Lake, J. Appl. Phys. **118**, 075101 (2015).
[87] A. Majumdar, S. Chowdhury, and R. Ahuja, ACS Appl. Energy Mater. **3**, 9315 (2020).
[88] B. Özdamar, G. Özbal, M. N. m. c. Çınar, K. Sevim, G. Kurt, B. Kaya, and H. Sevinçli, Phys. Rev. B **98**, 045431 (2018).
[89] D. H. Ozbey, M. J. Varjovi, G. O. Sargın, H. Sevinçli, and E. Durgun, Phys. Rev. B **110**, 035411 (2024).
[90] R. N. Somaiya, Y. A. Sonvane, and S. K. Gupta, Phys. Chem. Chem. Phys. **22**, 3990 (2020).
[91] Z. Xu and G. Gao, 2D Mater. **12**, 025024 (2025).
[92] P. Ghaemi, R. S. K. Mong, and J. E. Moore, Phys. Rev. Lett. **105**, 166603 (2010).
[93] Y. Xu, Z. Gan, and S.-C. Zhang, Phys. Rev. Lett. **112**, 226801 (2014).
[94] I. T. Witting, F. Ricci, T. C. Chasapis, G. Hautier, and G. J. Snyder, Research **2020**, 2020 (2020).
[95] L. Li, J. Jia, C. Shi, and W. Zeng, Molecules **27**, 8183 (2022).
[96] J. Liang, L. Cheng, J. Zhang, H. Liu, and Z. Zhang, Nanoscale **8**, 8855 (2016).
[97] M. Gaffar, S. A. Wella, and E. H. Hasdeo, Phys. Rev. B **104**, 205105 (2021).
[98] T.-H. Wang and H.-T. Jeng, ACS Appl. Energy Mater. **1**, 5646 (2018).
[99] C. Fu, Y. Sun, and C. Felser, APL Mater. **8**, 040913 (2020).
[100] N. Xu, Y. Xu, and J. Zhu, npj Quant. Mater. **2**, 51 (2017).
[101] D. Baldomir and D. Faílde, Sci. Rep. **9**, 6324 (2019).
[102] S. Roychowdhury, M. Samanta, A. Banik, and K. Biswas, J. Solid State Chem. **275**, 103 (2019).
[103] H. Usui and K. Kuroki, J. Appl. Phys. **121**, 165101 (2017).
[104] H. Usui, K. Suzuki, K. Kuroki, S. Nakano, K. Kudo, and M. Nohara, Phys. Rev. B **88**, 075140 (2013).
[105] J. M. Adhidewata, A. R. T. Nugraha, E. H. Hasdeo, P. Estelle, and B. E. Gunara, Materials Today Communications **31**, 103737 (2022).
[106] C. Wang, Z. Xu, K. Xu, and G. Gao, Molecules **26**, 6376 (2021).
[107] S. Wei, C. Wang, S. Fan, and G. Gao, J. Appl. Phys. **127**, 155103 (2020).
[108] C. Wang, S. Wei, and G. Gao, ACS Appl. Nano Mater. **2**, 4061 (2019).
[109] Q. Tian, W. Zhang, Z. Qin, and G. Qin, Nanoscale **13**, 18032 (2021).
[110] K. Kuroki and R. Arita, J. Phys. Soc. Jpn. **76**, 083707 (2007).
[111] L. Wu, J. Yang, S. Wang, P. Wei, J. Yang, W. Zhang, and L. Chen, Phys. Rev. B **90**, 195210 (2014).
[112] L. Wu, J. Yang, S. Wang, P. Wei, J. Yang, W. Zhang, and L. Chen, Appl. Phys. Lett. **105**, 202115 (2014).
[113] J. Yuan, Y. Cai, L. Shen, Y. Xiao, J.-C. Ren, A. Wang, Y. P. Feng, and X. Yan, Nano Energy **52**, 163 (2018).
[114] A. Bafekry, M. Faraji, M. M. Fadlallah, D. M. Hoat, H. R. Jappor, I. A. Sarsari, M. Ghergherehchi, and S. A. H. Feghhi, Phys. Chem. Chem. Phys. **23**, 25866 (2021).
[115] S.-D. Guo, A.-X. Zhang, and H.-C. Li, Nanotechnology **28**, 445702 (2017).
[116] L. Zhang, Y. Gu, and A. Du, ACS Omega **6**, 31919 (2021).
[117] S. Babaee Touski and N. Ghobadi, Phys. Rev. B **103**, 165404 (2021).
[118] Q. Xia, Z. Xu, L. Zhang, and G. Gao, J. Appl. Phys. **136**, 044304 (2024).
[119] Y. Pei, H. Wang, and G. J. Snyder, Adv. Mater. **24**, 6125 (2012).
[120] G. Özbal, R. T. Senger, C. Sevik, and H. Sevinçli, Phys. Rev. B **100**, 085415 (2019).
[121] Y. Huang, H. Yuan, and H. Chen, Phys. Chem. Chem. Phys. **25**, 1808 (2023).
[122] X. Liu, L. Li, C. Yang, C. Bai, and J. Li, J. Mater. Chem. A **11**, 21735 (2023).
[123] Y. Wu, B. Hou, C. Ma, J. Cao, Y. Chen, Z. Lu, H. Mei, H. Shao, Y. Xu, H. Zhu, *et al.*, Mater. Horiz. **8**, 1253 (2021).
[124] T. Sohier, M. Gibertini, D. Campi, G. Pizzi, and N. Marzari, Nano Lett. **19**, 3723 (2019).

[125] Y. Wu, B. Hou, Y. Chen, J. Cao, H. Shao, Y. Zhang, C. Ma, H. Zhu, R. Zhang, and H. Zhang, npj Comput. Mater. **7**, 145 (2021).

[126] Y. Nakamura, T. Zhao, J. Xi, W. Shi, D. Wang, and Z. Shuai, Adv. Elect. Mater. **3**, 1700143 (2017).

[127] Y. Wu, J. He, Y. Chen, M. Kong, Y. Zhang, X. Hu, J. Lian, H. Zhang, and R. Zhang, Nanoscale **14**, 5462 (2022).

[128] A. Shafique, A. Samad, and Y.-H. Shin, Phys. Chem. Chem. Phys. **19**, 20677 (2017).

[129] H. S. Song, S. L. Li, L. Gao, Y. Xu, K. Ueno, J. Tang, Y. B. Cheng, and K. Tsukagoshi, Nanoscale **5**, 9666 (2013).

[130] H. Chen, C. Li, L. Shan, and L. Cheng, Phys. Rev. B **109**, 224103 (2024).

[131] T. G. Pedersen, C. Flindt, J. Pedersen, N. A. Mortensen, A.-P. Jauho, and K. Pedersen, Phys. Rev. Lett. **100**, 136804 (2008).

[132] J. A. Fürst, J. G. Pedersen, C. Flindt, N. A. Mortensen, M. Brandbyge, T. G. Pedersen, and A.-P. Jauho, New J. Phys. **11**, 095020 (2009).

[133] X. Liang, Y.-S. Jung, S. Wu, A. Ismach, D. L. Olynick, S. Cabrini, and J. Bokor, Nano Lett. **10**, 2454 (2010).

[134] N. S. Safron, A. S. Brewer, and M. S. Arnold, Small **7**, 492 (2011).

[135] M. Sharafat Hossain, F. Al-Dirini, F. M. Hossain, and E. Skafidas, Sci. Rep. **5**, 11297 (2015).

[136] T. Gunst, T. Markussen, A.-P. Jauho, and M. Brandbyge, Phys. Rev. B **84**, 155449 (2011).

[137] H. Karamitaheri, M. Pourfath, R. Faez, and H. Kosina, ECS Trans. **35**, 185 (2011).

[138] H. Sadeghi, S. Sangtarash, and C. J. Lambert, Beilstein J. Nanotechnol. **6**, 1176 (2015).

[139] M. Yamawaki, M. Ohnishi, S. Ju, and J. Shiomi, Sci. Adv. **4**, eaar4192 (2018).

[140] Y. Yan, Q.-F. Liang, H. Zhao, C.-Q. Wu, and B. Li, Phys. Lett. A **376**, 2425 (2012).

[141] J. Oh, H. Yoo, J. Choi, J. Y. Kim, D. S. Lee, M. J. Kim, J.-C. Lee, W. N. Kim, J. C. Grossman, J. H. Park, *et al.*, Nano Energy **35**, 26 (2017).

[142] N. Herrera-Reinoza, A. C. dos Santos, L. H. de Lima, R. Landers, and A. de Siervo, Chem. Mater. **33**, 2871 (2021).

[143] L. Ci, L. Song, C. Jin, D. Jariwala, D. Wu, Y. Li, A. Srivastava, Z. F. Wang, K. Storr, L. Balicas, F. Liu, and P. M. Ajayan, Nat. Mater. **9**, 430 (2010).

[144] M. Liu, Y. Li, P. Chen, J. Sun, D. Ma, Q. Li, T. Gao, Y. Gao, Z. Cheng, X. Qiu, *et al.*, Nano Lett. **14**, 6342 (2014).

[145] H. Sevinçli, M. Topsakal, and S. Ciraci, Phys. Rev. B **78**, 245402 (2008).

[146] C.-C. Chen, Z. Li, L. Shi, and S. B. Cronin, Nano Res. **8**, 666 (2015).

[147] H. Sevinçli, W. Li, N. Mingo, G. Cuniberti, and S. Roche, Phys. Rev. B **84**, 205444 (2011).

[148] K. Yang, Y. Chen, R. D'Agosta, Y. Xie, J. Zhong, and A. Rubio, Phys. Rev. B **86**, 045425 (2012).

[149] Y. Yokomizo and J. Nakamura, Appl. Phys. Lett. **103**, 113901 (2013).

[150] V.-T. Tran, J. Saint-Martin, and P. Dollfus, Nanotechnology **26**, 495202 (2015).

[151] J.-W. Jiang, J.-S. Wang, and B.-S. Wang, Appl. Phys. Lett. **99**, 043109 (2011).

[152] J. Wang, X. Mu, X. Wang, N. Wang, F. Ma, W. Liang, and M. Sun, Mater. Today Phys. **5**, 29 (2018).

[153] A. Kınacı, J. B. Haskins, C. Sevik, and T. Çağın, Phys. Rev. B **86**, 115410 (2012).

[154] J. Duan, X. Wang, X. Lai, G. Li, K. Watanabe, T. Taniguchi, M. Zebarjadi, and E. Y. Andrei, Proc. Natl. Acad. Sci. USA **113**, 14272 (2016).

[155] W.-Y. Lee, M.-S. Kang, G.-S. Kim, J. W. Choi, N.-W. Park, Y. Sim, Y.-H. Kim, M.-J. Seong, Y.-G. Yoon, E. Saitoh, and S.-K. Lee, ACS Nano **16**, 3404 (2022).

[156] T. Wang, C. Liu, F. Jiang, Z. Xu, X. Wang, X. Li, C. Li, J. Xu, and X. Yang, Phys. Chem. Chem. Phys. **19**, 17560 (2017).

[157] S. Kim, H. Bark, S. Nam, H. Choi, and H. Lee, ACS Sustainable Chem. Eng. **6**, 15487 (2018).

[158] Z. Mao, Z. Wang, T. Shi, P.-a. Zong, J. Liang, Z. Liu, P. Zhang, Y. Huang, Y. Han, K. Ahmad, Z. Almutairi, and C. Wan, Adv. Mater. Interfaces **9**, 2200555 (2022).

[159] M.-Q. Liu, Y.-L. Li, and Z.-G. Sun, Physica E **143**, 115358 (2022).

[160] Z. Wang, C. Zhang, J. Zhang, J. liang, Z. Liu, F. Hang, Y. Xuan, X. Wang, M. Chen, S. Tang, and P.-an Zong, ACS Appl. Energy Mater. **5**, 11351 (2022).

[161] F. M. Gonzalo, M. J. Piotrowski, E. R. Delgado, C. A. P. Bravo, J. A. C. García, J. S. A. Arenas, and E. M. Flores, Sci. Rep. **14**, 26844 (2024).

[162] Y. Ouyang and J. Guo, Appl. Phys. Lett. **94**, 263107 (2009).

[163] P. A. Almeida and G. B. Martins, J. Phys.: Condens. Matter **34**, 335302 (2022).

[164] H. Sevinçli, C. Sevik, T. Çağın, and G. Cuniberti, Sci. Rep. **3**, 1228 (2013).

[165] M. S. Hossain, D. H. Huynh, P. D. Nguyen, L. Jiang, T. C. Nguyen, F. Al-Dirini, F. M. Hossain, and E. Skafidas, J. Appl. Phys. **119**, 125106 (2016).

[166] S. Ganguly and S. K. Maiti, J. Phys. D: Appl. Phys. **54**, 025301 (2021).

[167] H. Sevinçli and G. Cuniberti, Phys. Rev. B **81**, 113401 (2010).

[168] X. Huang, S. Ma, H. Wang, S. Lin, C. Zhao, H. Wang, and S. Ju, Int. J. Heat Mass Transf. **197**, 123332 (2022).

[169] X. Cui, T. Ouyang, J. Li, C. He, C. Tang, and J. Zhong, Phys. Chem. Chem. Phys. **20**, 7173 (2018).

[170] P. S. E. Yeo, M. B. Sullivan, K. P. Loh, and C. K. Gan, J. Mater. Chem. A **1**, 10762 (2013).

[171] S. Deng, X. Cai, Y. Zhang, and L. Li, Carbon **145**, 622 (2019).

[172] S. Deng, L. Li, and P. Rees, Carbon **155**, 438 (2019).

[173] J. Oh, Y. Kim, S. Chung, H. Kim, and J. G. Son, Adv. Mater. Interfaces **6**, 1901333 (2019).

[174] Q.-Y. Li, T. Feng, W. Okita, Y. Komori, H. Suzuki, T. Kato, T. Kaneko, T. Ikuta, X. Ruan, and K. Takahashi, ACS Nano **13**, 9182 (2019).

[175] L. J. Wirth and A. A. Farajian, J. Phys. Chem. C **122**, 8843 (2018).

[176] W. Cao, H. Xiao, T. Ouyang, and J. Zhong, J. Appl. Phys. **122**, 174302 (2017).

[177] J. Zhang, H. J. Liu, L. Cheng, J. Wei, J. H. Liang, D. D. Fan, J. Shi, X. F. Tang, and Q. J. Zhang, Sci. Rep. **4**, 6452 (2014).

[178] X. Jiang, C. Ban, L. Li, C. Wang, W. Chen, and X. Liu, AIP Advances **11**, 055120 (2021).

[179] K. Zberecki, R. Swirkowicz, and J. Barnaś, Phys. Chem. Chem. Phys. **17**, 22448 (2015).

[180] R. Ma, H. Geng, W. Y. Deng, M. N. Chen, L. Sheng, and D. Y. Xing, Phys. Rev. B **94**, 125410 (2016).

[181] D. D. Fan, H. J. Liu, L. Cheng, P. H. Jiang, J. Shi, and X. F. Tang, Appl. Phys. Lett. **105**, 133113 (2014).

[182] X. Liu, G. Zhang, Q.-X. Pei, and Y.-W. Zhang, Appl. Phys. Lett. **103**, 133113 (2013).

[183] J. Wang, F. Xie, X.-H. Cao, S.-C. An, W.-X. Zhou, L.-M. Tang, and K.-Q. Chen, Sci. Rep. **7**, 41418 (2017).

[184] E. Unsal, R. T. Senger, and H. Sevinçli, Phys. Rev. B **103**, 014104 (2021).

[185] Y.-Y. Liu, Y.-J. Zeng, P.-Z. Jia, X.-H. Cao, X. Jiang, and K.-Q. Chen, J. Phys.: Condens. Matter **30**, 275701 (2018).

[186] D. Han, M. Wang, X. Yang, M. Du, L. Cheng, and X. Wang, J. Alloys Compd. **903**, 163850 (2022).

[187] Z. Zhang, Y. Xie, Q. Peng, and Y. Chen, Sci. Rep. **6**, 21639 (2016).

[188] Y. Ouyang, Y. Xie, Z. Zhang, Q. Peng, and Y. Chen, J. Appl. Phys. **120**, 235109 (2016).

[189] A. Arab, A. V. Davydov, D. A. Papaconstantopoulos, and Q. Li, J. Electron. Mater. **45**, 5253 (2016).

[190] J. Bera and S. Sahu, RSC Adv. **9**, 25216 (2019).

[191] S.-D. Guo, Comput. Mater. Sci. **123**, 8 (2016).

[192] Dimple, N. Jena, and A. D. Sarkar, J. Phys.: Condens. Matter **29**, 225501 (2017).

[193] K. Yuan, X. Zhang, L. Li, and D. Tang, Phys. Chem. Chem. Phys. **21**, 468 (2019).

[194] A. Shafique and Y.-H. Shin, Phys. Chem. Chem. Phys. **19**, 32072 (2017).

[195] H. K. Ng, D. Xiang, A. Suwardi, G. Hu, K. Yang, Y. Zhao, T. Liu, Z. Cao, H. Liu, S. Li, *et al.*, Nat. Electron. **5**, 489 (2022).

[196] X. Zhao, G. Tang, Y. Li, M. Zhang, and Y. Nie, ACS Appl. Electron. Mater. **3**, 2995 (2021).

[197] H.-Y. Song, J.-J. Sun, and M. Li, Chem. Phys. Lett. **784**, 139109 (2021).

[198] H. Wang, Y.-S. Lan, B. Dai, X.-W. Zhang, Z.-G. Wang, and N.-N. Ge, ACS Omega **6**, 29820 (2021).

[199] M. Narimani, S. Yalameha, and Z. Nourbakhsh, Physica E **134**, 114818 (2021).

[200] G. Li, K. Yao, and G. Gao, Nanotechnology **29**, 015204 (2018).

[201] H. Y. Lv, W. J. Lu, D. F. Shao, H. Y. Lu, and Y. P. Sun, J. Mater. Chem. C **4**, 4538 (2016).

[202] R. D'Souza, S. Mukherjee, and S. Ahmad, J. Appl. Phys. **126**, 214302 (2019).

[203] D. Qin, X.-J. Ge, G.-q. Ding, G.-y. Gao, and J.-T. Lü, RSC Adv. **7**, 47243 (2017).

[204] F. Saiz and R. Rurali, Nano Express **1**, 010026 (2020).

[205] F. Saiz, J. Carrete, and R. Rurali, Nanoscale Adv. **2**, 5352 (2020).

[206] R. Chaurasiya, S. Tyagi, N. Singh, S. Auluck, and A. Dixit, J. Alloys Compd. **855**, 157304 (2021).

[207] S.-D. Guo, X.-S. Guo, and Y. Deng, J. Appl. Phys. **126**, 154301 (2019).

[208] S. Ahmad, F. Khan, B. Amin, and I. Ahmad, J. Solid State Chem. **299**, 122189 (2021).

[209] M. M. Cicek, M. Demirtas, and E. Durgun, J. Appl. Phys. **129**, 234302 (2021).

[210] L. W. Sprague, C. Huang, J.-P. Song, and B. M. Rubenstein, J. Phys. Chem. C **123**, 25437 (2019).

[211] Q. Wang, L. Han, L. Wu, T. Zhang, S. Li, and P. Lu, Nanoscale Res. Lett. **14**, 287 (2019).

[212] W. Ibarra-Hernández, A. C. Garcia-Castro, A. Bautista-Hernández, M. Salazar-Villanueva, A. Cantarero, and A. H. Romero, Phys. Rev. Mater. **6**, 025403 (2022).

[213] M.-S. Li, K.-X. Chen, D.-C. Mo, and S.-S. Lyu, Phys. Chem. Chem. Phys. **21**, 24695 (2019).

[214] P. Liu, M. Wu, G. Abbas, W. Yang, F. Liu, and Y. Li, Comput. Mater. Sci. **207**, 111271 (2022).

[215] R. Gupta, S. Kakkar, B. Dongre, J. Carrete, and C. Bera, ACS Appl. Energy Mater. **6**, 3944 (2023).

[216] S. Nag, R. Singh, and R. Kumar, Phys. Chem. Chem. Phys. **24**, 211 (2022).

[217] F. Xiong, H. B. Tan, C. Xia, and Y. Chen, ACS Appl. Nano Mater. **3**, 114 (2020).

[218] Y. Li, K. Ma, X. Fan, F. Liu, J. Li, and H. Xie, Appl. Surf. Sci. **521**, 146256 (2020).

[219] M. A. tamerd, M. Zanouni, A. Nid-bahami, M. Diani, and A. Marjaoui, Int. J. Quantum Chem. **122**, e26906 (2022).

[220] S.-B. Chen, G. Liu, W.-J. Yan, C.-E. Hu, X.-R. Chen, and H.-Y. Geng, Nanomaterials **12**, 40 (2022).

[221] N. Wang, M. Li, H. Xiao, H. Gong, Z. Liu, X. Zu, and L. Qiao, Phys. Chem. Chem. Phys. **21**, 15097 (2019).

[222] M. A. Mohebpour, S. I. Vishkayi, and M. B. Tagani, Phys. Chem. Chem. Phys. **22**, 23246 (2020).

[223] J. Ma, F. Meng, J. He, Y. Jia, and W. Li, ACS Appl. Mater. Interfaces **12**, 43901 (2020).

[224] S. Karmakar and T. Saha-Dasgupta, Phys. Rev. Mater. **5**, 124006 (2021).

[225] N. Gupta and R. Verma, Superlattices Microstruct. **156**, 106944 (2021).

[226] H. Alavi-Rad, A. Kiani-Sarkaleh, S. Rouhi, and A. Ghadimi, Physica E **124**, 114339 (2020).

[227] H. Y. Lv, W. J. Lu, D. F. Shao, and Y. P. Sun, Phys. Rev. B **90**, 085433 (2014).

[228] Y. D. Kuang, L. Lindsay, S. Q. Shi, and G. P. Zheng, Nanoscale **8**, 3760 (2016).

[229] Y. Wu, K. Xu, C. Ma, Y. Chen, Z. Lu, H. Zhang, Z. Fang, and R. Zhang, Nano Energy **63**, 103870 (2019).

[230] Z. Shao, X. Wang, H. Qiu, H. Sun, Y. Cao, X. Wu, and X. Chen, Results Phys. **58**, 107541 (2024).

[231] Q. Xia, Y. Liu, and G. Gao, J. Mater. Chem. C **13**, 5689 (2025).

[232] G. O. Sargin, S. Demirci, K. Gong, and V. O. Özçelik, Phys. Rev. Mater. **9**, 024003 (2025).

[233] S. A. Khandy, K. Kaur, S. Marutheeswaran, and I. Islam, ACS Appl. Energy Mater. **7**, 9279 (2024).

[234] A. F. Wani, S. A. Khandy, A. S. Verma, S. Dhiman, and K. Kaur, Sci. Rep. **14**, 29555 (2024).

[235] S. Zhou, Y. Guo, and J. Zhao, Phys. Chem. Chem. Phys. **18**, 10607 (2016).

[236] J. Y. Kim and J. C. Grossman, Nano Lett. **15**, 2830 (2015).

[237] H. Zhang, A. F. Fonseca, and K. Cho, J. Phys. Chem. C **118**, 1436 (2014).

[238] J. Y. Kim, J.-H. Lee, and J. C. Grossman, ACS Nano **6**, 9050 (2012).

[239] K. Sevim and H. Sevinçli, Carbon **140**, 603 (2018).

[240] N. Xiao, X. Dong, L. Song, D. Liu, Y. Tay, S. Wu, L.-J. Li, Y. Zhao, T. Yu, H. Zhang, *et al.*, ACS Nano **5**, 2749 (2011).

[241] X. Shen, X. Lin, J. Jia, Z. Wang, Z. Li, and J.-K. Kim, Carbon **80**, 235 (2014).

[242] D. Sim, D. Liu, X. Dong, N. Xiao, S. Li, Y. Zhao, L.-J. Li, Q. Yan, and H. H. Hng, J. Phys. Chem. C **115**, 1780 (2011).

[243] W. Kim, W. Lee, S.-M. Lee, D. Kim, and J. Park, Nanotechnology **33**, 175702 (2022).

[244] B.-Y. Cao, W.-J. Yao, and Z.-Q. Ye, Carbon **96**, 711 (2016).

[245] M. Khazaei, M. Arai, T. Sasaki, C.-Y. Chung, N. S. Venkataramanan, M. Estili, Y. Sakka, and Y. Kawazoe, Adv. Funct. Mater. **23**, 2185 (2013).

[246] M. Khazaei, M. Arai, T. Sasaki, M. Estili, and Y. Sakka, Phys. Chem. Chem. Phys. **16**, 7841 (2014).

[247] H. Kim, B. Anasori, Y. Gogotsi, and H. N. Alshareef, Chem. Mater. **29**, 6472 (2017).

[248] Z. Jing, H. Wang, X. Feng, B. Xiao, Y. Ding, K. Wu, and Y. Cheng, J. Phys. Chem. Lett. **10**, 5721 (2019).

[249] S. Sarikurt, D. Çakır, M. Keçeli, and C. Sevik, Nanoscale **10**, 8859 (2018).

[250] Z. Jing, X. Feng, Y. Qiu, N. Li, K. Wu, Y. Cheng, and B. Xiao, J. Phys. Chem. C **127**, 14125 (2023).

[251] Y. F. Li, G. H. Tang, and B. Fu, Phys. Rev. B **99**, 235428 (2019).

[252] C. Leng, D. Ren, and L. Zhang, Results Phys. **36**, 105422 (2022).

[253] Y. Lu, H. Li, J. Rong, X. Yu, Y. Sui, and Z. Liu, Diam. Relat. Mater. **154**, 112209 (2025).

[254] T. Zhang, J. Peng, T. Yang, X. Li, and L. Zhu, J. Phys. Chem. C **126**, 18505 (2022).

[255] M. A. Mohebpour, S. M. Mozvashi, S. I. Vishkayi, and M. B. Tagani, Sci. Rep. **11**, 23840 (2021).

[256] M.-S. Li, D.-C. Mo, and S.-S. Lyu, Sci. Rep. **11**, 10030 (2021).

[257] S.-Z. Huang, C.-G. Fang, J.-X. Guo, B.-Y. Wang, H.-D. Yang, Q.-Y. Feng, B. Li, X. Xiang, X.-T. Zu, and H.-X. Deng, J. Colloid Interface Sci. **639**, 14 (2023).

[258] R. Abinaya, S. Harish, S. Ponnusamy, M. Shimomura, M. Navaneethan, and J. Archana, Chem. Eng. J. **416**, 128484 (2021).

[259] M. Kayyalha, J. Maassen, M. Lundstrom, L. Shi, and Y. P. Chen, J. Appl. Phys. **120**, 134305 (2016).

[260] J. Wu, Y. Liu, Y. Liu, Y. Cai, Y. Zhao, H. K. Ng, K. Watanabe, T. Taniguchi, G. Zhang, C.-W. Qiu, D. Chi, A. H. C. Neto, J. T. L. Thong, K. P. Loh, and K. Hippalgaonkar, Proc. Natl. Acad. Sci. USA **117**, 13929 (2020).

[261] H. Qin, K. Ren, Z. Guoqiang, Y. Dai, and G. Zhang, Phys. Chem. Chem. Phys. **24**, 20437 (2022).

[262] D. Chen, H. Chen, S. Hu, H. Guo, S. W. Sharshir, M. An, W. Ma, and X. Zhang, J. Alloys Compd. **831**, 154875 (2020).

[263] M. Sharma, A. Kumar, and P. Ahluwalia, Physica E **107**, 117 (2019).

[264] R. Kumar, Appl. Phys. A **127**, 635 (2021).

[265] C. Adessi, S. Pecorario, S. Thébaud, and G. Bouzerar, Phys. Chem. Chem. Phys. **22**, 15048 (2020).

[266] M. Choi, T. G. Novak, J. Byen, H. Lee, J. Baek, S. Hong, K. Kim, J. Song, H. Shin, and S. Jeon, ACS Appl. Mater. Interfaces **13**, 24304 (2021).

[267] D. Singh, V. Shukla, and R. Ahuja, Phys. Rev. B **102**, 075444 (2020).

[268] W. Zeng, X.-M. Tao, S. Lin, C. Lee, D. Shi, K. ho Lam, B. Huang, Q. Wang, and Y. Zhao, Nano Energy **54**, 163 (2018).

[269] Y. Anno, M. Takeuchi, M. Matsuoka, K. Takei, S. Akita, and T. Arie, Appl. Phys. Lett. **110**, 263501 (2017).

[270] Y. Anno, Y. Imakita, K. Takei, S. Akita, and T. Arie, 2D Mater. **4**, 025019 (2017).

[271] Z. Gholami and F. Khoeini, Sci. Rep. **11**, 15320 (2021).

[272] C. Cui, T. Ouyang, C. Tang, C. He, J. Li, C. Zhang, and J. Zhong, Carbon **176**, 52 (2021).

[273] V. Karthikeyan, S. L. Oo, J. U. Surjadi, X. Li, V. C. S. Theja, V. Kannan, S. C. Lau, Y. Lu, K.-H. Lam, and V. A. L. Roy, ACS Appl. Mater. Interfaces **13**, 58701 (2021).

[274] H. Q. Yang, X. Y. Wang, H. Wu, B. Zhang, D. D. Xie, Y. J. Chen, X. Lu, X. D. Han, L. Miao, and X. Y. Zhou, J. Mater. Chem. C **7**, 3351 (2019).

[275] W. Zheng, W. Cao, Z. Wang, H. Deng, J. Shi, and R. Xiong, Beilstein J. Nanotechnol. **10**, 2031 (2019).

[276] H. Yu, Y. Li, D. Wei, G. Guo, Z. Feng, J. Ye, Q. Luo, Y. Ma, Y. Tang, and X. Dai, Micro Nanostruct. **165**, 207188 (2022).

[277] I. Ozdemir, A. W. Holleitner, C. Kastl, and O. Ü. Aktürk, Sci. Rep. **12**, 12756 (2022).

[278] Z. Yu, M. Li, Y. Yang, P. Yu, A. Suwardi, L. Zhang, and Y. Zhao, Adv. Elect. Mater. **11**, 2400634 (2025).

[279] Z. Wan, X. Liu, C. Liu, C. Liu, P. Liu, R. Tan, Q. Zhang, Z. Chen, J. Xu, and F. Jiang, Small **21**, 2410854 (2025).

[280] Y.-N. Peng, J.-F. Yu, X.-H. Cao, D. Wu, P.-Z. Jia, W.-X. Zhou, and K.-Q. Chen, Physica E **122**, 114160 (2020).

[281] H. Sadeghi, S. Sangtarash, and C. J. Lambert, Sci. Rep. **5**, 9514 (2015).

[282] C. Núñez, M. Saiz-Bretín, P. A. Orellana, L. Rosales, and F. Domínguez-Adame, J. Phys.: Condens. Matter **32**, 275301 (2020).

[283] R.-L. An, X.-F. Wang, P. Vasilopoulos, Y.-S. Liu, A.-B. Chen, Y.-J. Dong, and M.-X. Zhai, J. Phys. Chem. C **118**, 21339 (2014).

[284] Y.-B. Dai, K. Luo, and X.-F. Wang, Sci. Rep. **10**, 9105 (2020).

[285] M. Rezaei, H. Karbaschi, M. Amini, M. Soltani, and G. Rashedi, Nanotechnology **32**, 375704 (2021).

[286] L. J. Wirth, T. H. Osborn, and A. A. Farajian, Appl. Phys. Lett. **109**, 173102 (2016).

[287] V.-T. Tran, J. Saint-Martin, P. Dollfus, and S. Volz, Sci. Rep. **7**, 2313 (2017).

[288] A. Aydin, A. Sisman, J. Fransson, A. M. Black-Schaffer, and P. Dutta, J. Phys.: Condens. Matter **34**, 195304 (2022).

[289] M. A. Bazrafshan and F. Khoeini, Sci. Rep. **12**, 18419 (2022).

[290] M. Yoshida, T. Iizuka, Y. Saito, M. Onga, R. Suzuki, Y. Zhang, Y. Iwasa, and S. Shimizu, Nano Lett. **16**, 2061 (2016).

[291] Y. Saito, T. Iizuka, T. Koretsune, R. Arita, S. Shimizu, and Y. Iwasa, Nano Lett. **16**, 4819 (2016).

[292] D. Joseph, M. Navaneethan, R. Abinaya, S. Harish, J. Archana, S. Ponnusamy, K. Hara, and Y. Hayakawa, Appl. Surf. Sci. **505**, 144066 (2020).

[293] T. Horiguchi, T. Hamada, M. Hamada, I. Muneta, K. Kakushima, K. Tsutsui, T. Tatsumi, S. Tomiya, and H. Wakabayashi, Jpn. J. Appl. Phys. **61**, 075506 (2022).

[294] Z.-F. Zhou, G.-K. Ren, X. Tan, R. Liu, C. Liu, Y.-H. Lin, and C.-W. Nan, J. Mater. Chem. A **6**, 24128 (2018).

[295] M. A. Jenisha, S. Kavirajan, S. Harish, J. Archana, K. Kamalabharathi, E. S. Kumar, and M. Navaneethan, J. Alloys Compd. **895**, 162493 (2022).

[296] P. X. Thi, M. Miyata, H. Van Ngoc, P. T. Lam, N. T. Tung, M. Muruganathan, P. T. Tue, M. Akabori, D. H. Chi, H. Mizuta, Y. Takamura, and M. Koyano, Phys. Status Solidi B **255**, 1800125 (2018).

[297] I. Durán, C. Bueno-Blanco, J. Rodríguez-Muro, M. Martinez, E. Champa-Bujaico, P. Cancho García, D.-Y. Lin, A. Marti, E. Antolin, and S. A. Svatek, ACS Appl. Energy Mater. **8**, 3500 (2025).

[298] Z. Yang, K. Liu, S. Chen, S. Zhong, J. Wu, X. Su, C. Uher, Q. Zhang, and X. Tang, ACS Appl. Energy Mater. **8**, 2378 (2025).

[299] L. Zhu, B. Li, and K. Yao, Nanotechnology **29**, 325206 (2018).

[300] S. Youn, J. Kim, H. Moon, J.-K. Kim, J. Jang, J. Chang, T. Lee, K. Kang, and W. Lee, Small **18**, 2200818 (2022).

[301] W. Lee, G. Lim, and S. H. Ko, Nano Energy **87**, 106188 (2021).

[302] X. Yu, J.-h. Liu, W.-X. Zhou, Z.-X. Xie, P.-Z. Jia, Y.-X. Deng, X.-H. Cao, Z.-Q. Fan, and D. Wu, Phys. Chem. Chem. Phys. **25**, 19082 (2023).

[303] R. M. Tromer, A. Freitas, I. M. Felix, B. Mortazavi, L. D. Machado, S. Azevedo, and L. F. C. Pereira, Phys. Chem. Chem. Phys. **22**, 21147 (2020).

[304] J. Deb, R. Mondal, U. Sarkar, and H. Sadeghi, ACS Omega **6**, 20149 (2021).

[305] H. J. Hwang, S.-Y. Kim, S. K. Lee, and B. H. Lee, Carbon **201**, 467 (2023).

[306] N. Liu, J. Liu, S. Wang, and K. Yao, Phys. Lett. A **384**, 126127 (2020).

[307] N. Liu, H. Zhu, Y. Feng, S. Zhu, K. Yao, and S. Wang, Physica E **138**, 115067 (2022).

[308] S. Ramezani Akbarabadi and M. Madadi Asl, Adv. Condens. Matter Phys. **2021**, 8110754 (2021).

[309] E. Rahmati, A. Bafekry, M. Faraji, D. Gogva, C. V. Nguyen, and M. Ghergherehchi, RSC Adv. **12**, 6174 (2022).

[310] H. Goldsmid, *Introduction to Thermoelectricity* (Springer, Berlin, 2009).

[311] A. F. Ioffe, L. S. Stil'bans, E. K. Iordanishvili, T. S. Stavitskaya, A. Gelbtuch, and G. Vineyard, Phys. Today **12**(5), 42 (1959).

[312] G. J. Snyder and E. S. Toberer, Nat. Mater. **7**, 105 (2008).

[313] Y. Pei, A. D. LaLonde, N. A. Heinz, X. Shi, S. Iwanaga, H. Wang, L. Chen, and G. J. Snyder, Adv. Mater. **23**, 5674 (2011).

[314] D. Rowe, *CRC Handbook of Thermoelectrics* (CRC Press, Boca Raton, FL, 1995).

[315] M. Dresselhaus, G. Chen, M. Tang, R. Yang, H. Lee, D. Wang, Z. Ren, J.-P. Fleurial, and P. Gogna, Adv. Mater. **19**, 1043 (2007).

[316] W. Li, L. Zheng, B. Ge, S. Lin, X. Zhang, Z. Chen, Y. Chang, and Y. Pei, Adv. Mater. **29**, 1605887 (2017).

[317] K. Biswas, J. He, I. D. Blum, C.-I. Wu, T. P. Hogan, D. N. Seidman, V. P. Dravid, and M. G. Kanatzidis, Nature (London) **489**, 414 (2012).

[318] L.-D. Zhao, S.-H. Lo, Y. Zhang, H. Sun, G. Tan, C. Uher, C. Wolverton, V. P. Dravid, and M. G. Kanatzidis, Nature (London) **508**, 373 (2014).

[319] G. Nolas, J. Sharp, and J. Goldsmid, *Thermoelectrics: Basic Principles and New Materials Developments* (Springer, Berlin, 2001).

[320] Z. Chen, Z. Jian, W. Li, Y. Chang, B. Ge, R. Hanus, J. Yang, Y. Chen, M. Huang, G. J. Snyder, and Y. Pei, Adv. Mater. **29**, 1606768 (2017).

[321] S. I. Kim, K. H. Lee, H. A. Mun, H. S. Kim, S. W. Hwang, J. W. Roh, D. J. Yang, W. H. Shin, X. S. Li, Y. H. Lee, G. J. Snyder, and S. W. Kim, Science **348**, 109 (2015).

[322] V. Oskotskii and I. Smirnov, *Defects in Crystals and Thermal Conductivity* (Nauka, Leningrad, 1975).

[323] M. Mukherjee, A. Srivastava, and A. K. Singh, J. Mater. Chem. C **10**, 12524 (2022).

[324] H. Haug and A. Jauho, *Quantum Kinetics in Transport and Optics of Semiconductors* (Springer, Berlin, 2007).

[325] G. Stefanucci and R. van Leeuwen, *Nonequilibrium Many-Body Theory of Quantum Systems: A Modern Introduction* (Cambridge University Press, Cambridge, 2013).

[326] G. Mahan, *Condensed Matter in a Nutshell* (Princeton University Press, Princeton, NJ, 2011).

[327] R. Kubo, J. Phys. Soc. Jpn. **12**, 570 (1957).

[328] R. Kubo, Rep. Prog. Phys. **29**, 255 (1966).

[329] D. J. Thouless, Philos. Mag. **32**, 877 (1975).

[330] S. Poncé, W. Li, S. Reichardt, and F. Giustino, Rep. Prog. Phys. **83**, 036501 (2020).

[331] D. Sangalli and A. Marini, Europhys. Lett. **110**, 47004 (2015).

[332] W. Li, J. Carrete, N. A. Katcho, and N. Mingo, Comput. Phys. Commun. **185**, 1747 (2014).

[333] J. Carrete, B. Vermeersch, A. Katre, A. van Roekeghem, T. Wang, G. K. Madsen, and N. Mingo, Comput. Phys. Commun. **220**, 351 (2017).

[334] M. Raya-Moreno, X. Cartoixà, and J. Carrete, Comput. Phys. Commun. **281**, 108504 (2022).

[335] F. Eriksson, E. Fransson, and P. Erhart, Adv. Theor. Simul. **2**, 1800184 (2019).

[336] R. Li, J.-X. Wang, E. Lee, and T. Luo, npj Comput. Mater. **8**, 29 (2022).

[337] B. Liao, B. Qiu, J. Zhou, S. Huberman, K. Esfarjani, and G. Chen, Phys. Rev. Lett. **114**, 115901 (2015).

[338] J.-Y. Yang, G. Qin, and M. Hu, Appl. Phys. Lett. **109**, 242103 (2016).

[339] Z. Tong, S. Li, X. Ruan, and H. Bao, Phys. Rev. B **100**, 144306 (2019).

[340] T. Wang, Z. Gui, A. Janotti, C. Ni, and P. Karandikar, Phys. Rev. Mater. **1**, 034601 (2017).

[341] Q. Xu, J. Zhou, T.-H. Liu, and G. Chen, Appl. Phys. Lett. **115**, 023903 (2019).

[342] T. Zhu, G. Yu, J. Xu, H. Wu, C. Fu, X. Liu, J. He, and X. Zhao, Adv. Elect. Mater. **2**, 1600171 (2016).

[343] D. D. Fan, H. J. Liu, L. Cheng, J. H. Liang, and P. H. Jiang, J. Mater. Chem. A **6**, 12125 (2018).

[344] Z. Tong, A. Pecchia, C. Yam, H. Bao, T. Dumitrică, and T. Frauenheim, Adv. Funct. Mater. **32**, 2111556 (2022).

[345] Z. Zhou, X. Yang, H. Fu, R. Wang, X. Lu, G. Wang, and X. Zhou, Adv. Funct. Mater. **32**, 2206974 (2022).

[346] L. Peng, A. Wu, Y. Xia, H. Zhang, Y. Yang, H. Shao, Y. Chen, J. Zhang, L. Shu, H. Zhu, Y. Zheng, and H. Zhang, J. Materiomics. **10**, 386 (2024).

[347] Y. Huang, J. Zhou, G. Wang, and Z. Sun, J. Am. Chem. Soc. **141**, 8503 (2019).

[348] Y. Sun, Z. Shuai, and D. Wang, J. Phys. Chem. C **123**, 12001 (2019).

[349] C. Liu, M. Yao, J. Yang, J. Xi, and X. Ke, Mater. Today Phys. **15**, 100277 (2020).

[350] N. Gupta and R. Verma, Mater. Sci. Semicond. Process. **153**, 107115 (2023).

[351] X. Gu, Z. Fan, and H. Bao, J. Appl. Phys. **130**, 210902 (2021).

[352] Y. Li, Y. Zhai, Z. Xuan, W. Guo, and H. Wang, J. Mol. Liq. **354**, 118877 (2022).

[353] J. Brorsson, A. Hashemi, Z. Fan, E. Fransson, F. Eriksson, T. Ala-Nissila, A. V. Krasheninnikov, H.-P. Komsa, and P. Erhart, Adv. Theor. Simul. **5**, 2100217 (2022).

[354] Y. Luo, M. Li, H. Yuan, H. Liu, and Y. Fang, npj Comput. Mater. **9**, 4 (2023).

[355] S. Baroni, R. Bertossa, L. Ercole, F. Grasselli, and A. Marcolongo, *Heat Transport in Insulators From Ab Initio Green-Kubo Theory* (Springer International Publishing, 2020), pp. 809–844.

[356] R. Bertossa, F. Grasselli, L. Ercole, and S. Baroni, Phys. Rev. Lett. **122**, 255901 (2019).

[357] Y. Srivastava and A. Jain, J. Appl. Phys. **134**, 225101 (2023).

[358] M. Qin, X. Zhang, J. Zhu, Y. Yang, Z. Ti, Y. Shen, X. Wang, X. Liu, and Y. Zhang, J. Mater. Chem. A **11**, 10612 (2023).

[359] Y. Wu, A. Huang, L. Ji, J. Ji, Y. Ding, and L. Zhou, J. Phys. Chem. Lett. **15**, 11525 (2024).

[360] Y. Zhang, Z. Tong, A. Pecchia, C. Yam, T. Dumitrică, and T. Frauenheim, Nanoscale **14**, 13053 (2022).

[361] X. Yang, Y.-S. Chen, Y.-H. Zheng, C.-W. Wu, G.-F. Xie, Y.-J. Zeng, and W.-X. Zhou, Appl. Phys. Lett. **124**, 072204 (2024).

[362] J. Lü, F. Xu, Y. Zhou, X. Mo, Y. Ouyang, and X. Tao, ACS Appl. Mater. Interfaces **16**, 24734 (2024).

[363] T. Zhang, Y.-R. Yang, X. Liu, J. Wang, Z. Liu, and Y. Liu, J. Mater. Chem. C **13**, 6207 (2025).

[364] X. Lu, D. T. Morelli, Y. Xia, F. Zhou, V. Ozolins, H. Chi, X. Zhou, and C. Uher, Adv. Energy Mater. **3**, 342 (2013).

[365] H. Liu, X. Shi, F. Xu, L. Zhang, W. Zhang, L. Chen, Q. Li, C. Uher, T. Day, and G. J. Snyder, Nat. Mater. **11**, 422 (2012).

[366] G. Tang, W. Wei, J. Zhang, Y. Li, X. Wang, G. Xu, C. Chang, Z. Wang, Y. Du, and L.-D. Zhao, J. Am. Chem. Soc. **138**, 13647 (2016).

[367] L.-D. Zhao, G. Tan, S. Hao, J. He, Y. Pei, H. Chi, H. Wang, S. Gong, H. Xu, V. P. Dravid, *et al.*, Science **351**, 141 (2016).

[368] D. Li, H. Zhao, S. Li, B. Wei, J. Shuai, C. Shi, X. Xi, P. Sun, S. Meng, L. Gu, Z. Ren, and X. Chen, Adv. Funct. Mater. **25**, 6478 (2015).

[369] P. Ying, X. Li, Y. Wang, J. Yang, C. Fu, W. Zhang, X. Zhao, and T. Zhu, Adv. Funct. Mater. **27**, 1604145 (2017).

[370] P. Ying, X. Liu, C. Fu, X. Yue, H. Xie, X. Zhao, W. Zhang, and T. Zhu, Chem. Mater. **27**, 909 (2015).

[371] S. Wang, J. Yang, L. Wu, P. Wei, J. Yang, W. Zhang, and Y. Grin, Chem. Mater. **27**, 1071 (2015).

[372] W. Li, S. Lin, B. Ge, J. Yang, W. Zhang, and Y. Pei, Adv. Sci. **3**, 1600196 (2016).

[373] M. K. Jana, K. Pal, A. Warankar, P. Mandal, U. V. Waghmare, and K. Biswas, J. Am. Chem. Soc. **139**, 4350 (2017).

[374] Y.-L. Pei, H. Wu, D. Wu, F. Zheng, and J. He, J. Am. Chem. Soc. **136**, 13902 (2014).

[375] M. Saleemi, M. S. Toprak, S. Li, M. Johnsson, and M. Muhammed, J. Mater. Chem. **22**, 725 (2012).

[376] D. Yang, W. Yao, Q. Chen, K. Peng, P. Jiang, X. Lu, C. Uher, T. Yang, G. Wang, and X. Zhou, Chem. Mater. **28**, 1611 (2016).

[377] A. I. Hochbaum, R. Chen, R. D. Delgado, W. Liang, E. C. Garnett, M. Najarian, A. Majumdar, and P. Yang, Nature (London) **451**, 163 (2008).

[378] R. Mulla, A. O. White, C. W. Dunnill, and A. R. Barron, Energy Adv. **2**, 606 (2023).

[379] G. Özbal Sargın, S. Sarikurt, H. Sevincli, and C. Sevik, J. Appl. Phys. **133**, 150902 (2023).

[380] X. Gu and R. Yang, Appl. Phys. Lett. **105**, 131903 (2014).

[381] M. Zulfiqar, Y. Zhao, G. Li, Z. Li, and J. Ni, Sci. Rep. **9**, 4571 (2019).

[382] R. Yan, J. R. Simpson, S. Bertolazzi, J. Brivio, M. Watson, X. Wu, A. Kis, T. Luo, A. R. Hight Walker, and H. G. Xing, ACS Nano **8**, 986 (2014).

[383] N. Peimyoo, J. Shang, W. Yang, Y. Wang, C. Cong, and T. Yu, Nano Res. **8**, 1210 (2015).

[384] L. Zhang, N. Wang, and Y. Li, Chem. Sci. **14**, 5266 (2023).

[385] S. Lee, S.-H. Kang, and Y.-K. Kwon, Sci. Rep. **9**, 5149 (2019).

[386] Q. Fan, J. Yang, Y. Liu, W. Zhang, H. Hou, and N. Wang, Results Phys. **49**, 106528 (2023).

[387] Q.-Y. Xie, J.-J. Ma, Q.-Y. Liu, P.-F. Liu, P. Zhang, K.-W. Zhang, and B.-T. Wang, Phys. Chem. Chem. Phys. **24**, 7303 (2022).

[388] V.-H. Chu, T.-H. Le, T.-T. Pham, and D.-L. Nguyen, RSC Adv. **13**, 4202 (2023).

[389] X. Liu, D. Zhang, H. Wang, Y. Chen, H. Wang, and Y. Ni, J. Appl. Phys. **130**, 185104 (2021).

[390] T. Zhao, Y. Sun, Z. Shuai, and D. Wang, Chem. Mater. **29**, 6261 (2017).

[391] B. Wang, X. Yan, X. Cui, and Y. Cai, ACS Appl. Nano Mater. **5**, 15441 (2022).

[392] R. Anbarasan, D. Kim, and J. H. Park, Comput. Mater. Sci. **247**, 113508 (2025).

[393] S.-H. Cao, Y.-Q. Lin, Z.-Y. Zeng, H.-Y. Geng, and X.-R. Chen, Appl. Surf. Sci. **680**, 161440 (2025).

[394] I. Maleki, S. M. V. Allaei, and S. S. Naghavi, Phys. Chem. Chem. Phys. **26**, 19724 (2024).

[395] Y.-Y. Wu, Q. Wei, J. Zou, and H. Yang, Phys. Chem. Chem. Phys. **23**, 19834 (2021).

[396] N. Khossossi, D. Singh, W. Luo, and R. Ahuja, Energy Technol. **10**, 2200400 (2022).

[397] B. Wan, Z. Gao, X. Huang, Y. Yang, L. Chen, Q. Wang, C. Fang, W. Shen, Y. Zhang, H. Ma, H. Gou, X. Jia, and Z. Zhang, ACS Appl. Energy Mater. **5**, 9549 (2022).

[398] A. Taheri, S. Pisana, and C. V. Singh, Nanoscale Adv. **4**, 2873 (2022).

[399] V. J. R. Rivera, F. M. Gonzalo, M. J. Piotrowski, and E. M. Flores, Results Phys. **68**, 108080 (2025).

[400] X. Song, X. Chen, G. Wang, L. Zhou, H. Yang, X. Li, H. Yang, Y. Shen, Y. Luo, and N. Wang, Phys. Chem. Chem. Phys. **25**, 24332 (2023).

[401] H. Qi, Z. Sun, C. Shen, Z. Chang, Z. Wang, X. Wang, M. Zhang, and N. Wang, ACS Appl. Energy Mater. **5**, 7371 (2022).

[402] X.-Y. Wang, X. Yang, X.-H. Meng, Y.-Q. Shen, Y. Shuai, Q. Ai, and Z.-X. Zhou, Phys. Chem. Chem. Phys. **26**, 29913 (2024).

[403] Q.-Y. Xie, P.-F. Liu, J.-J. Ma, F.-G. Kuang, K.-W. Zhang, and B.-T. Wang, Materials **15**, 3147 (2022).

[404] L. Chai, F. Zhang, Y. Bai, and B. Dong, J. Am. Ceram Soc. **107**, 7331 (2024).

[405] A. Lou, Q.-B. Liu, and H.-H. Fu, Phys. Rev. B **105**, 075431 (2022).

[406] E. Mamani Flores, V. J. Ramirez Rivera, F. Mamani Gonzalo, J. Ordonez-Miranda, J. R. Sambrano, M. Lucio Moreira, and M. J. Piotrowski, Sci. Rep. **14**, 16648 (2024).

[407] M. Jakhar, R. Sharma, and A. Kumar, Nanoscale **15**, 5964 (2023).

[408] Y. Li, J. Li, J. Tian, H. Liu, and J. Shi, ACS Appl. Nano Mater. **7**, 15086 (2024).
[409] K. Sujata, N. Verma, R. G. Solanki, and A. Kumar, Mater. Adv. **6**, 849 (2025).
[410] N. K. Sharma, V. Mahajan, R. Adhikari, and H. Sharma, Nanoscale **16**, 3091 (2024).
[411] X. Xuan, Z. Yang, R. Du, Y. Zhao, Y. Yan, C. Liu, H. Li, and G. Zhang, Mater. Adv. **4**, 4852 (2023).
[412] T. Zhang and L. Zhu, J. Mater. Chem. C **12**, 15578 (2024).
[413] X. Jiang, Z. Zhang, Z. Liu, J. Wang, and Y. Liu, Appl. Phys. Lett. **120**, 132202 (2022).
[414] W. Li, H. Wang, Z. Liu, and G. Yang, Eur. Phys. J. Plus **140**, 12 (2025).
[415] F. Duan, D. Wei, A. Chen, X. Zheng, H. Wang, and G. Qin, Nanoscale **15**, 1459 (2023).
[416] T. M. G. Mohiuddin, A. Lombardo, R. R. Nair, A. Bonetti, G. Savini, R. Jalil, N. Bonini, D. M. Basko, C. Galiotis, N. Marzari, K. S. Novoselov, A. K. Geim, and A. C. Ferrari, Phys. Rev. B **79**, 205433 (2009).
[417] G. Qin, Z. Qin, H. Wang, and M. Hu, Nano Energy **50**, 425 (2018).
[418] Y. Zeng, C.-L. Lo, S. Zhang, Z. Chen, and A. Marconnet, Carbon **158**, 63 (2020).
[419] K. Nakagawa, K. Satoh, S. Murakami, K. Takei, S. Akita, and T. Arie, Sci. Rep. **11**, 19533 (2021).
[420] Z. Fan, L. F. C. Pereira, P. Hirvonen, M. M. Ervasti, K. R. Elder, D. Donadio, T. Ala-Nissila, and A. Harju, Phys. Rev. B **95**, 144309 (2017).
[421] V. J. Ramirez Rivera, F. Mamani Gonzalo, H. E. Nina Mendoza, M. Jeomar Piotrowski, J. A. Chacaltana Garcia, E. Rodriguez Delgado, and E. Mamani Flores, J. Appl. Phys. **136**, 234301 (2024)\.
[422] J. Liu, M. Fang, E.-H. Yang, and X. Zhang, Sci. Rep. **15**, 1976 (2025).
[423] J.-W. Jiang, H. S. Park, and T. Rabczuk, J. Appl. Phys. **114**, 064307 (2013).
[424] H. Liu, G. Qin, Y. Lin, and M. Hu, Nano Lett. **16**, 3831 (2016).
[425] Y. Han, G. Qin, C. Jungemann, and M. Hu, Nanotechnology **27**, 265706 (2016).
[426] Y. Kuang, L. Lindsay, and B. Huang, Nano Lett. **15**, 6121 (2015).
[427] Z. Sun, K. Yuan, X. Zhang, G. Qin, X. Gong, and D. Tang, Phys. Chem. Chem. Phys. **21**, 15647 (2019).
[428] X. Meng, T. Pandey, J. Jeong, S. Fu, J. Yang, K. Chen, A. Singh, F. He, X. Xu, J. Zhou, W.-P. Hsieh, A. K. Singh, J.-F. Lin, and Y. Wang, Phys. Rev. Lett. **122**, 155901 (2019).
[429] A. Taheri, C. Da Silva, and C. H. Amon, Phys. Chem. Chem. Phys. **20**, 27611 (2018).
[430] M. Raeisi, S. Ahmadi, and A. Rajabpour, Nanoscale **11**, 21799 (2019).
[431] Z. Sun, K. Yuan, Z. Chang, X. Zhang, G. Qin, and D. Tang, J. Appl. Phys. **126**, 125104 (2019).
[432] F. Duan, C. Shen, H. Zhang, and G. Qin, Phys. Rev. B **105**, 125406 (2022).
[433] Y. Gao, Y. Jing, J. Liu, X. Li, and Q. Meng, Appl. Therm. Eng. **113**, 1419 (2017).
[434] J.-J. Ma, J.-J. Zheng, W.-D. Li, D.-H. Wang, and B.-T. Wang, Phys. Chem. Chem. Phys. **22**, 5832 (2020).
[435] M. Yarali, H. Brahmi, Z. Yan, X. Li, L. Xie, S. Chen, S. Kumar, M. Yoon, K. Xiao, and A. Mavrokefalos, ACS Appl. Mater. Interfaces **10**, 4921 (2018).
[436] Z. Ding, Q.-X. Pei, J.-W. Jiang, and Y.-W. Zhang, J. Phys. Chem. C **119**, 16358 (2015).
[437] H. Zhang, G. Lee, and K. Cho, Phys. Rev. B **84**, 115460 (2011).
[438] C. A. Polanco and L. Lindsay, Phys. Rev. B **97**, 014303 (2018).
[439] X. Wu and Q. Han, Comput. Mater. Sci. **184**, 109938 (2020).
[440] Y. Liu, C. Xiao, Z. Li, and Y. Xie, Adv. Energy Mater. **6**, 1600436 (2016).
[441] L. Cui, S. Shi, Z. Li, G. Wei, and X. Du, Phys. Chem. Chem. Phys. **20**, 27169 (2018).
[442] D. C. Desai, B. Zviazhynski, J.-J. Zhou, and M. Bernardi, Phys. Rev. B **103**, L161103 (2021).
[443] N. Zen, T. A. Puurtinen, T. J. Isotalo, S. Chaudhuri, and I. J. Maasilta, Nat. Commun. **5**, 3435 (2014).
[444] W. Yao, B. Wu, and Y. Liu, ACS Nano **14**, 9320 (2020).
[445] P. Man, D. Srolovitz, J. Zhao, and T. H. Ly, Acc. Chem. Res. **54**, 4191 (2021).
[446] G.-K. Ren, J.-L. Lan, K. J. Ventura, X. Tan, Y.-H. Lin, and C.-W. Nan, npj Comput. Mater. **2**, 16023 (2016).
[447] K. R. Hahn, C. Melis, and L. Colombo, Carbon **96**, 429 (2016).
[448] D. Lee, S. Lee, B.-S. An, T.-H. Kim, C.-W. Yang, J. W. Suk, and S. Baik, Chem. Mater. **29**, 10409 (2017).
[449] T. Ma, Z. Liu, J. Wen, Y. Gao, X. Ren, H. Chen, C. Jin, X.-L. Ma, N. Xu, H.-M. Cheng, and W. Ren, Nat. Commun. **8**, 14486 (2017).
[450] S. R. Yeandel, M. Molinari, and S. C. Parker, Nanoscale **10**, 15010 (2018).
[451] A. Wei, Q. Liu, H. Yao, Y. Li, and Y. Li, J. Phys. Chem. C **122**, 19869 (2018).
[452] M. Zhang, B. Zou, X. Zhang, Y. Zhou, and H. Sun, J. Alloys Compd. **856**, 158119 (2021).
[453] J. Sun, Y. Guo, Q. Wang, and Y. Kawazoe, Carbon **145**, 445 (2019).
[454] L. M. Sandonas, H. Sevincli, R. Gutierrez, and G. Cuniberti, Adv. Sci. **5**, 1700365 (2018).
[455] J. Chen, X. Xu, J. Zhou, and B. Li, Rev. Mod. Phys. **94**, 025002 (2022).
[456] Y. Gao, Q. Liu, and B. Xu, ACS Nano **10**, 5431 (2016).
[457] Y. Gao, W. Yang, and B. Xu, Adv. Mater. Interfaces **4**, 1700278 (2017).
[458] Y. Zhang, Q. Lv, H. Wang, S. Zhao, Q. Xiong, R. Lv, and X. Zhang, Science **378**, 169 (2022).
[459] X.-K. Chen, Z.-X. Xie, W.-X. Zhou, L.-M. Tang, and K.-Q. Chen, Carbon **100**, 492 (2016).
[460] X.-K. Chen, J.-W. Hu, X.-J. Wu, P. Jia, Z.-H. Peng, and K.-Q. Chen, J. Phys. D: Appl. Phys. **51**, 085103 (2018).
[461] M.-K. Hong, S.-H. Hyun, H.-S. Jang, B.-S. An, H.-C. Jang, H.-S. Hwang, S.-I. Kim, J.-Y. Moon, S. M. Sattari-Esfahlan, S.-Y. Lee, *et al.*, Appl. Surf. Sci. **554**, 149655 (2021).
[462] X. Liu and M. C. Hersam, Sci. Adv. **5**, eaax6444 (2019).
[463] Y. Guo, S. Zhou, Y. Bai, and J. Zhao, J. Supercond. Nov. Magn. **29**, 717 (2016).

[464] B. Mortazavi, A. Rajabpour, S. Ahzi, Y. Rémond, and S. Mehdi Vaez Allaei, Solid State Commun. **152**, 261 (2012).

[465] B. Yang, D. Li, L. Qi, T. Li, and P. Yang, Phys. Lett. A **383**, 1306 (2019).

[466] A. Giri and P. E. Hopkins, J. Appl. Phys. **125**, 205102 (2019).

[467] X. Ma, S. Wu, Z. Yi, D. Peng, and J. Zhang, Int. J. Heat Mass Transf. **137**, 790 (2019).

[468] Z. Yan, M. Yoon, and S. Kumar, 2D Mater. **5**, 031008 (2018).

[469] H. Wei, X. Xiao, X. Jin, X. Wan, L. Shi, Y. Duan, J. Fan, R. Wang, and X. Wu, ACS Appl. Nano Mater. **8**, 244 (2025).

[470] Z. Du, X. Chen, J. Zhu, and J. Cui, Curr. Appl. Phys. **18**, 893 (2018).

[471] J. Hu, S. Schiffli, A. Vallabhaneni, X. Ruan, and Y. P. Chen, Appl. Phys. Lett. **97**, 133107 (2010).

[472] J.-W. Jiang, J. Lan, J.-S. Wang, and B. Li, J. Appl. Phys. **107**, 054314 (2010).

[473] L. Lindsay and D. A. Broido, Phys. Rev. B **84**, 155421 (2011).

[474] S. Chen, Q. Wu, C. Mishra, J. Kang, H. Zhang, K. Cho, W. Cai, A. A. Balandin, and R. S. Ruoff, Nat. Mater. **11**, 203 (2012).

[475] E. Whiteway, M. Lee, and M. Hilke, ACS Appl. Nano Mater. **3**, 9167 (2020).

[476] G. Trambly de Laissardière, D. Mayou, and L. Magaud, Nano Lett. **10**, 804 (2010).

[477] Z.-D. Song and B. A. Bernevig, Phys. Rev. Lett. **129**, 047601 (2022).

[478] N. R. Chebrolu, B. L. Chittari, and J. Jung, Phys. Rev. B **99**, 235417 (2019).

[479] Y. Cao, V. Fatemi, A. Demir, S. Fang, S. L. Tomarken, J. Y. Luo, J. D. Sanchez-Yamagishi, K. Watanabe, T. Taniguchi, E. Kaxiras, R. C. Ashoori, and P. Jarillo-Herrero, Nature (London) **556**, 80 (2018).

[480] S. Lisi, X. Lu, T. Benschop, T. A. de Jong, P. Stepanov, J. R. Duran, F. Margot, I. Cucchi, E. Cappelli, A. Hunter, *et al.*, Nat. Phys. **17**, 189 (2021).

[481] M. I. B. Utama, R. J. Koch, K. Lee, N. Leconte, H. Li, S. Zhao, L. Jiang, J. Zhu, K. Watanabe, T. Taniguchi, *et al.*, Nat. Phys. **17**, 184 (2021).

[482] B. Ghawri, P. S. Mahapatra, M. Garg, S. Mandal, S. Bhowmik, A. Jayaraman, R. Soni, K. Watanabe, T. Taniguchi, H. R. Krishnamurthy, *et al.*, Nat. Commun. **13**, 1522 (2022).

[483] A. Jayaraman, K. Hsieh, B. Ghawri, P. S. Mahapatra, K. Watanabe, T. Taniguchi, and A. Ghosh, Nano Lett. **21**, 1221 (2021).

[484] S. S. Kubakaddi, J. Phys.: Condens. Matter **33**, 245704 (2021).

[485] D. Guerci, P. Simon, and C. Mora, Phys. Rev. Res. **4**, L012013 (2022).

[486] P. S. Mahapatra, B. Ghawri, M. Garg, S. Mandal, K. Watanabe, T. Taniguchi, M. Jain, S. Mukerjee, and A. Ghosh, Phys. Rev. Lett. **125**, 226802 (2020).

[487] P. S. Mahapatra, K. Sarkar, H. R. Krishnamurthy, S. Mukerjee, and A. Ghosh, Nano Lett. **17**, 6822 (2017).

[488] A. Kommini and Z. Aksamija, 2D Mater. **8**, 045022 (2021).

[489] N. Gupta, S. Rani, P. Kumari, R. Ahuja, and S. J. Ray, Carbon **215**, 118437 (2023).

[490] S. J. Yang, D. Kim, J. Choi, S. H. Kim, K. Park, S. Ryu, and K. Cho, Adv. Mater. **33**, 2102797 (2021).

[491] A. Giri, A. Z. Chen, A. Mattoni, K. Aryana, D. Zhang, X. Hu, S.-H. Lee, J. J. Choi, and P. E. Hopkins, Nano Lett. **20**, 3331 (2020).

[492] S.-N. Hsu, W. Zhao, Y. Gao, Akriti, M. Segovia, X. Xu, B. W. Boudouris, and L. Dou, Nano Lett. **21**, 7839 (2021).

[493] Y. He, C. D. Spataru, F. Léonard, R. E. Jones, M. E. Foster, M. D. Allendorf, and A. Alec Talin, Phys. Chem. Chem. Phys. **19**, 19461 (2017).

[494] P. Ninawe, K. Gupta, and N. Ballav, Inorg. Chem. **60**, 19079 (2021).

[495] L. Sun, B. Liao, D. Sheberla, D. Kraemer, J. Zhou, E. A. Stach, D. Zakharov, V. Stavila, A. A. Talin, Y. Ge, *et al.*, Joule **1**, 168 (2017).

[496] M. de Lourdes Gonzalez-Juarez, E. Flores, M. Martin-Gonzalez, I. Nandhakumar, and D. Bradshaw, J. Mater. Chem. A **8**, 13197 (2020).

[497] R. Tsuchikawa, N. Lotfizadeh, N. Lahiri, S. Liu, M. Lach, C. Slam, J. Louie, and V. V. Deshpande, Phys. Status Solidi A **217**, 2000437 (2020).

[498] Z. Chen, Y. Cui, L. Liang, H. Wang, W. Xu, Q. Zhang, and G. Chen, Mater. Today Nano **20**, 100276 (2022).

[499] K. J. Erickson, F. Léonard, V. Stavila, M. E. Foster, C. D. Spataru, R. E. Jones, B. M. Foley, P. E. Hopkins, M. D. Allendorf, and A. A. Talin, Adv. Mater. **27**, 3453 (2015).

[500] Z. Chen, Y. Cui, Y. Jin, L. Liu, J. Yan, Y. Sun, Y. Zou, Y. Sun, W. Xu, and D. Zhu, J. Mater. Chem. C **8**, 8199 (2020).

[501] M. Islamov, H. Babaei, R. Anderson, K. B. Sezginel, J. R. Long, A. J. H. McGaughey, D. A. Gomez-Gualdron, and C. E. Wilmer, npj Comput. Mater. **9**, 11 (2023).

[502] L. Wang, B. Dong, R. Ge, F. Jiang, and J. Xu, ACS Appl. Mater. Interfaces **9**, 7108 (2017).

[503] T. Zhou, X. Wu, T. Deng, H. Li, Z. Gao, and W. Shi, J. Mater. Chem. A **11**, 15821 (2023).

[504] Y. Pang, Z. Yang, Y. Yang, and T.-L. Ren, Small **16**, 1901124 (2020).

[505] M. H. Lee and W. Wu, Adv. Mater. Technol. **7**, 2101623 (2022).

[506] D. Jiang, Z. Liu, Z. Xiao, Z. Qian, Y. Sun, Z. Zeng, and R. Wang, J. Mater. Chem. A **10**, 89 (2021).

[507] B. Cho, A. R. Kim, D. J. Kim, H.-S. Chung, S. Y. Choi, J.-D. Kwon, S. W. Park, Y. Kim, B. H. Lee, K. H. Lee, *et al.*, ACS Appl. Mater. Interfaces **8**, 19635 (2016).

[508] Y. Guo, C. Dun, J. Xu, P. Li, W. Huang, J. Mu, C. Hou, C. A. Hewitt, Q. Zhang, Y. Li, D. L. Carroll, and H. Wang, ACS Appl. Mater. Interfaces **10**, 33316 (2018).

[509] Z.-H. Zheng, X.-L. Shi, D.-W. Ao, W.-D. Liu, M. Li, L.-Z. Kou, Y.-X. Chen, F. Li, M. Wei, G.-X. Liang, *et al.*, Nat. Sustainability **6**, 180 (2023).

[510] D. Kong, W. Zhu, Z. Guo, and Y. Deng, Energy **175**, 292 (2019).

[511] T. G. Novak, J. Kim, J. Kim, H. Shin, A. P. Tiwari, J. Y. Song, and S. Jeon, 2D Mater. **6**, 045019 (2019).

[512] T. G. Novak, J. Kim, J. Kim, A. P. Tiwari, H. Shin, J. Y. Song, and S. Jeon, Adv. Funct. Mater. **30**, 2001760 (2020).

[513] Z. Wang, M. Chen, Z. Cao, J. Liang, Z. Liu, Y. Xuan, L. Pan, K. M. Razeeb, Y. Wang, C. Wan, and P.-a. Zong, ACS Appl. Nano Mater. **5**, 16872 (2022).
[514] E. Liu, A. Negm, and M. Howlader, Mater. Today Energy **20**, 100625 (2021).
[515] J. Zhou, B. Liao, and G. Chen, Semicond. Sci. Technol. **31**, 043001 (2016).
[516] B. Kozinsky and D. J. Singh, Annu. Rev. Mater. Res. **51**, 565 (2021).
[517] B. Ryu and M.-W. Oh, J. Korean Ceram. Soc. **53**, 273 (2016).
[518] A. S. Chaves, M. Pizzochero, D. T. Larson, A. Antonelli, and E. Kaxiras, J. Comput. Electron. **22**, 1281 (2023).
[519] P. Gorai, V. Stevanović, and E. S. Toberer, Nat. Rev. Mater. **2**, 17053 (2017).
[520] J. Yang, L. Xi, W. Qiu, L. Wu, X. Shi, L. Chen, J. Yang, W. Zhang, C. Uher, and D. J. Singh, npj Comput. Mater. **2**, 15015 (2016).